Morphology and dynamics of storm-time ionospheric density structures

Evan Grier Thomas

Dissertation submitted to the faculty of the
Virginia Polytechnic Institute and State University
in partial fulfillment of the requirements for the degree of

Doctor of Philosophy
in
Electrical Engineering

J. Michael Ruohoniemi, Co-Chair
Joseph B. H. Baker, Co-Chair
Scott M. Bailey
Robert W. McGwier
Wayne A. Scales
Kevin A. Shinpaugh

02/16/2016
Blacksburg, VA

Keywords: SuperDARN, GPS TEC, Polar Cap Patch, Ionospheric Storm

Morphology and dynamics of storm-time ionospheric density structures

Evan Grier Thomas

ABSTRACT

Accurate knowledge of the electron density structure of the Earth's upper atmosphere is crucial to forecasting the performance of transionospheric radio signals. For this research, we focus on storm-time structuring in the mid- to high latitude ionosphere where large gradients in electron density can cause severe degradation of communication and navigation signals. We begin in Chapter 2 with a review of the primary data sets and methods used to accomplish the collaborative, multi-instrument studies described in this dissertation. In Chapter 3, we compare observational techniques for tracking polar cap patches during a moderate geomagnetic storm interval. For the first time, we monitor the transportation of patches with high spatial and temporal resolution across the polar cap for 1–2 h using a combination of GPS TEC, all-sky airglow imagers (ASIs), and Super Dual Auroral Radar Network (SuperDARN) HF radar backscatter. Simultaneous measurements from these data sets allow for continuous tracking of patch location, horizontal extent, and velocity even under adverse observational conditions for one or more of the techniques. A focus is placed on the structuring of patches, particularly on the nightside ionosphere as they become wider in the dawn-dusk direction and develop narrow finger-like structures. In Chapter 4, we perform a superposed epoch analysis to characterize the average response of GPS TEC in the North American sector during more than 100 geomagnetic storms over a 13-year interval. For the first time a rigorous approach is used to fully separate storm-time, local time, longitudinal, and seasonal effects at midlatitudes where dense ground receiver coverage is available. The rapid onset of a positive phase is observed across much of the dayside and evening ionosphere followed by a longer-lasting negative phase across all latitudes and local times. Our results show clear seasonal variations in the storm-time TEC, such that summer events tend to be dominated by the negative storm response while winter events exhibit a stronger initial positive phase with minimal negative storm effects. A prominent magnetic declination effect is identified and examined in terms of thermospheric zonal winds pushing plasma upward/downward along magnetic field lines of opposite declination. Finally in Chapter 5 we summarize several co-authored studies which examined various storm-time phenomena utilizing GPS TEC mapping tools developed for this dissertation research, with topics including subauroral polarization stream (SAPS), storm enhanced density (SED), tongue of ionization (TOI), and polar cap patches.

Acknowledgments

I would like to start by thanking my advisors, Dr. Jo Baker and Dr. Mike Ruohoniemi, for all of their guidance and support over the last six-plus years as a member of their research group. I could never have imagined that a short conversation with Dr. Baker after a lecture during my senior year would evolve into a Masters and Doctoral graduate research program that would bring me all over the world. Thank you to Dr. Lasse Clausen for teaching me IDL and gamely answering so many other questions - none of these wonderful GPS TEC figures would have been otherwise possible. I would also like to make a very special thanks to all of my past and present labmates for their support and encouragement. Specifically, I would like to thank Kevin and Nathaniel for all of their tireless work keeping the radars and data servers functioning. A special mention also goes to my former VT SD colleagues (AJ, Bharat, Sebastien) who have made the transition from space physics to greener pastures in Silicon Valley and beyond.

I would like to thank Dr. Keisuke Hosokawa and Dr. Nozomu Nishitani for hosting me at their institutions during my 10-week visit to Japan with support from an NSF EAPSI and JSPS Summer Program fellowship. My stay in Japan was an absolutely amazing experience and I am truly grateful for being afforded such a research opportunity during my graduate studies. I would also like to thank Dr. David Sibeck at NASA Goddard Space Flight Center for providing office and desk space during my two years as a visiting scientist there. Special thanks also go to Brian Walsh and Kyle Murphy at NASA/GSFC for their support and guidance during my time at Goddard. I am very grateful to all of my co-authors and scientific collaborators over the last few years, who are too numerous to list here. However

I would like to specifically acknowledge Dr. Anthea Coster who introduced me to the GPS TEC data set which would eventually play a central role in my graduate studies and this dissertation.

Finally, I would like to thank my family for their love and support in helping me become the person I am today. And a very, very special thanks to Rachel for putting up with all of the time, distance, and effort that went into this dissertation.

Evan Thomas
Blacksburg, VA
February 2016

Funding for this research was provided by the National Science Foundation under grants AGS-1243070, AGS-1341918, and IIA-1310774. Support was also provided by the Virginia Space Grant Consortium under a graduate research fellowship.

Attribution

Several colleagues provided data, research, figures, and text which culminated in the two manuscripts presented as Chapters 3 and 4 in this dissertation. A brief description of their contributions is included here.

Joseph B. H. Baker, PhD (Virginia Tech) is an Associate Professor in the Bradley Department of Electrical and Computer Engineering at Virginia Tech. He was a co-author for Chapters 3 and 4 and is a Co-Investigator for the NSF grants supporting this research. Dr. Baker is one of two advisors for my graduate studies and has contributed text and editorial comments throughout this dissertation.

J. Michael Ruohoniemi, PhD (Virginia Tech) is an Associate Professor in the Bradley Department of Electrical and Computer Engineering at Virginia Tech. He was a co-author for Chapters 3 and 4 and is the Principal Investigator for the NSF grants supporting this research. Dr. Ruohoniemi is one of two advisors for my graduate studies and has contributed text and editorial comments throughout this disssertation.

Keisuke Hosokawa, PhD (University of Electro-Communications) is an Assistant Professor in the Department of Communication Engineering and Informatics at the University of Electro-Communications. He was a co-author for Chapter 3 and assists with the operation and maintenance of the all-sky airglow imagers at Resolute Bay and Svalbard. Dr. Hosokawa was the primary host scientist for a 10 week research visit to Japan through the NSF East Asia and Pacific Summer Institutes (EAPSI) program and provided guidance and software expertise. He has also contributed text and editorial comments for Chapter 3.

Jun Sakai, PhD (University of Electro-Communications) is a Researcher in the Center for Space Science and Radio Engineering at the University of Electro-Communications. He was a co-author for Chapter 3 and provided guidance during the 10 week research visit to Japan. Dr. Sakai has also contributed text and editorial comments for Chapter 3.

Satoshi Taguchi, PhD (Kyoto University) is a Professor in the Department of Geophysics at Kyoto University. He was a co-author for Chapter 3 and is the Principal Investigator of the all-sky airglow imager at Svalbard.

Kazuo Shiokawa, PhD (Nagoya University) is a Professor in the Institute for Space-Earth Environment Reserach at Nagoya University. He was a co-author for Chapter 3 and is the Principal Investigator of the all-sky airgow imager at Resolute Bay. Dr. Shiokawa also contributed editorial comments.

Yuichi Otsuka, PhD (Nagoya University) is an Associate Professor in the Institute for Space-Earth Environment Research at Nagoya University. He was a co-author for Chapter 3 and assists with the operation and maintenance of the all-sky airglow imager at Resolute Bay.

Anthea J. Coster, PhD (MIT Haystack Observatory) is a Principal Research Scientist in the Atmospheric Sciences Group at MIT Haystack Observatory. She was a co-author for Chapters 3 and 4 and is the Principal Investigator of the GPS total electron content data set in the Madrigal database. Dr. Coster has also hosted several research visits to MIT Haystack Observatory and contributed editorial comments.

Jean-Pierre St.-Maurice, PhD (University of Saskatchewan) is a Professor in the Department of Physics and Engineering Physics at the University of Saskatchewan. He was a co-author for Chapter 3 and is a Principal Investigator of SuperDARN Canada. Dr. St.-Maurice also contributed editorial comments.

Kathryn A. McWilliams, PhD (University of Saskatchewan) is an Associate Professor in the Department of Physics and Engineering Physics at the University of Saskatchewan. She was a co-author for Chapter 3 and is a Principal Investigator of SuperDARN Canada. Dr. McWilliams also contributed editorial comments.

Shun-Rong Zhang, PhD (MIT Haystack Observatory) is a Research Scientist in the Atmospheric Sciences Group at MIT Haystack Observatory. He was a co-author for Chapter 4 and provided guidance on the effects of magnetic field line declination. Dr. Zhang also contributed editorial comments.

Contents

List of Figures

List of Tables

Chapter 1

Introduction

1.1 The Ionosphere

The ionosphere is a region of weakly ionized plasma which stretches from about 50–1,000 km altitude above the Earth's surface. Although neutral components still dominate at these altitudes, the ionization is sufficient to endow the atmosphere with electrical properties. The ionosphere is divided into three principal layers: the D region (below 90 km), E region (between 90 km and 130 km), and F region (above 130 km). Oftentimes the F region is further divided into F_1 and F_2 layers because of the smaller peak sometimes seen in the density profile below the main (F_2) peak. Absorption of solar radiation by neutral molecules is the primary source of atmospheric ionization except at auroral latitudes where energetic particle precipitation can be significant. Field-aligned currents connecting the magnetosphere to the ionosphere are the primary mechanism by which these energetic particles are transported to the ionosphere. Figure 1.1 shows the density and composition of the daytime ionosphere (solid lines) and neutral atmosphere (dashed lines) in terms of number density versus altitude. The primary ionospheric layers are defined by density peaks that result from an interplay of local production, loss, and transport processes [*Luhmann*, 1995].

Electron density balance in the ionosphere is described by the continuity equation

$$\frac{\partial N}{\partial t} = q - l(N) - \nabla \cdot (N\mathbf{V}) \tag{1.1}$$

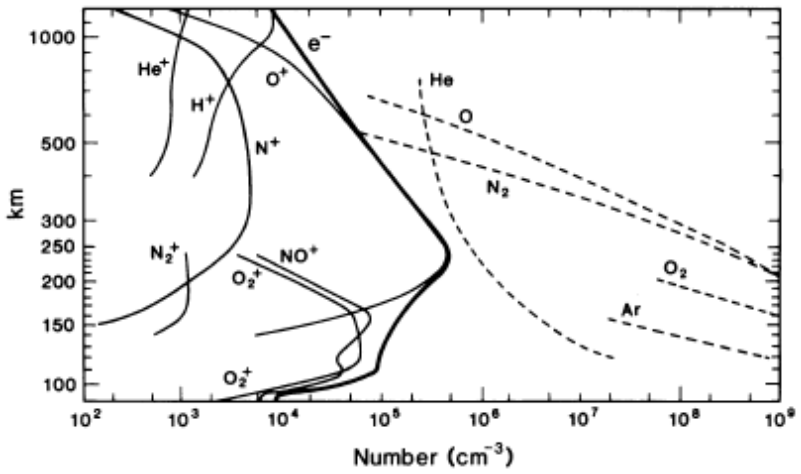

Figure 1.1: Density and composition of the daytime ionosphere and neutral atmosphere in terms of number density versus altitude based on mass-spectrometer measurements [*Luhmann*, 1995].

where N is the electron density, q the production rate of ionization, $l(N)$ the loss term, and $\mathbf{V}$ is a net drift velocity resulting from transport processes. At F_2-region heights the dominant dayside production mechanism is the photoionization of atomic oxygen via solar extreme ultraviolet (EUV) radiation

$$\mathrm{O} + h\nu \rightarrow \mathrm{O}^+ + e^-$$

where $h\nu$ is a photon, h is Planck's constant (6.62×10^{-34} $\mathrm{m^2kg/s}$), and ν is the frequency of the photon (Hz). Direct recombination of these oxygen ions with electrons via radiative recombination is a very slow and inefficient process. Instead, the dominant loss mechanism is a two-step process where atomic oxygen ions first undergo charge transfer with the molecular neutral constituents $\mathrm{O_2}$ or $\mathrm{N_2}$

$$\mathrm{O}^+ + \mathrm{O_2} \rightarrow \mathrm{O_2^+} + \mathrm{O}$$
$$\mathrm{O}^+ + \mathrm{N_2} \rightarrow \mathrm{NO}^+ + \mathrm{N}$$

These newly produced O_2^+ and NO^+ ions are then quickly lost to dissociative recombination of the form

$$O_2^+ + e^- \rightarrow O + O^*$$
$$NO^+ + e^- \rightarrow O + N^*$$

Production and loss of ionization in the F-region is therefore largely dependent on the neutral atmosphere composition in terms of O, O_2, and N_2. Note, that below about 100 km the neutral constituents are turbulently mixed, while at higher altitudes the vertical distribution of neutrals is determined by molecular weight via diffusive transport [*Rishbeth and Garriott*, 1969].

The above production and loss processes are balanced by the transport term in Equation (1.1), which in practice is often a superposition of several different mechanisms. At F-region altitudes both ions and electrons drift with a nearly horizontal velocity given by $\mathbf{v} = \mathbf{E}\times\mathbf{B}/B^2$, where $\mathbf{E}$ is the ionospheric electric field and $\mathbf{B}$ is the geomagnetic field. The large-scale motion of the plasma most often conforms to a two-cell pattern, with antisunward flow from the dayside across the polar cap to the nightside and return flow at auroral latitudes in the dawn and dusk sectors [*Heppner and Maynard*, 1987; *Ruohoniemi and Greenwald*, 1996]. Charged particles may also be transported by thermospheric neutral winds. These neutral winds vary with the daily heating and cooling of the upper atmosphere and are governed by the viscosity of air, Coriolis force, and ion-drag due to collisions [*Rishbeth*, 1998]. Ions and electrons may also undergo plasma diffusion due to gravity or pressure gradients, which in the F-region may only occur along magnetic field lines. In the presence of an inclined magnetic field these transport mechanisms will impart both a horizontal and vertical motion to the ionospheric plasma. In the following sections, we will discuss how transient events driven by the sun can produce large perturbations in the ionospheric

electron density morphology.

1.2 Geomagnetic Disturbances

Large variations in the Earth's magnetic field, known as geomagnetic storms, have been studied using ground-based magnetometers since the mid-1800's [e.g., *Chapman and Bartels*, 1940]. These disturbances correspond to periods of intense coupling between the solar wind and magnetosphere and are often associated with extreme features in the solar wind such as coronal mass ejctions (CMEs) or co-rotating interaction regions (CIRs). Geomagnetic storms are typically divided into three phases according to the deviation in the horizontal magnetic field component H (Figure 1.2). First, a sudden positive increase in the H component may be observed which can often be attributed to a compression of the magnetopause due to an interplanetary shock structure in the solar wind. It should be noted however that this initial phase is not a requisite feature of all magnetic storms [*Gonzalez et al.*, 1992]. The storm main phase begins once the interplanetary magnetic field (IMF) turns southward, driving magnetic reconnection at the dayside magnetopause and depositing a large amount of energy into the magnetosphere [*Kozyra et al.*, 1998]. This coupling leads to an intensification of the ring current and the sharp decrease in the H component seen from ∼20:00-23:30 UT in Figure 1.2. When the solar wind driving conditions reduce and the H component reaches its minimum value, the storm enters what is known as the recovery phase as the ring current intensity slowly decays. The recovery phase can last anywhere from a few hours to a few days as the magnetosphere returns to its pre-storm condition [*Gonzalez et al.*, 1994; *Kamide et al.*, 1998; *Hutchinson et al.*, 2011].

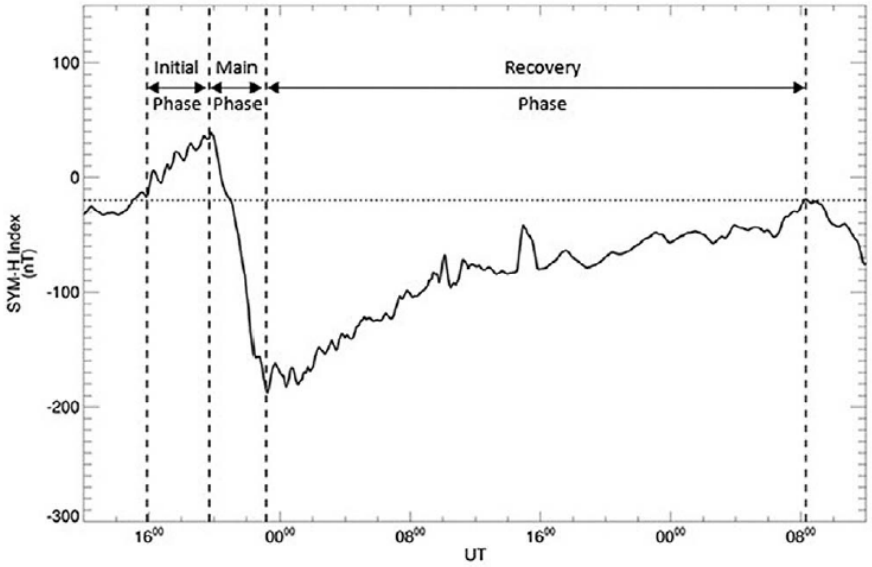

Figure 1.2: A characteristic Sym-H index trace showing initial, main, and recovery storm phases [*Hutchinson et al.*, 2011].

1.3 Ionospheric Storm Effects

The ionospheric response to geomagnetic storms has been studied since the first discovery of a conducting region of the Earth's upper atmosphere in the early 1900's [see Table 1 in *Prölss*, 2008]. While all ionospheric parameters are affected during a geomagnetic storm, an overwhelming majority of studies have focusd on perturbations in the electron concentration. This is because the electron density (specifically the maximum F_2-layer density, or N_mF_2) is the most easily measured parameter of the ionosphere. The storm-time variation in electron density has traditionally been classified as either a positive (increase) or negative (decrease) storm effect or phase [*Matsushita*, 1959]. In general, the initial storm response tends to be positive across much of the dayside ionosphere and commences soon after main phase onset [*Thomas and Venables*, 1966]. This initial positive phase is often followed by a prolonged negative phase, although some storms have been found to exhibit only a positive or negative response [*Prölss*, 1995]. Figure 1.3 shows one such example of the

ionospheric electron density response observed at two midlatitude ionosonde stations during a geomagnetic storm on 21-22 February 1973 [*Prölss*, 1980]. Following the onset of magnetic activity near 06:00 UT seen in the ap index (top panel), large departures from the monthly median measurements of N_{max} are observed at each station. Both negative (middle panel) and positive (bottom panel) storm effects appear to occur simultaneously in the southern and northern hemispheres, respectively. For several decades scientists were unable to fully explain the complex relationship between positive and negative ionospheric storm effects. As we will see in the next section, a comprehensive explanation requires a consideration of the thermospheric response to geomagnetic activity as well [*Buonsanto*, 1999].

1.4 Thermospheric Storm Effects

Solar wind energy is continuously dissipated in the polar regions of the Earth's upper atmosphere via particle precipitation and electrodynamic (Joule) heating, sufficient to create a permanent disturbance zone even under quiet geomagnetic conditions. This region is characterized by an increase in the gas temperature, an increase in the heavier gases (e.g., O_2 and N_2), and a decrease in the lighter gases (e.g., He) [*Prölss et al.*, 1988]. Thermospheric winds at F-region altitudes are driven by horizontal pressure gradients produced by the high-latitude energy input and dayside solar EUV heating. Under geomagnetically quiet conditions, these winds tend to diverge away from the vicinity of the subsolar point in the summer hemisphere and converge on the nightside in the winter hemisphere. As discussed in the previous section, the neutral wind velocity is further modulated by the viscosity of the air molecules, Coriolis force, and ion-drag [*Rishbeth*, 1998]. Thus during quiet conditions, the disturbance composition changes produced by heating are restricted to polar latitudes, except for the early morning sector where equatorward neutral winds may transport composition perturbations to subauroral latitudes. These composition changes are short-lived and rapidly

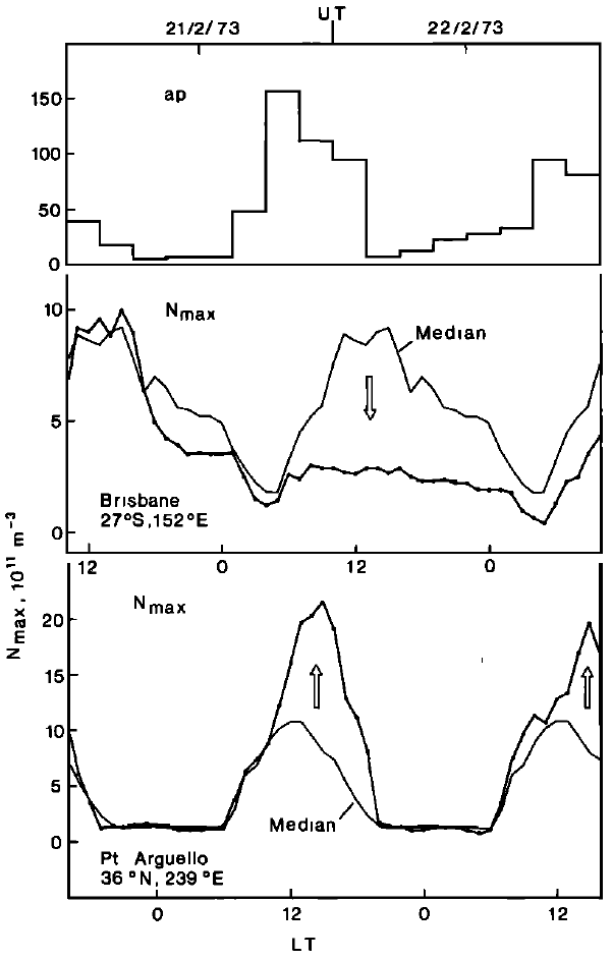

Figure 1.3: Example of magnetic storm induced changes in the ionospheric electron density. Measured F_2 layer maximum electron densities ($N_{\max}$, heavy dotted curves) obtained at two mid-latitude stations during the magnetic disturbance event of February 21 and 22 of 1973 (upper panel) illustrate negative and positive ionospheric storm effects (middle and lower panels). The monthly median serves as a quiet time reference (thin curves) [*Prölss*, 1980].

dissipate as they rotate to later local times (e.g., prestorm conditions shown in Figure 1.5a) [*Prölss*, 1995].

During storms, the neutral composition disturbance zone expands beyond the polar cap toward lower latitudes with increasing geomagnetic activity (Figure 1.4). Continued energy injection at high latitudes alters the global thermospheric wind circulation, reducing or even reversing the daytime poleward-directed winds. Strong winds or "storm surges" [*Volland*,

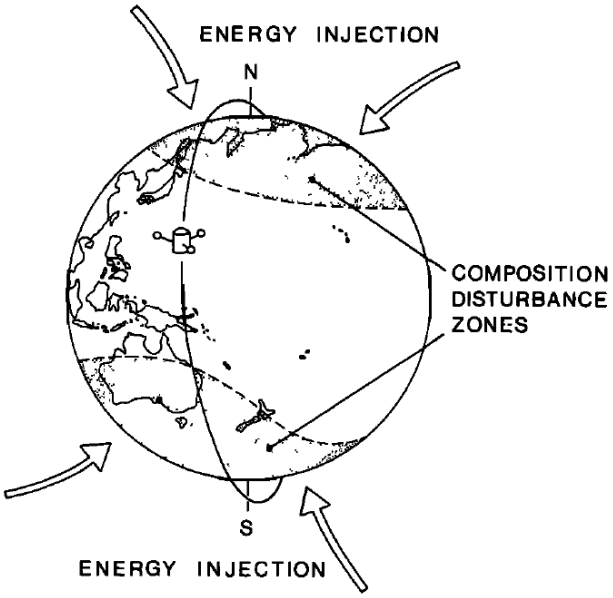

Figure 1.4: Energy injection and the formation of neutral composition disturbance zones during a magnetic storm. In addition, a sample orbit of the Esro 4 satellite is shown which provided neutral composition measurements [*Prölss*, 1980].

1979] in the post-midnight sector carry the molecularly rich air from the disturbance zone to middle latitudes (Figure 1.5b) where a negative storm effect will occur due to enhanced recombination at F region altitudes. This composition disturbance feature will then co-rotate to later local times as the storm progresses (Figure 1.5c). Therefore negative storm effects are largely attributed to chemical processes driven by the high-latitude energy input and modulated by the thermospheric neutral winds [*Prölss*, 1987; *Fuller-Rowell et al.*, 1994]. On the dayside, positive storm effects are due to an uplift of the ionospheric F-layer plasma to higher altitudes where molecular recombination is decreased while solar EUV photoionization persists. This vertical transport is believed to occur via a combinaton of equatorward-directed storm-time neutral winds and electrodynamical effects, although there is still significant uncertainty regarding which is the dominant mechanism [*Foster*, 1993; *Buonsanto*, 1995; *Prölss*, 1995].

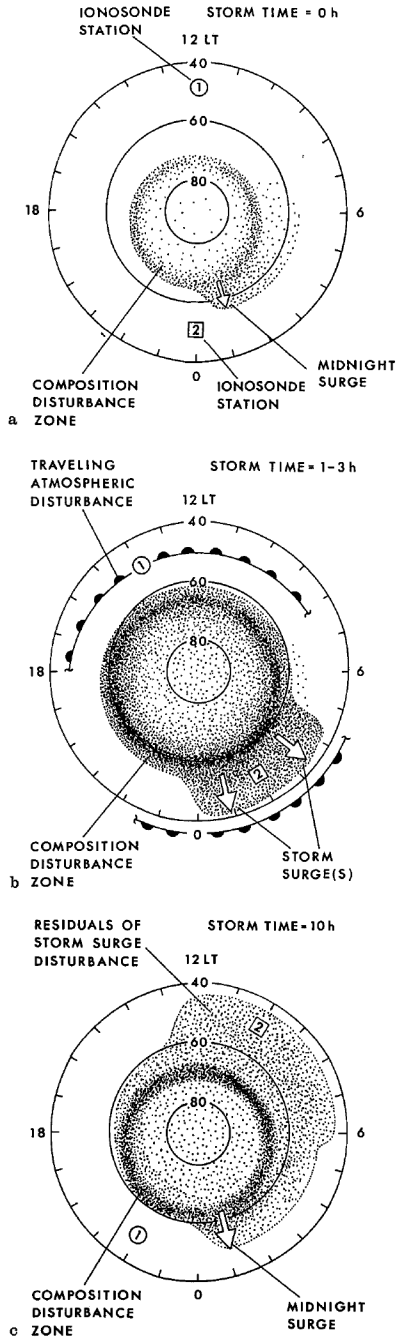

Figure 1.5: Schematic illustration of the time sequence of thermospheric-ionospheric storm effects. The dotted area identifies regions with an anomalously high N_2/O density ratio. (a) Illustrates prestorm conditions, (b) the expansion phase, and (c) the later phase of a storm. To show the expansion of the composition disturbance toward middle latitudes, the situation in the night sector of part b refers to a somewhat later time than that in the associated day sector [*Prölss*, 1993].

1.5 Mid- to High Latitude Ionospheric Storm Phenomena

Here we introduce several features of the mid- to high latitude storm-time ionosphere which are currently of significant interest to the space science community.

1.5.1 Subauroral Polarization Stream (SAPS)

The subauroral polarization stream (SAPS) is a relatively narrow channel ($\sim$5° magnetic latitude) of enhanced westward plasma flow ($\sim$0.5-1 km/s) located just equatorward of the lower electron precipitation boundary in the evening/nightside ionosphere. Sometimes embedded within SAPS is a narrower channel ($\sim$1° magnetic latitude) of even higher velocity flow ($\sim$1-2 km/s) known as a polarization jet (PJ) or subauroral ion drift (SAID). SAPS are believed to be caused by pressure gradients in the ring current during periods of sustained solar wind-magnetosphere coupling, leading to a separation between the ion and electron precipitation boundaries in the magnetospheric equatorial plane. A separation is also created between the ionospheric footpoint of field-aligned currents (FACs) driven by the precipitating ions and electrons. If a portion of these Region-2 FACs flow into regions of low conductivity in the subauroral ionosphere, such as the ionospheric density trough [*Rodger*, 2008], large north-south polarization electric fields are required to maintain current continuity which will drive a westward plasma drift. Frictional heating associated with these high-velocity drifts will enhance the ionospheric recombinaton rate and further decrease the plasma density [*Rodger et al.*, 1992], thus creating a positive feedback loop of increasingly-large electric fields [*Foster and Burke*, 2002]. Statistical characterizations of SAPS width, location, and intensity have largely been based on localized observations [*Foster and Vo*, 2002; *Erickson et al.*, 2011]. Additional research is necessary to test whether these parameterizations are

accurate across a range of magnetic local time (MLT) sectors.

1.5.2 Storm Enhanced Density (SED) and Polar Tongue of Ionization (TOI)

During the positive phase of ionospheric storms, when dayside electron densities are enhanced due to an uplift of the F_2-layer to regions of decreased recombination, plumes of ionization in the dusk sector can be carried sunward and poleward by the low-latitude edge of the SAPS [*Foster et al.*, 2007]. This storm enhanced density (SED) plume is characterized by increased densities, an elevated F peak altitude, and low electron and ion temperatures [*Foster*, 1993]. During sustained southward IMF conditions, the SED is transported through the cusp and into the polar cap by enhanced convection electric fields as either a continuous tongue of ionization (TOI) [*Sato and Rourke*, 1964; *Knudsen*, 1974] or polar cap patches [*Weber et al.*, 1986; *Crowley*, 1996]. There is currently some disagreement as to the distinction between a TOI and patches, although it should be noted that polar cap patches can be observed under any geomagnetic conditions and do not require the presence of an SED plume [*Hosokawa et al.*, 2014]. Here we focus on the SED plume and TOI; polar cap patches will be discussed separately in the next section (Section 1.5.3).

The connection between midlatitude SED structure and polar TOI was first demonstrated in a multi-instrument study during a large geomagnetic storm by *Foster et al.* [2005]. A plume of enhanced GPS total electron content (TEC) was seen to closely follow high-latitude convection streamlines derived from SuperDARN and satellite observations, although the lower-latitude sunward convecting regions were missed in the SuperDARN coverage. *Thomas et al.* [2013] analyzed a similarly linked SED/TOI interval when sufficient midlatitude observations were available to directly confirm the controlling role played by an expanding convection electric field in forming polar TOI from an SED plume. After the solar

wind drivers subsided (i.e., turned less southward IMF) the high-latitude convection pattern driving plasma motion was shown to retreat poleward, leaving behind a "fossil" SED plume which slowly decayed as it co-rotated to later local times. While the studies by *Foster et al.* [2005] and *Thomas et al.* [2013] demonstrated how SED plasma at midlatitudes could be drawn into the polar cap, questions still remain as to which mechanisms are responsible for the initial increase in the source plasma density. The degree to which SAPS transport [*Foster et al.*, 2007], an eastward penetration electric field [*Huang et al.*, 2011], or thermospheric processes [*Prölss*, 1995] control the generation and decay of these plumes remains an open question.

1.5.3 Polar Cap Patches

In contrast to the continuous tongue of ionization (TOI), polar cap patches are discrete structures in the F region ionosphere with electron densities at least twice that of the surrounding plasma [*Crowley*, 1996]. Patches are often formed in the dayside ionosphere near the footprint of the magnetospheric cusp during transient magnetic reconnection [*Lockwood and Carlson*, 1992] and propagate across the central polar cap toward the nightside where they may exit across a wide range of magnetic local times [*Moen et al.*, 2007]. The motion of polar cap patches is believed to be controlled by the background plasma convection [*Milan et al.*, 2002] as the incompressible nature of the ionospheric plasma has been demonstrated using incoherent scatter and SuperDARN radar observations [e.g., *Moen et al.*, 2001; *Davies et al.*, 2002]. However there are still many open questions regarding patch structuring and dynamics. For example, there appears to be some discrepancy in the dawn-dusk extent of patches observed during quiet geomagnetic conditions (wide, cigar-shaped) versus geomagnetically active periods (narrow, blob-shaped) [*Hosokawa et al.*, 2014]. There is also some debate whether the fine-scale structuring observed as patches approach the nightside

ionosphere is driven by the gradient drift instability [*Gondarenko et al.*, 2003; *Gondarenko and Guzdar*, 2004] or the shear driven instability [*Carlson*, 2012]. To resolve these issues, additional multi-instrument studies of polar cap patches characterizing each of the relevent ionospheric parameters (e.g., plasma density, temperature, velocity) are necessary.

1.5.4 Ionospheric Scintillation

Polar cap patches and tongue of ionization are particularly significant for commercial and military applications due to their impact on transionospheric radio signals. The sharp electron density gradients associated with these structures are believed to cause rapid fluctuations in signal amplitude and phase, called scintillation [*Aarons*, 1982; *Buchau et al.*, 1985], which can severely degrade GPS navigation signals. The S_4 and σ_Φ indices are two widely used measures for quantifying the degree of scintillation on GPS signals. The scintillation amplitude index S_4 is the standard deviation of the received power normalized by its mean value, while the phase index σ_Φ is the standard deviation of the detrended L1 phase using a filter in the receiver with a cutoff frequency. These indices are typically recorded using high-precision GPS receivers with sampling rates of at least 50 Hz [*Prikryl et al.*, 2013]. Because there are a limited number of GPS receivers with such a high sampling rate located within the polar cap, alternative techniques using lower-rate measurements are necessary for more comprehensive detection of scintillation occurrence. Only then will our understanding of the specific processes which cause ionospheric scintillation allow for proper forecasting of communication outages in the polar cap.

1.6 Research Objectives

Section 1.1 has introduced the structure of the ionosphere as well as the production, loss, and transport processes which govern the electron density distribution. During geomagnetic

storms, the intense coupling between the solar wind and magnetosphere causes large amounts of energy to be deposited into the Earth's magnetosphere-ionosphere-thermosphere (M-I-T) system. The resulting perturbations in ionospheric electron density can have a severe impact on over-the-horizon signal propagation and satellite navigation systems. Over the last two decades, maps of GPS total electron content (TEC) have improved our understanding of these ionospheric storm effects. The broad objective of this dissertation is to use this powerful data set to improve our understanding of storm-time electron density changes in the mid- to high latitude ionosphere. For example, we will obtain the first large-scale, statistical characterization of storm-time effects in TEC. Progress is demonstrated through a series of first-authored and co-authored publications that examine storm effects generally and the specific phenomena outlined in Section 1.5.

1.7 Dissertation Organization

Chapter 1 has begun our discussion with a review of ionospheric formation, structure, and storm-time perturbations as well as some outstanding research questions. Chapter 2 will introduce the primary data sets and methods used in this dissertation. Next, Chapter 3 will present a case study on the structuring and transport of polar cap patches during a moderate geomagnetic storm. Chapter 4 will consider the statistical ionospheric storm response at midlatitudes over North America in terms of storm-time, local time, seasonal, and longitudinal effects. Chapter 5 will proceed with a discussion of recent co-authored findings on various ionospheric storm phenomena. Finally, Chapter 6 will present conclusions and ideas for future research relevant to the current work.

Chapter 2

Data Sets and Methods

2.1 SuperDARN

To understand the role of convection electric field in plasma structuring and transport we use observations from a global network of ground-based high frequency (HF) radars. The first Super Dual Auroral Radar Network (SuperDARN) radar was constructed in Goose Bay, Labrador and saw first light in October 1983 [*Greenwald et al.*, 1985]. The Goose Bay radar is still in operation and continuously measures LOS velocities, spectral width, and backscattered power from decameter-scale field-aligned plasma irregularities in the F region ionosphere. The main antenna array consists of 16 log-periodic antennas which transmit and receive signals over a frequency range from 8-20 MHz [*Greenwald et al.*, 1995]. In its present state, the SuperDARN network consists of a total of 34 radars operated by over a dozen institutions around the world. Figure 2.1 shows the locations and fields of view (FOVs) of all currently operational radars in the Northern (left) and Southern (right) Hemispheres in magnetic coordinates.

SuperDARN radars operate continuously to measure line-of-sight (LOS) velocities, backscattered power, and spectral width from decameter-scale plasma irregularities in the ionosphere [*Chisham et al.*, 2007]. The $\mathbf{E} \times \mathbf{B}$ drift velocities measured from SuperDARN radars can be combined into a global map of ionospheric plasma convection using the technique described by *Ruohoniemi and Baker* [1998] and *Shepherd and Ruohoniemi* [2000]. Figure 2.2

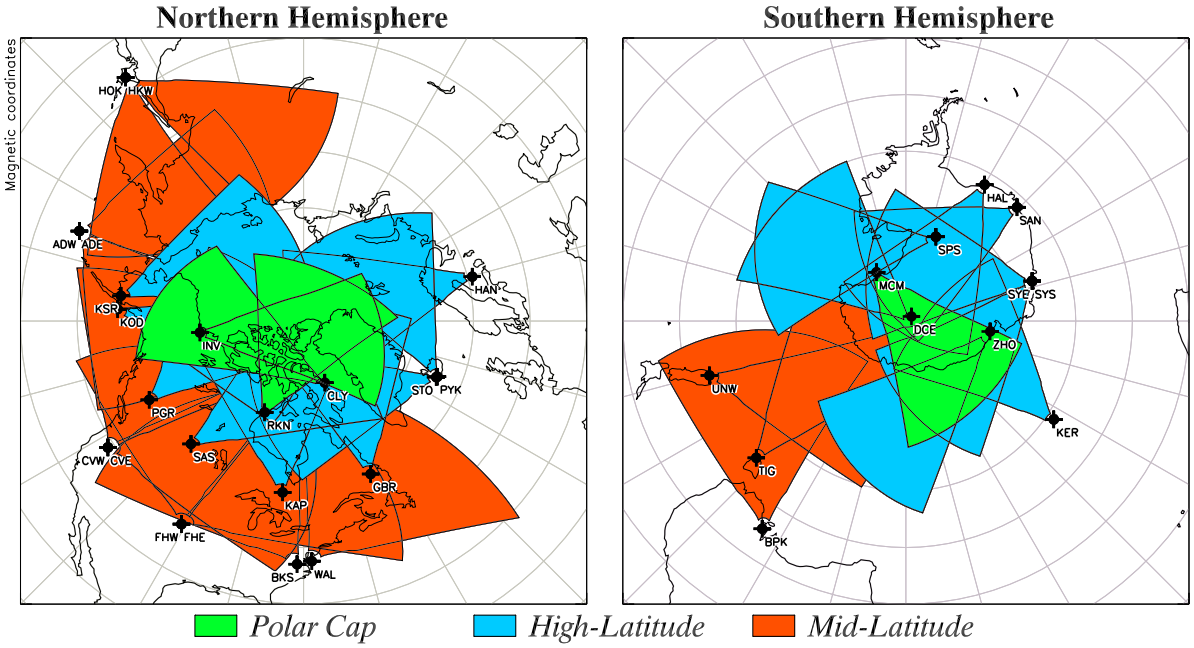

Figure 2.1: Fields of view of currently operational SuperDARN radars in northern (left) and southern (right) hemispheres as of 31 December 2015. Mid-latitude, high-latitude, and polar radar FOVs are shaded red, blue, and green respectively.

shows a sample map obtained for the 19:30–19:32 UT storm interval on 26 September 2011. The contours of constant electrostatic potential constitute streamlines for F region plasma convection. The pattern is predominantly two-cell with a pronounced dayside "throat" feature that can be expected to channel plasma into the polar cap from lower latitudes. Velocity vectors are drawn where velocity data were available from the radars; additional data were provided by a statistical model that is keyed to the prevailing IMF conditions. The coverage by the radars is extensive over North America and provides strong constraints for the fitted pattern, in particular, for the convergence of flows on the dayside that defines the throat. Further discussion of SuperDARN characteristics can be found in Section 3.2.

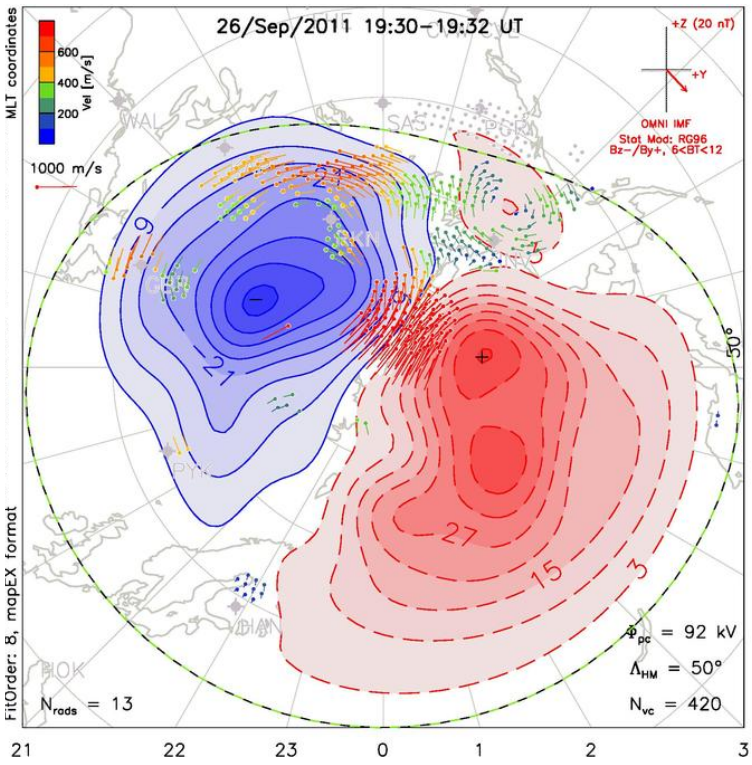

Figure 2.2: Map of plasma convection obtained for the 19:30–19:32 UT storm interval on 26 September 2011 using the standard SuperDARN fitting technique as described in the text and plotted in MLT with magnetic noon at the top. The contours indicate lines of constant electrostatic potential; the contour step is 6 kV and solid/dashed contours indicate negative/positive signs on the potential. The positions and three-letter names of the radars contributing to the solution are indicated.

2.2 Global Positioning System

2.2.1 Satellite Navigation

One of today's most powerful tools for imaging large-scale ionospheric density structure can be traced to the dawn of the satellite era nearly 60 years ago. The concept of a satellite navigation system was first proposed after the launch of Sputnik 1 on October 4, 1957. Scientists at The Johns Hopkins Applied Physics Laboratory were able to trace the orbit of the spacecraft by measuring the Doppler shift in the frequency of its continuously transmitted

signal [*Guier and Weiffenbach*, 1960]. Soon afterward, the U.S. Navy launched the first satellite for a two-dimensional navigation system known as the Navy Navigation Satellite System (NAVSAT) or TRANSIT. These spacecraft were located at an altitude of about 1,000 km with an orbital period of roughly 100 minutes and transmitted navigation messages at 150 and 400 MHz. Users on the Earth's surface were able to calculate their location to an accuracy of only about 50-200 km and each satellite remained in view for no more than 20 minutes at a time. Because navigation signals were transmitted on two different frequencies, users were able to estimate delays introduced by electron densities in the ionosphere by measuring the difference in the arrival time of the two received signals. This novel concept would be re-used for later satellite navigation systems. The TRANSIT system was fully operational with a total of 7 satellites and 6 spares in orbit from 1968 until its retirement in 1996 [*Yionoulis*, 1998].

2.2.2 GPS

To overcome the shortcomings of TRANSIT, a new satellite navigation system was developed by Aerospace Corp. and the Department of Defense (DoD) Joint Program Office (JPO) called the Global Positioning System (GPS). GPS differed from TRANSIT in two key aspects: each spacecraft carried four atomic clocks for highly accurate time synchronization, and users were able to calculate a fully three-dimensional navigation solution by solving a series of four independent equations for the receiver clock bias and their three position coordinates. Each satellite transmitted its ephemeris and timing information on the same two frequencies: L1 (1575.42 MHz) and L2 (1227.6 MHz). Pseudorandom noise codes (PRNs) called the precision (P) code and coarse acquisition (C/A) code are modulated onto these two signals. The L1 and L2 signals are modulated by the P-code while only the L1 signal is modulated by the C/A code (Figure 2.3). The DoD encrypted the P code to ensure the

most accurate navigation solutions would be reserved for military personnel. An intentional degradation called selective availability was also imposed on the C/A code available to civilian users which created navigation errors on the order of hundreds of meters. The first Block-I GPS satellite was launched in 1978, with additional spacecraft regularly launched until a fully operational constellation of 24 satellites was achieved in 1993 [*Getting*, 1993].

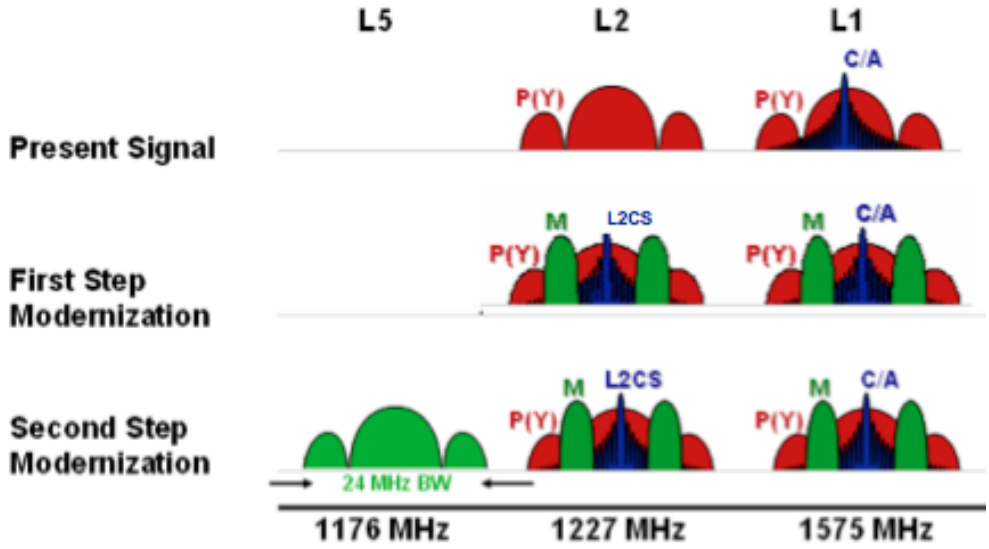

Figure 2.3: Modernization of GPS signals. "Present Signal" refers to the signal structure at the time of the constellation's completion in 1995 [*Coster*, 2011].

In its present state, the GPS constellation consists of between 24 and 32 satellites in six orbital planes with an inclination of 55°. The spacecraft orbits are nearly circular and are located 26,600 km from the center of the Earth. The control segment for GPS consists of a master control station (MCS) at Schriever Air Force Base, an alternate MCS, and six monitor stations at accurately-located geographic positions. Selective availability was permanently turned off on May 4, 2000 by Executive Order from President Clinton [*Kintner*, 1999]. A modernization process is underway to improve the quality of signals available to both military and civilian users with several new PRN codes modulated on the L1 and L2 signals (Figure 2.3). In addition, a new L5 signal at 1776.45 MHz will be available to civilian users

for support of safety-of-life applications. A modified Block IIRM spacecraft launched on March 24, 2009 is the first GPS satellite to transmit the new L5 signal [*Shaw et al.*, 2000; *Coster*, 2011].

2.2.3 GPS TEC

Total electron content (TEC) is a commonly-used parameter for characterizing the Earth's ionosphere. It is defined as the total number of electrons within a cross-sectional volume along a path between two points and given in units of $1{\times}10^{16}$ electrons/m^2, or 1 TECU. Researchers at MIT Haystack Observatory maintain one of several databases of global TEC (NASA Jet Propulsion Laboratory in California and the National Institute of Communications Technology in Japan are two others). The group at MIT Haystack was the first to incorporate GPS receivers from outside the International GNSS Service (IGS) and Continuously Operating Reference System (CORS) networks of strictly-managed receivers to identify plumes of storm enhanced density (SED) that form over the United States during geomagnetic storms [*Coster et al.*, 2001]. Data files in RINEX and other formats are downloaded from thousands of GPS receiver sites around the world for automated processing with the MIT Automated Processing of GPS (MAPGPS) software package. First, a multiplicative factor called a mapping function is used to convert each individual line-of-sight TEC measurement into a zenith TEC estimate. An ionospheric pierce point at 350 km altitude is assumed and an elevation angle cutoff of 7° is imposed. The mapping function used in the automated processing is:

$$z = \frac{1}{\sqrt{(1.0 - (F\cos(el))^2)}}$$

where the adjustment parameter, F, is set to 0.95 for minimization of the average difference in estimated zenith TEC values for coincident measurements.

After the conversion to zenith TEC values, a combination of three different techniques

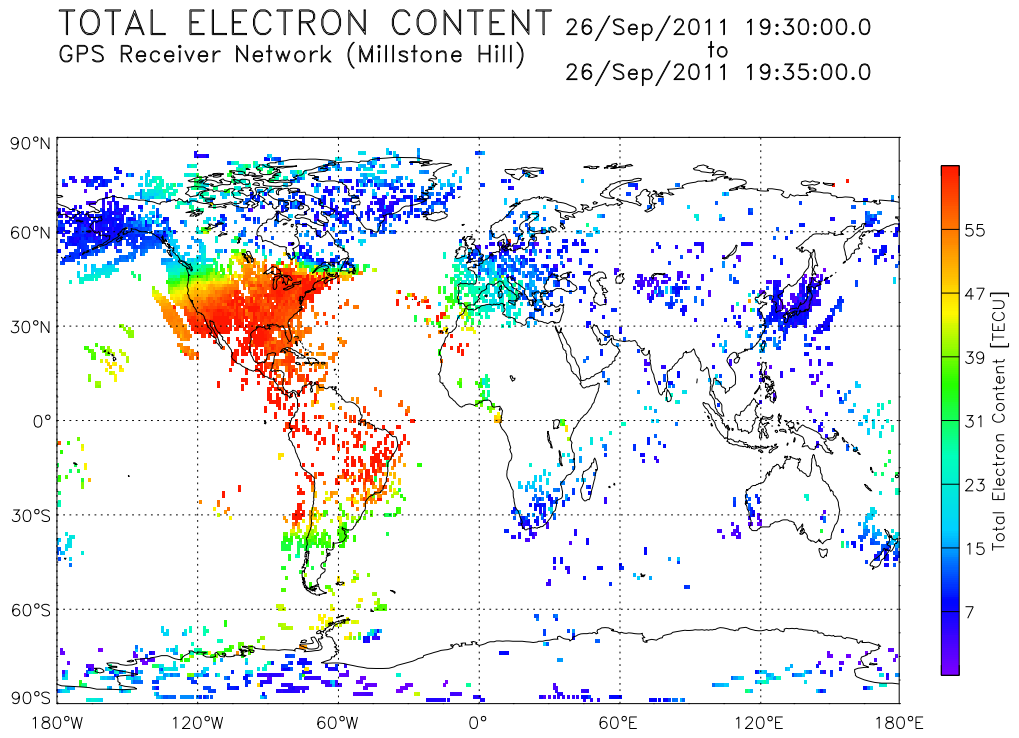

Figure 2.4: Global map of GPS TEC data for the 19:30–19:35 UT storm interval on 26 September 2011. Blank regions indicate missing TEC coverage.

is used for the estimation and removal of receiver biases: minimum scalloping, least squares, and the zero TEC method. A detailed explanation of these three methods can be found in *Rideout and Coster* [2006]. Finally, after receiver biases have been accounted for, the original data stream is decimated to a lower rate for faster processing time. Since June 2005, maps of global GPS TEC have been available from the Madrigal website at MIT Haystack (http://madrigal.haystack.mit.edu/madrigal). Data is provided at 5-minute intervals in 1° by 1° cells in geographic coordinates [*Rideout and Coster*, 2006; *Coster*, 2011]. Pre-generated plots of TEC data averaged over 20-minute intervals into 3° by 3° bins are posted on that day's experiment page. Figure 2.4 shows a sample map of downloaded TEC data for the 19:30–19:35 UT storm interval on 26 September 2011. A plume of storm enhanced density (SED) can be seen stretching across North America from the eastern United States towards Alaska. Further discussion of GPS TEC characteristics can be found in Sections 3.2 and 4.2.2.

2.3 630.0 nm All-Sky Airglow

Optical measurements present a useful alternative to radio techniques for characterizing the ionospheric electron density structure. There are numerous airglow emission bands in the Earth's upper atmosphere related to the chemical interactions between ionized and neutral constituents. Here we focus on the dissociative recombination of molecular oxygen ions in the lower thermosphere (200-300 km)

$$O_2^+ + e^- \rightarrow O + O^*$$

which results in the emission of the 630.0 nm atomic oxygen red line. *Barbier et al.* [1962] demonstrated that the intensity of 630.0 nm airglow emissions is empirically proportional to

$$f_0F_2 \times \exp\left(-\frac{h'F - 200}{41.3}\right)$$

where f_0F_2 is the critical frequency of the F_2 layer and $h'F$ is the virtual height of the F_2 layer. The maximum F_2-layer electron density (N_mF_2) can be found from the critical frequency f_0F_2 using the equation

$$N_mF_2 = \frac{1}{80.6}(f_0F_2)^2$$

where N_mF_2 is in units of m^{-3} and f_0F_2 is in units of Hz. Therefore, the intensity of 630.0 nm red line airglow emissions is proportional to the peak F_2-layer electron density (N_mF_2). This relationship has been applied to the study of a wide range of phenomena such as polar cap patches [*Weber et al.*, 1984, 1986; *Hosokawa et al.*, 2006] and travelling ionospheric disturbances (TIDs) [*Kubota et al.*, 2001; *Ogawa et al.*, 2002; *Shiokawa et al.*, 2009].

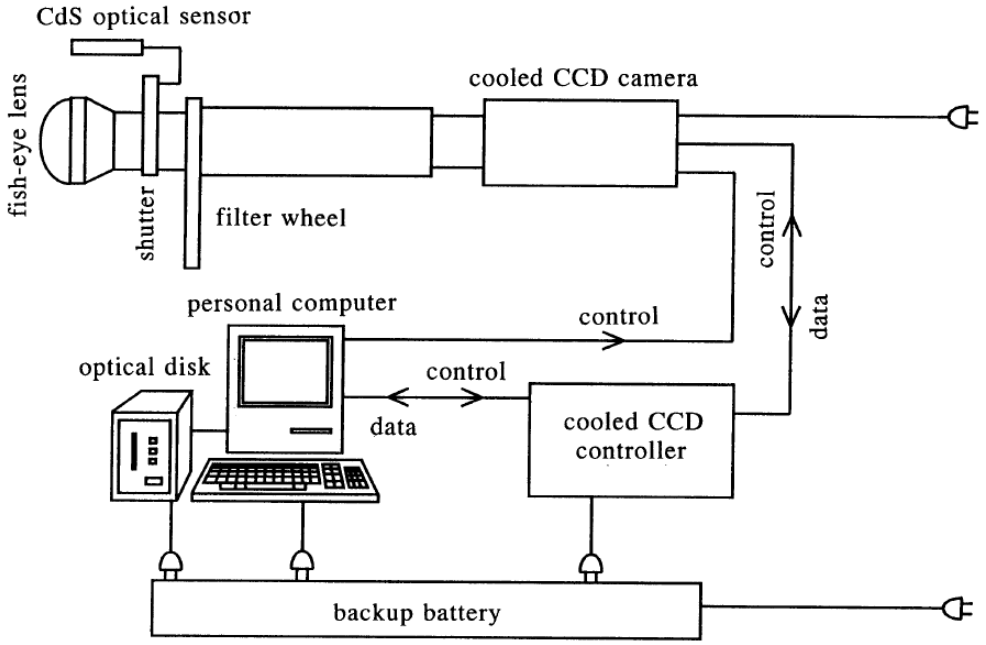

Figure 2.5: Schematic diagram of the OMTI all-sky cooled CCD camera system with 5-position filter wheel. The camera operation is controlled by the personal computer. Image data are saved into the optical disk [*Shiokawa et al.*, 1999].

More specifically, 630.0 nm airglow intensity can be measured using a variety of optical instruments such as all-sky imagers (ASIs), scanning photometers, and Fabry-Perot interferometers. For the results presented in Chapter 3, we use observations from cooled charge-coupled device (CCD) cameras with narrow band-pass filters capable of obtaining two-dimensional images of the airglow emissions in units of photon flux or rayleighs (R). Figure 2.5 shows a schematic diagram of one such ASI from the Optical Mesosphere Thermosphere Imagers (OMTI) network operated by Nagoya University [*Shiokawa et al.*, 1999]. Further discussion of 630.0 nm ASI characteristics can be found in Section 3.2.

Figure 2.7 shows a 2-min snapshot of 630.0 nm all-sky airglow emissions recorded by an OMTI camera located in Resolute Bay (RSB) at 03:32 UT on 27 September 2011 during the geomagnetic storm recovery phase (earlier measurements from this storm interval were not available as the imager FOV was contaminated by daylight). Similar to Figures 2.2

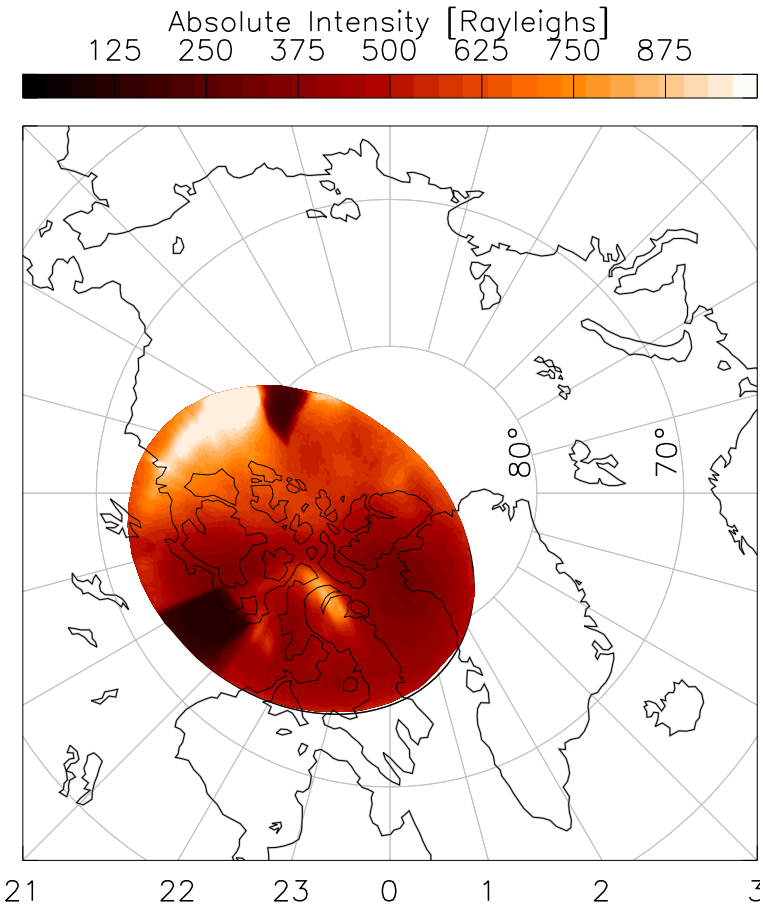

Figure 2.6: 630.0 nm all-sky airglow emissions recorded by OMTI camera in Resolute Bay, Canada (RSB) during the geomagnetic storm recovery phase at 03:32 UT on 27 September 2011 in MLAT/MLT coordinates. Dark wedge-like shapes at 15 and 20 MLT are obstructions by the two nearby incoherent scatter radars at Resolute Bay.

and 2.4, data are again plotted in MLAT/MLT coordinates. Also note that the dark wedge-like shapes at 15 and 20 MLT are obstructions by the two nearby incoherent scatter radars at Resolute Bay. Here we see a bright optical signature near 80° MLAT and 22 MLT likely corresponding to a polar cap patch. These localized optical measurements generally offer much finer-scale resolution for tracking the structuring of patches or other density structures compared to the globally gridded GPS TEC data discussed previously.

2.4 Other Data Sets

Over the years, several geomagnetic indices have been created to describe different storm-time perturbations of the M-I system. Numerous spacecraft have also been launched to monitor the upstream solar wind conditions to forecast space weather effects in the magnetosphere and ionosphere. These supplementary data sets can be valuable tools for identifying unique intervals for a case study (e.g., Chapter 3) or classifying observations for a larger statistical survey (e.g., Chapter 4). In this section we discuss a few of the indices and interplanetary parameters used throughout this dissertation.

2.4.1 Dst/Sym-H Indices

The Disturbance storm time (*Dst*) index is an hourly measure of the average global H variation obtained from four equatorial ground magnetometer stations and has traditionally been used to classify geomagnetic storms into varying categories of weak, moderate, or strong activity [*Gonzalez et al.*, 1994]. An alternative to *Dst* is the Sym-H index, which is a measure of the symmetric disturbance in the H field obtained at 1 min cadence from 11 midlatitude ground magnetometer stations [*Iyemori*, 1990; *Iyemori et al.*, 2010]. The Sym-H index has been shown to closely track *Dst* for magnitudes ≤ -300 nT and can be treated as a higher-resolution "proxy" or alternative [*Wanliss and Showalter*, 2006]. Figures 2.7a and 2.7b show the *Dst* and Sym-H indices from 06:00-24:00 UT during the geomagnetic storm on 26 September 2011. While the Sym-H index clearly provides finer temporal resolution, both indices identify the storm main phase onset (sharp decrease to negative values) as occurring around 15:00 UT. The storm recovery phase begins about two hours later at 17:00 UT as both the *Dst* and Sym-H values remain consistently negative around -100 nT into the next day. In this manner geomagnetic storms are identified for both case and statistical studies

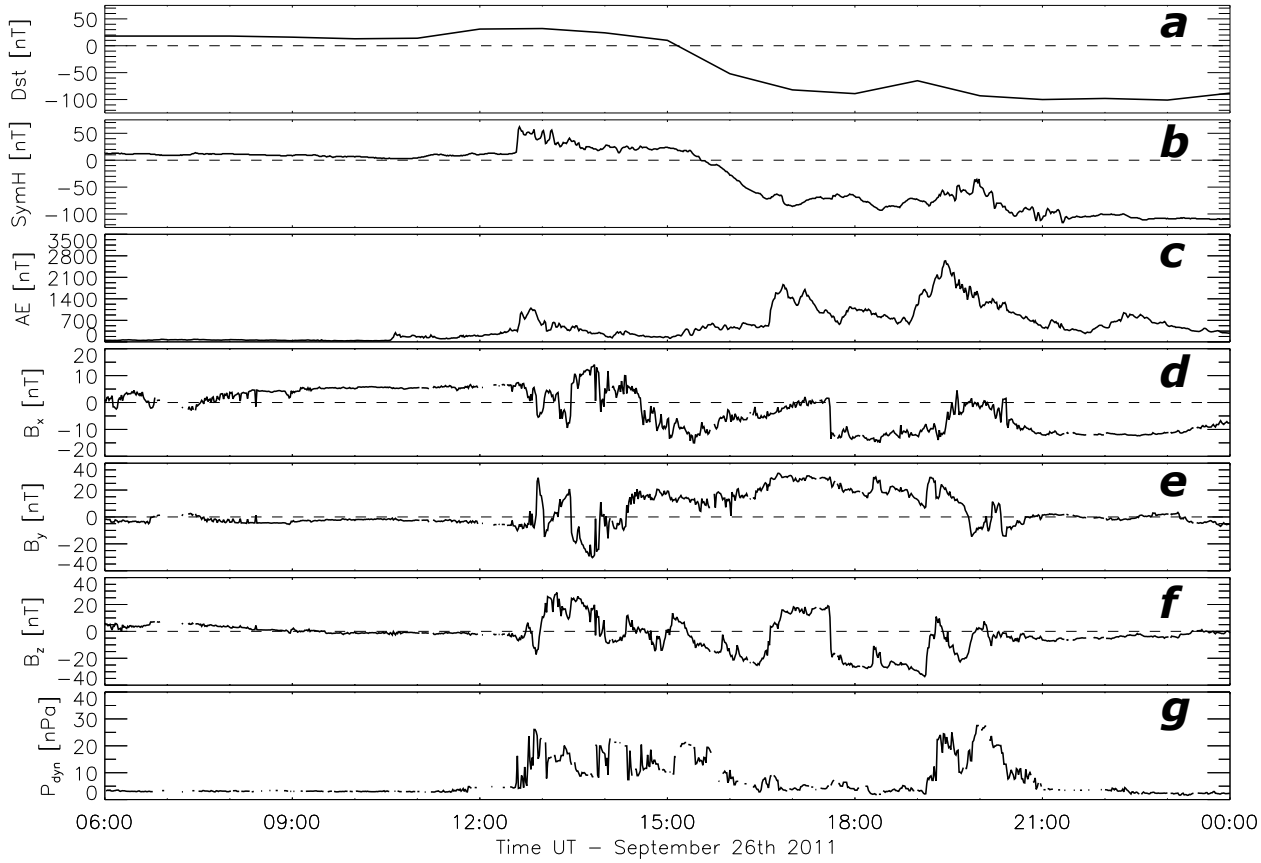

Figure 2.7: Geomagnetic and solar wind OMNI parameters during geomagnetic storm on 26 September 2011: (a) Dst index, (b) Sym-H index, (c) AE index, OMNI IMF (d) Bx, (e) By, (f) Bz, and (g) dynamic pressure. Identification of storm phases is explained in the text.

of ionospheric storm effects throughout the dissertation.

2.4.2 AE Index

The Auroral Electrojet (AE) index is a measure of global electrojet activity [*Davis and Sugiura*, 1966]. The horizontal or H component of the Earth's magnetic field is first recorded at 1 min cadence at several (7-13) ground magnetometer stations located throughout the auroral zone in the northern hemisphere. Next, the data is normalized by subtracting the average value from the five geomagnetically quietest days of the month for each station. Upper (AU) and lower (AL) envelopes are then calculated by superposing data from all

stations. The AU and AL indices reflect the strongest current intensity of the eastward and westward auroral electrojets respectively. The AE index is thus obtained by taking the difference between the AU and AL indices. The last of these auroral indices is the AO index, which is the mean value of AU and AL and provides a measure of the equivalent zonal current [*Kamei et al.*, 1992]. Figure 2.7c shows the AE index during the 26 September 2011 geomagnetic storm. Three peaks in the AE index can be seen near 12:45, 17:00, and 19:30 UT. The first two peaks coincide with the storm sudden commencement (sharp increase to positive Dst/Sym-H values) and main phase onset, while the third and largest peak occurs well into the storm recovery phase. These are likely signatures of substorm onset corresponding to magnetic reconnection processes in the tail. In this way we see how different magnetic perturbation indices are necessary to capture the effects of the different M-I current systems.

2.4.3 OMNI Interplanetary Measurements

Knowledge of solar wind parameters such as the orientation and magnitude of the interplanetary magnetic field (IMF) is crucial to understanding the degree of coupling to the Earth's magnetosphere. Here we focus on the OMNI 2 database which is a compilation of magnetic field and plasma parameters measured at 1 min cadence by several spacecraft in the upstream solar wind. These interplanetary values have been lagged to the subsolar point on the Earth's bow shock [*King and Papitashvili*, 2005]. While lower-resolution historical data are available since 1964, currently only the Advanced Composition Explorer (ACE) and Wind spacecraft located in L1 (Lagrange point) orbit are contributing IMF and plasma parameter measurements to the OMNI 2 database. Figures 2.7d–2.7g show OMNI IMF Bx, By, Bz, and dynamic pressure measurements during the 26 September 2011 geomagnetic storm. The arrival of a solar coronal mass ejection near 12:45 UT can be seen as an abrupt

increase in the magnitude of the IMF components and solar wind dynamic pressure. A southward turning of IMF Bz to largely negative values (-30 nT) near 15:00 UT triggers the storm main phase onset previously identified in the *Dst*/Sym-H ring current indices. A second structure in the solar wind is seen in the dynamic pressure later at 19:00 UT, preceding the final intensification of AE near 19:30 UT. While the IMF Bz component remains weakly negative as the storm enters the recovery phase around 21:00 UT, it is greatly reduced in magnitude from its earlier values and the IMF By and solar wind dynamic pressure remain steady near zero. Thus we see how interplanetary measurements of the solar wind IMF and plasma parameters help provide context for the geomagnetic indices described above.

2.5 Methods and Data Access

A core tenet of this research work has been to ensure ease of access and data availability for outside users. In fact, this philosophy has led to several of the collaborative research projects described later in the dissertation. *Thomas* [2012] first introduced the package of online plotting tools for generating combined GPS TEC/SuperDARN figures hosted on the VT SuperDARN website (http://vt.superdarn.org). At the most basic level, users are able to generate either static or animated .gif plots of GPS TEC data. Options are available for applying a spatiotemporal median filtering technique to the TEC data as well as overlaying common SuperDARN parameters such as line-of-sight velocities, backscattered power, and fitted convection patterns. After generating one of these figures a link to that day's GPS TEC data file on Madrigal can be found below the figure. If no data for the selected date are available, the user receives an error message and a link to a summary plot of the available TEC data on Virginia Techs servers is provided. A "quick guide" is also available for download which explains the plotting options, median filtering technique, and any known issues or planned updates. Users are requested to contact the developer before using any

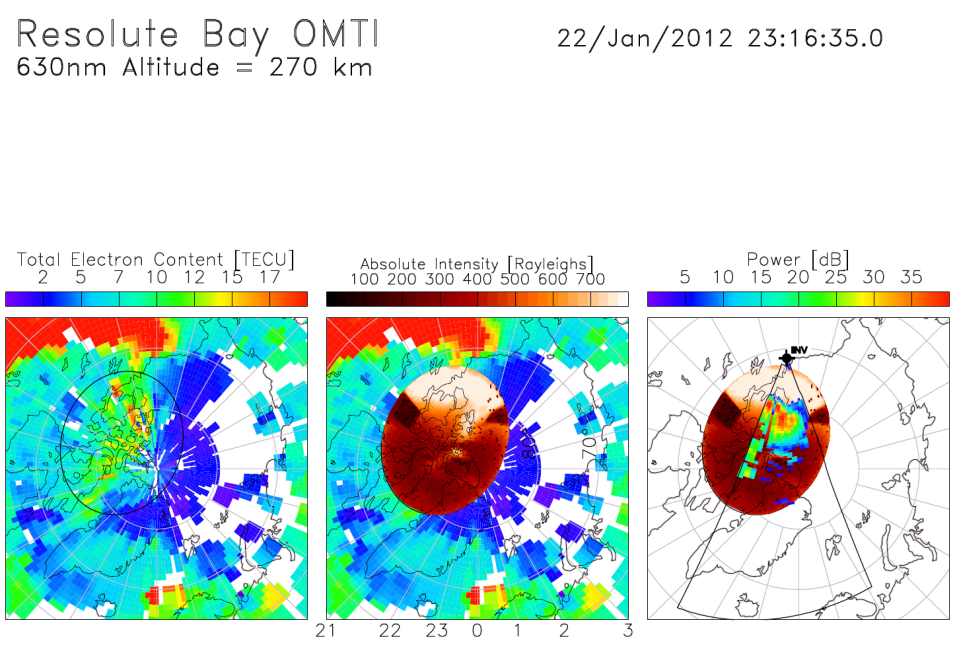

Figure 2.8: Output from the Interactive ASI Plotting page on the VT SuperDARN website for a polar cap patch event on 22 January 2012. (left panel) GPS TEC with field of view (FOV) of OMTI camera at Resolute Bay overlaid, (middle panel) same GPS TEC data with 630.0 nm airglow overlaid, (right panel) 630.0 nm airglow data with SuperDARN Inuvik (INV) radar backscatter power overlaid. Airglow data is measured by the OMTI camera located in Resolute Bay, Canada [*Shiokawa et al.*, 2009].

figures in a conference presentation or journal submission for quality control purposes.

As a direct result of an NSF-sponsored research visit to Japan (award number IIA-1310774) a new tool has been added to the suite of online plotting software which allows users to overlay 630.0 nm airglow measurements from all-sky imagers (ASIs). Currently, optical data are only available from the Resolute Bay (RSB) OMTI camera [*Shiokawa et al.*, 2009] from January 2005 to March 2014, although data from the Svalbard camera (SCAM) [*Taguchi et al.*, 2012] may also become publicly available at a later date. Users have the capability to select the emission altitude mapping, zenith angle cutoff, and whether to apply correction for limb effects. Figure 2.8 demonstrates how SuperDARN, GPS TEC, and 630.0 nm airglow measurements have been integrated for the purposes of this tool. The left panel shows 5 min GPS TEC data in the northern polar cap with the field of view (FOV) of the RSB imager

overlaid. The middle panel shows a 2 min snapshot of 630.0 nm airglow overlaid onto the same TEC. Finally, backscattered power measured by the Inuvik (INV) SuperDARN radar is overlaid onto the same 630.0 nm airglow image in the right panel. Similar to the GPS TEC/SuperDARN tools described above, users may also generate animated movies in this format. Figure 2.9 shows the currently available GPS TEC (left) and airglow (right) data stored on the VT SuperDARN data server. These new analysis tools have already aided in the research performed in Chapter 3 and will make it easier for scientists to improve our understanding of plasma density structuring and related phenomena in the high latitude ionosphere.

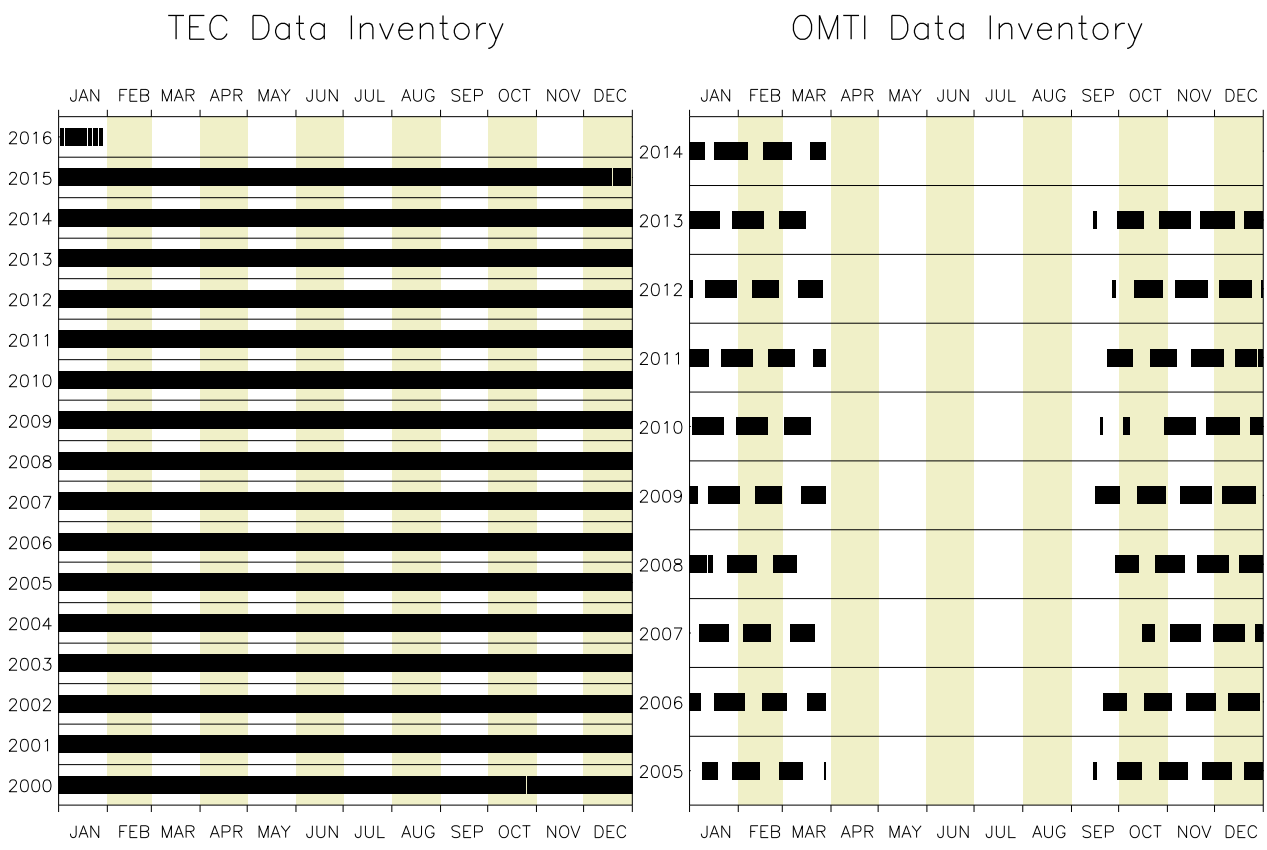

Figure 2.9: Summary plots of (left) GPS TEC and (right) OMTI Resolute Bay 630.0 nm airglow data available on the VT SuperDARN data server for online plotting.

Chapter 3

Multi-instrument, high-resolution imaging of polar cap patch transportation

E. G. Thomas[1], K. Hosokawa[2], J. Sakai[3], J. B. H. Baker[1], J. M. Ruohoniemi[1], S. Taguchi[4], K. Shiokawa[5], Y. Otsuka[5], A. J. Coster[6], J.-P. St.-Maurice[7], and K. A. McWilliams[7]
Radio Science, Published 2015.

[1] Bradley Department of Electrical and Computer Engineering, Virginia Tech, Blacksburg, Virginia, USA.
[2] Department of Communication Engineering and Informatics, University of Electro-Communications, Chofu, Japan.
[3] Center for Space Science and Radio Engineering, University of Electro-Communications, Chofu, Japan.
[4] Department of Geophysics, Graduate School of Science, Kyoto University, Kyoto, Japan.
[5] Solar-Terrestrial Environment Laboratory, Nagoya University, Nagoya, Japan.
[6] Haystack Observatory, Massachusetts Institute of Technology, Westford, Massachusetts, USA.
[7] Institute for Space and Atmospheric Studies, University of Saskatchewan, Saskatoon, Saskatchewan, Canada.

Abstract

Transionospheric radio signals in the high-latitude polar cap are susceptible to degradation when encountering sharp electron density gradients associated with discrete plasma structures, or patches. Multi-instrument measurements of polar cap patches are examined during a geomagnetic storm interval on 22 January 2012. For the first time, we monitor the transportation of patches with high spatial and temporal resolution across the polar cap for 1–2 h using a combination of GPS total electron content (TEC), all-sky airglow imagers (ASIs), and Super Dual Auroral Radar Network (SuperDARN) HF radar backscatter. Simultaneous measurements from these data sets allow for continuous tracking of patch location, horizontal

extent, and velocity despite adverse observational conditions for the primary technique (e.g., sunlit regions in the ASI data). Spatial collocation between patch-like features in relatively coarse but global GPS TEC measurements and those mapped by high-resolution ASI data was very good, indicating that GPS TEC can be applied to track patches continuously as they are transported across the polar cap. In contrast to previous observations of cigar-shaped patches formed under weakly disturbed conditions, the relatively narrow dawn-dusk extent of patches in the present interval (500–800 km) suggests association with a longitudinally confined plasma source region, such as storm-enhanced density (SED) plume. SuperDARN observations show that the backscatter power enhancements corresponded to the optical patches, and for the first time we demonstrate that the motion of the optical patches was consistent with background plasma convection velocities.

3.1 Introduction

Polar cap patches are discrete plasma structures in the F region ionosphere characterized by electron densities elevated above those of the surrounding plasma and ranging in horizontal size from 100 to 1000 km [*Weber et al.*, 1986; *Crowley*, 1996]. Patches are formed in the dayside ionosphere near the footprint of the magnetospheric cusp and propagate toward the nightside across the central polar cap region. They are believed to be closely related to rapid fluctuations in radio signal amplitude and phase, called scintillation [*Aarons*, 1982; *Weber et al.*, 1984; *Buchau et al.*, 1985]. Recently, *Carlson* [2012] examined several of the most commonly proposed patch formation and structuring mechanisms, suggesting that capture of daytime sunlit plasma through transient magnetic reconnection [*Lockwood and Carlson*, 1992] is often the dominant production mechanism, while relatively less dense patches may also be produced by particle precipitation in the cusp [*Rodger et al.*, 1995; *Walker et al.*, 1999; *Moen et al.*, 2001; *Lorentzen et al.*, 2010] and polar cap [*Oksavik et al.*, 2006]. In situ measurements from the recently launched constellation of Swarm spacecraft have been used to demonstrate these formation mechanisms [*Goodwin et al.*, 2015] and characterize patch structuring due to the gradient drift instability [*Spicher et al.*, 2015]. The region where patches exit the polar cap and enter the nightside auroral zone spans a wide range of mag-

netic local times [*Moen et al.*, 2007] and is determined by magnetic reconnection in the tail [*Zhang et al.*, 2013].

In contrast to discrete patches, the polar tongue of ionization (TOI) is a continuous channel of high-density F region plasma which is transported from the dayside midlatitude ionosphere through the cusp and into the polar cap by enhanced convection electric fields [*Foster*, 1993; *Foster et al.*, 2005]. The source of the TOI is the region of midlatitude storm-enhanced density (SED) formed under geomagnetically disturbed conditions. An outstanding issue is the precise conditions which determine whether an SED plume leads to the generation of a continuous TOI feature or discrete patches.

Although it is often assumed that patches move with the background plasma velocity, there have been only limited demonstrations of the equivalence of these velocities, and none with direct measurements of the velocities themselves. For example, *Hosokawa et al.* [2009] demonstrated a strong statistical link between the motion of patches over Resolute Bay and interplanetary magnetic field (IMF) conditions while *Hosokawa et al.* [2010] examined this link for an event with two patches. *Perry et al.* [2013], studying the same two-patch event, illustrated a link between the vertical motion of the patches and their luminosity. The degree of equivalence between optical patch velocities and the background $\mathbf{E} \times \mathbf{B}$ plasma drift is still to be demonstrated conclusively with direct, simultaneous measurements.

Another open question is the spatial extent of polar cap patches under varying geomagnetic conditions. Typically, the dawn-dusk width of patches observed in the polar cap is much greater than the noon-midnight horizontal extent during low levels of geomagnetic activity [*Hosokawa et al.*, 2014]. These cigar-shaped patches have been suggested as evidence of transient flow bursts capturing sunlit plasma near the dayside polar cap boundary across several hours of magnetic local time [*Carlson et al.*, 2004]. However, if the distribution of source plasma in the dayside ionosphere has some asymmetry (e.g., an SED plume), the

shape of patches may also be distorted.

The goal of this paper is to examine polar cap patches generated from an SED plume on 22 January 2012 and monitor their transportation from the dayside to nightside ionosphere at high spatial and temporal resolution. Previous studies have examined patches using only Global Positioning System (GPS) total electron content (TEC) data [*Zhang et al.*, 2013]; GPS TEC and overhead satellite electron content (OSEC) [*Bust and Crowley*, 2007]; optical and Super Dual Auroral Radar Network (SuperDARN) data [*Hosokawa et al.*, 2009]; or optical, SuperDARN, and incoherent scatter radar data [*Dahlgren et al.*, 2012]. Here for the first time, we use a combination of GPS TEC, all-sky airglow imagers (ASIs), and SuperDARN HF radar to verify the conformity of patch characteristics (e.g., spatial extent and velocity) across these three data sets.

3.2 Instrumentation

In this study, airglow measurements are collected with two ASIs within the northern polar cap. The first is the Optical Mesosphere Thermosphere Imagers camera located at Resolute Bay, Canada (RSB: 74.73°N, 265.07°E, geomagnetic latitude 82.96°) [*Shiokawa et al.*, 2009] while the second is a highly sensitive airglow imager operated in Longyearbyen, Norway (LYR: 78.21°N, 15.55°E, geomagnetic latitude 75.67°) since October 2011 [*Taguchi et al.*, 2012]. These ASIs monitor the intensity of atomic oxygen red line emissions at 630.0 nm wavelength which are known to be closely related to the F region electron density profile and vertical plasma motion [*Buchau et al.*, 1983; *Perry et al.*, 2013]. We have followed the procedure described by *Kubota et al.* [2001] to correct the observed intensities for zenith angle sensitivity, the van Rhijn effect, and atmospheric extinction [*Tohmatsu and Ogawa*, 1990].

Global maps of GPS TEC binned into 1° × 1° cells at 5 min cadence are obtained from the Madrigal database at Massachusetts Institute of Technology Haystack Observatory [*Rideout and Coster*, 2006] and presented using the method described by *Thomas et al.* [2013]. One TEC unit (TECU) is given as 1×10^{16} el/m^2 and represents the total number of electrons contained in a column extending upward from the Earth's surface through the ionosphere with a cross-sectional area of 1 m^2. Similar to 630.0 nm airglow, GPS TEC is often considered representative of horizontal ionospheric electron density structure [*Mendillo*, 2006].

SuperDARN is an international network of coherent HF radars which operate continuously to measure line-of-sight (LOS) velocities, backscatter power, and spectral width from decameter-scale plasma irregularities in the ionosphere [*Chisham et al.*, 2007]. The measured convection drift velocities of these plasma irregularities are routinely used to derive global electric field maps that describe the large-scale circulation of plasma in the ionosphere [*Ruohoniemi and Baker*, 1998]. We focus on observations from the PolarDARN Inuvik radar (INV: 68.4°N, 226.5°E, geomagnetic latitude 71.5°) which shares a common field of view (FOV) with the RSB imager.

It is important to consider the different instrument limitations and sampling resolutions when reconciling patch observations across each of the three data sets. A 630.0 nm airglow imager requires dark skies to differentiate F region electron density patches from the background solar extreme ultraviolet (EUV) photionization incident on the dayside ionosphere. For zenith angles less than 45° (i.e., near the center of the imager FOVs) the average spatial resolution is ∼4 km for RSB and ∼2 km for the LYR camera. The HF radar technique employed by SuperDARN depends on the satisfaction of two criteria: 1) favorable radio wave propagation conditions for the transmitted signal to reach the patch and 2) the presence of field-aligned decameter-scale irregularities from which the signal can backscatter toward

the radar site [e.g., *Moen et al.*, 2000]. Observations from the INV radar are separated in azimuth by 3.3° and sampled in 45 km range gates, while GPS TEC values within the polar cap are averaged over ∼100 km spatial scales. Due to the orbital inclination of the GPS constellation (55°), the maximum possible elevation angle from a receiver at the geographic pole is less than 45°, limiting the availability of TEC coverage at high latitudes.

There are also various mapping ambiguities involved with each of the three datasets that can lead to some spatial differences. For example, TEC data are calculated assuming a slab ionosphere at 350 km altitude, while we have assumed 270 km and 280 km peak emission altitudes for the RSB and LYR images, respectively [*Sakai et al.*, 2014]. Similarly, there is often an uncertainty of about one range gate (±45 km) when mapping SuperDARN backscatter due to limitations of the standard virtual height model [*Chisham et al.*, 2008]; this can be corrected when reliable elevation angle of arrival information is available. To summarize, fine spatial resolution (2/4 km) is available from the ASIs over limited areas, mesoscale (45 km) from HF radar over larger areas, and coarse resolution (100 km) over continental areas, making it possible to carry out multiresolution imaging of plasma structure in the polar cap ionosphere even where one measurement technique may be degraded or unavailable.

3.3 Observations

3.3.1 Event Overview

A moderate geomagnetic storm was triggered on 22 January 2012 by an interplanetary coronal mass ejection (ICME). The arrival of the ICME at Earth's magnetosphere can be seen in Figure 3.1 (first panel) at 06:15 UT as an abrupt intensification in *Sym-H* followed

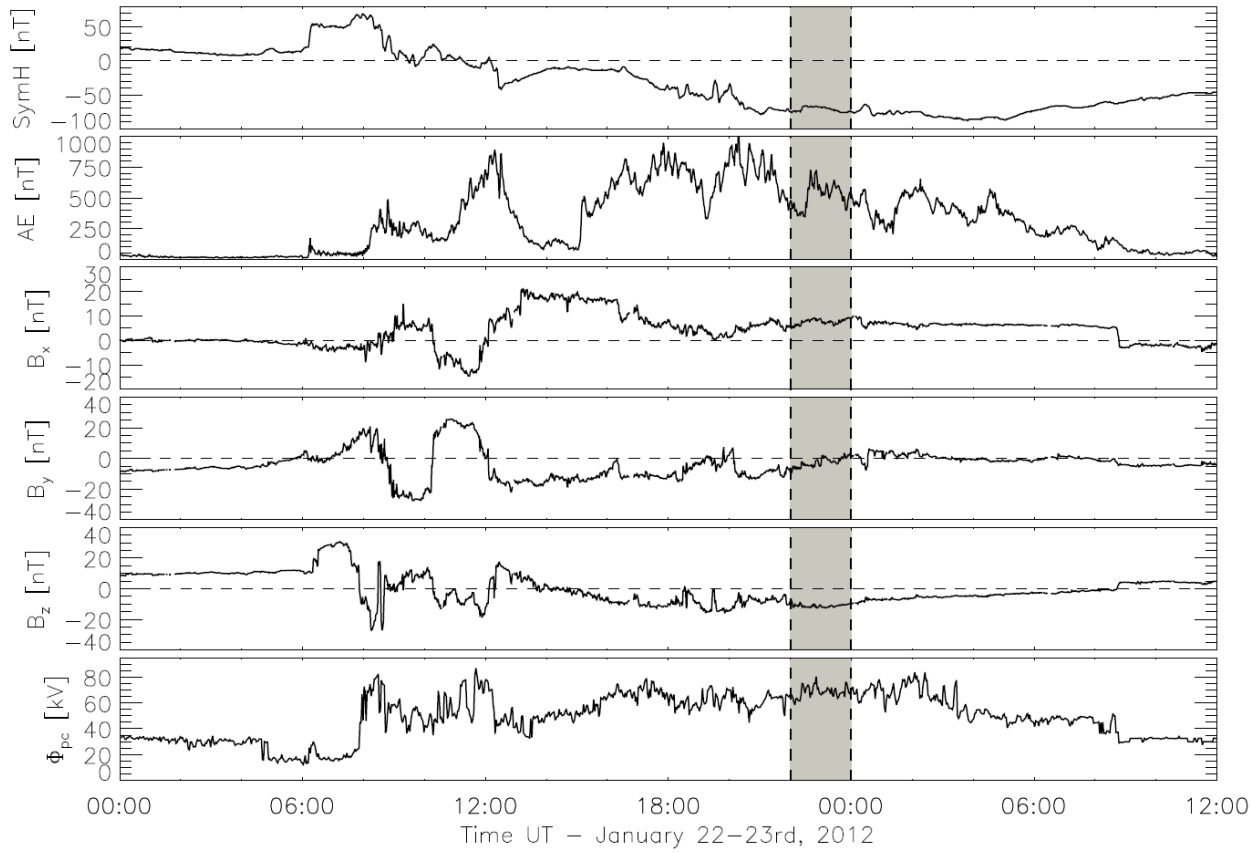

Figure 3.1: Geomagnetic and solar wind parameters on 22–23 January 2012: (first panel) *Sym-H* index, (second panel) *AE* index, OMNI IMF (third panel) B_x, (fourth panel) B_y, (fifth panel) B_z, and (sixth panel) SuperDARN cross polar cap potential. The shaded region indicates the interval from 22 to 24 UT when a series of polar cap patches were identified from both GPS TEC maps and 630.0 nm airglow images.

by a decline from +60 to −80 nT. We have highlighted a 2 h interval (22–24 UT) from the main phase of the storm during which a train of patches was observed in the polar cap ionosphere across the three data sets. Figure 3.1 (second panel) indicates sustained recurrent substorm activity in the auroral electrojet (AE) index beginning around 15:00 UT and continuing for the next 18 h. The next three panels show the IMF B_x, B_y, and B_z components at the bow shock in geocentric solar magnetospheric (GSM) coordinates from the OMNI 2 database [*King and Papitashvili*, 2005]; the magnitudes of all three components were very large (>20 nT) following storm onset. IMF B_y was decreasingly negative during

the first half of the 2 h interval while the B_z component remained southward at around -10 nT. Conversely, IMF B_x slowly varied between +5 and +10 nT during the same period. The Northern Hemisphere cross polar cap potential derived from SuperDARN observations (Figure 3.1, sixth panel) was elevated throughout the main phase of the storm, corresponding to enhanced storm time convection and circulation of plasma in the high-latitude ionosphere [*Ruohoniemi et al.*, 2001]. The occurrence of F region patches over Svalbard during this period was confirmed in measurements of electron density carried out by the European Incoherent Scatter (EISCAT) Svalbard radar as described by *Sakai et al.* [2014].

Figure 3.2 shows an overview of GPS TEC, ASI, and SuperDARN observations at 22:08 (a–d) and 22:42 UT (e–h) on 22 January 2012 in magnetic local time (MLT)/magnetic latitude (MLAT) coordinates. A narrow region of increased TEC corresponding to an SED plume is seen extending across North America toward 70° Λ and noon MLT in Figure 3.2a. The boxed region from this panel is enlarged in Figure 3.2b to highlight the successive train of polar cap patches stretching from the dayside SED plume to the nightside ionosphere. Note that we have decreased the TEC color scale from that applied in Figure 3.2a in order to display the patch features more prominently. In Figure 3.2c the 630.0 nm airglow image from the LYR all-sky camera is overlaid on the map of GPS TEC. A remarkable spatial correspondence is seen between the patch-like features in the TEC and optical observations around 24 MLT between Greenland and Svalbard (the bright region at the bottom of the LYR FOV corresponds to auroral precipitation). Figure 3.2d shows regions of HF ionospheric backscatter observed by the INV radar with its FOV overlaid onto the 630.0 nm airglow data. There is a very good correspondence between the HF backscatter and bright TEC patch within the INV FOV near the geomagnetic pole at 15 MLT.

More than 30 min later at 22:42 UT the SED plume is still visible in GPS TEC over North America (Figure 3.2e), and a train of patches is still observed stretching across the

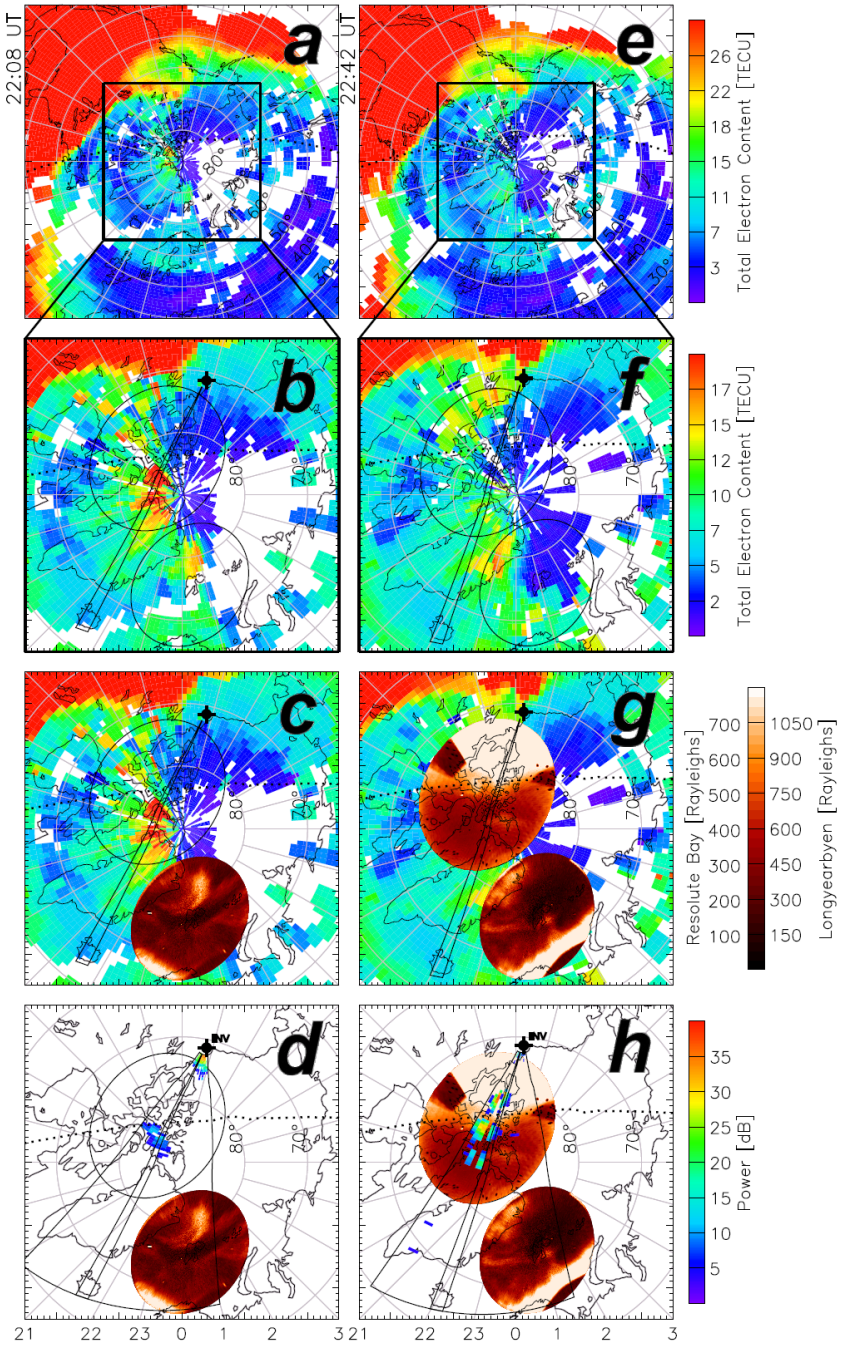

Figure 3.2: GPS TEC, 630.0 nm airglow, and SuperDARN ionospheric echoes on 22 January 2012 at 22:08 UT (a–d) and 22:42 UT (e–h) in MLT/MLAT coordinates. (a,e) Maps of GPS TEC showing SED plume over North America extending toward dayside cusp region. (b,f) Enlarged view of TEC within polar cap region, with ASI FOVs and Beam-10 of the INV radar indicated. (c,g) 630.0 nm airglow observations from RSB and LYR imagers overlaid onto GPS TEC maps. (d,h) Backscatter power measured by the INV radar overlaid onto the airglow images. Day/night terminator (solar zenith angle = 100°) indicated by dotted line. Empty regions in the GPS TEC maps denote lack of data coverage rather than low electron density values.

polar cap. There is a very clear correspondence between the TEC and airglow patches on the edge of the LYR FOV over Greenland seen in Figure 3.2g. By this time, data also became available from the RSB imager, although the upper half of its FOV is contaminated by daylight as indicated by the dotted solar terminator line (Note that the dark wedge-like shapes at 10 and 15 MLT are obstructions by the two nearby incoherent scatter radars at Resolute Bay). The reader is referred to Movie S1 in the supporting information which clearly shows these optical patches emerging from the sunlit region and their subsequent transportation to the nightside auroral oval. In particular, this movie demonstrates the common antisunward motion of the INV echoes and RSB optical patches seen in Figure 3.2h. The benefit of the high-resolution airglow data also becomes more apparent when tracking the fine-scale structuring of the patches as they reach the nightside, which cannot be resolved from the globally gridded TEC data.

3.3.2 Airglow-SuperDARN Time Series

Although two-dimensional images are useful for determining the spatial extent of patches, they provide limited insight into the magnitude of patch velocities. We next examine these data in a time series/keogram format along a selected INV radar beam. Figure 3.3 shows (a) radar backscatter power and (b) RSB 630.0 nm optical intensity along Beam 10 of the INV radar as a function of slant range (distance traveled by a transmitted signal through the ionosphere to a region of backscattering irregularities). The times of the maps presented in Figure 3.2 (22:08 UT and 22:42 UT) are indicated by vertical dashed lines, and the y axis of each panel has been oriented such that downward moving features correspond to antisunward motion along the radar beam. Accordingly, the bright region at the top of the RSB keogram corresponds to daylight contamination. Also note that optical data were not recorded by the RSB ASI until 22:40 UT once the Sun was sufficiently (12°) below the horizon. Linear

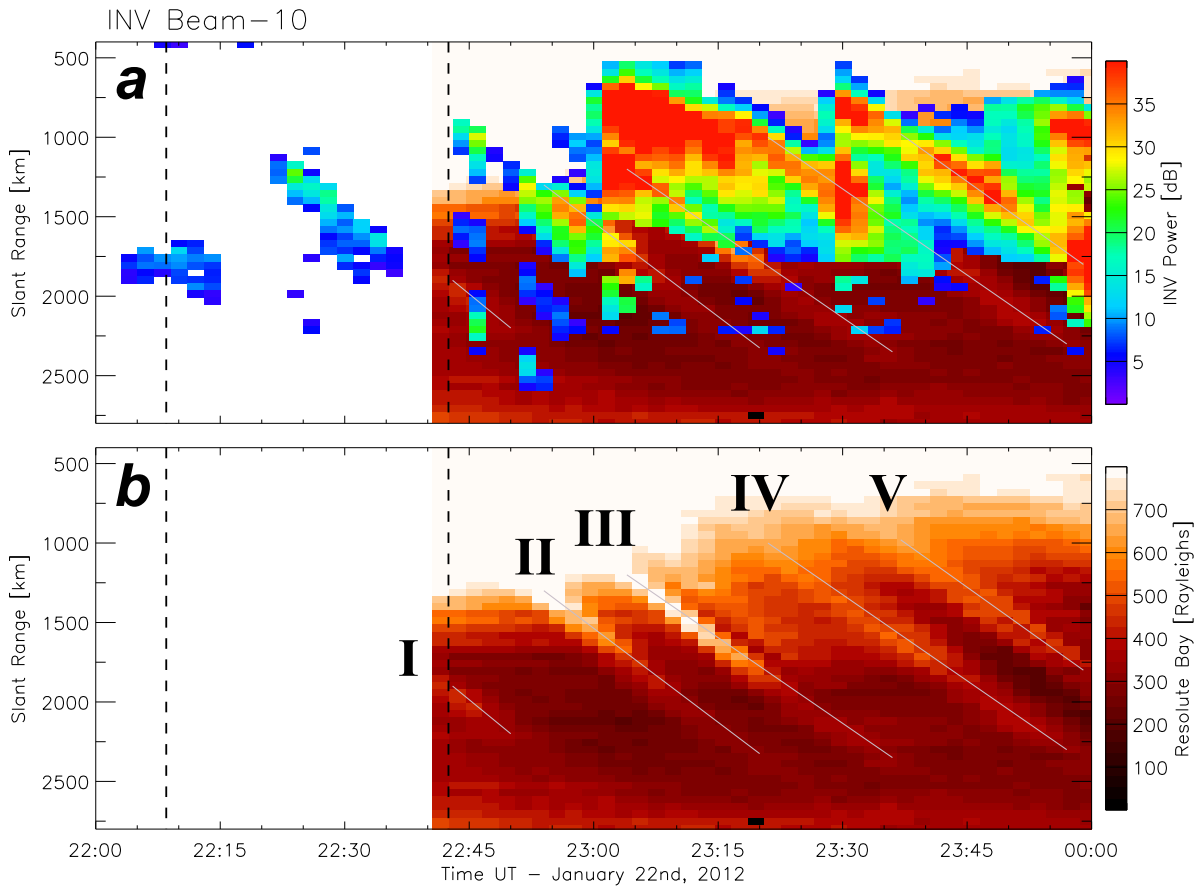

Figure 3.3: Time series/keogram representation of RSB 630.0 nm airglow and SuperDARN echoes along Beam 10 of the INV radar. (a) Backscatter power overlaid onto 630.0 nm airglow measurements and (b) same ASI 630.0 nm measurements closest to each range cell along the radar beam. Vertical dashed lines indicate the times of the maps shown in Figure 3.2, and y axes are oriented such that all features are traveling antisunward. Solid white lines (I–V) represent patch trajectories estimated from RSB optical data.

traces of five RSB optical patches (I–V) are overlaid onto both panels in Figure 3.3.

There is a remarkable one-to-one spatial correspondence between the INV power and RSB airglow for the optical patches labeled I through V (Figures 3.3a and 3.3b). We infer that the dayside patches are closely associated with enhanced radar backscatter due to more favorable conditions for the formation of ionospheric irregularities. We note that a weak patch-like feature was seen in the radar observations between patches I and II, where the optical measurements were fairly featureless. Comparing the overall intensities of the

Table 3.1: Velocity magnitudes of polar cap patches shown in Figure 3.3 as determined from great circle distance of optical traces and averaged HF radar measurements.

Patch	**Velocity (m/s)**	
	RSB (airglow)	INV (HF radar)
I	671	667
II	694	685
III	638	639
IV	612	665
V	647	679

patch features between the two sets of measurements, it seems likely that the corresponding optical feature was too weak to be detected. Although the RSB ASI did not turn on until 22:40 UT, it is possible to trace the first optical patch located near 2000 km slant range (I) to its position 20 min earlier using the radar backscatter power data. The INV radar even observed ionospheric patches within the daylight-contaminated region of the RSB FOV several minutes before they appeared in the optical measurements. Such an early warning capability could prove useful in real-time predictions of patch motion.

The INV radar measures the LOS $\mathbf{E} \times \mathbf{B}$ drift of small-scale plasma irregularities, which need not be associated with any larger density features such as a polar cap patch. Estimated speeds of the optical patches (I–V) in Figure 3.3 are calculated from the great circle distance of the linear traces and listed in Table 3.1 along with their average LOS velocities measured by the INV radar. Velocity magnitudes are 600–700 m/s and agree to within 10% between the two data sets for each patch. The motion of polar cap patches are believed to be driven by the background plasma convection [*Milan et al.*, 2002] as the incompressible nature of the ionospheric plasma has previously been demonstrated using EISCAT and SuperDARN radar observations [*Moen et al.*, 2001; *Davies et al.*, 2002; *Lockwood et al.*, 2005; *Zhang et al.*, 2011]. In the past literature, however, there have been no studies that directly demonstrate

the connection between optical patch motion and background convection velocity. The correspondence observed here lends credence to the idea that patch motion in the polar cap is controlled by convection and that the backscatter power enhancements seen by the HF radars can be used to track the patches. These results confirm a very good correspondence between these two sets of velocity measurements with reliable accuracy.

3.3.3 Airglow-TEC Comparison

We now consider the relationship between GPS TEC and 630.0 nm airglow measurements of polar cap patches. Historically, most studies comparing these two data-sets have focused on signatures of traveling ionospheric disturbances (TIDs) at middle to low latitiudes [e.g., *Ogawa et al.*, 2002]. The recent expansion of ground-based GPS receivers to higher latitudes in the North American and European sectors allows for the inclusion of polar cap observations in globally gridded maps of GPS TEC. This now provides the opportunity to test the agreement between vertically integrated TEC observations of patches with well-documented patch signatures in 630.0 nm airglow mapped to a discrete emission altitude. While TEC data are available within the FOVs of both ASIs, here we will focus on optical measurements from only the LYR imager due to daylight contamination masking the upper half of the RSB FOV.

Figure 3.4 presents an overview of this comparative analysis. We have selected the time interval from Figure 3.2g (22:42 UT) when a bright patch was observed in both GPS TEC and LYR airglow data. Nearest TEC values are mapped into each pixel of the LYR FOV (Figure 3.4a) for comparison with the high-resolution measurements of 630.0 nm airglow intensity in Figure 3.4b. Blank regions indicate missing TEC coverage, while areas corresponding to auroral precipitation within the LYR FOV (shaded black) have been discarded

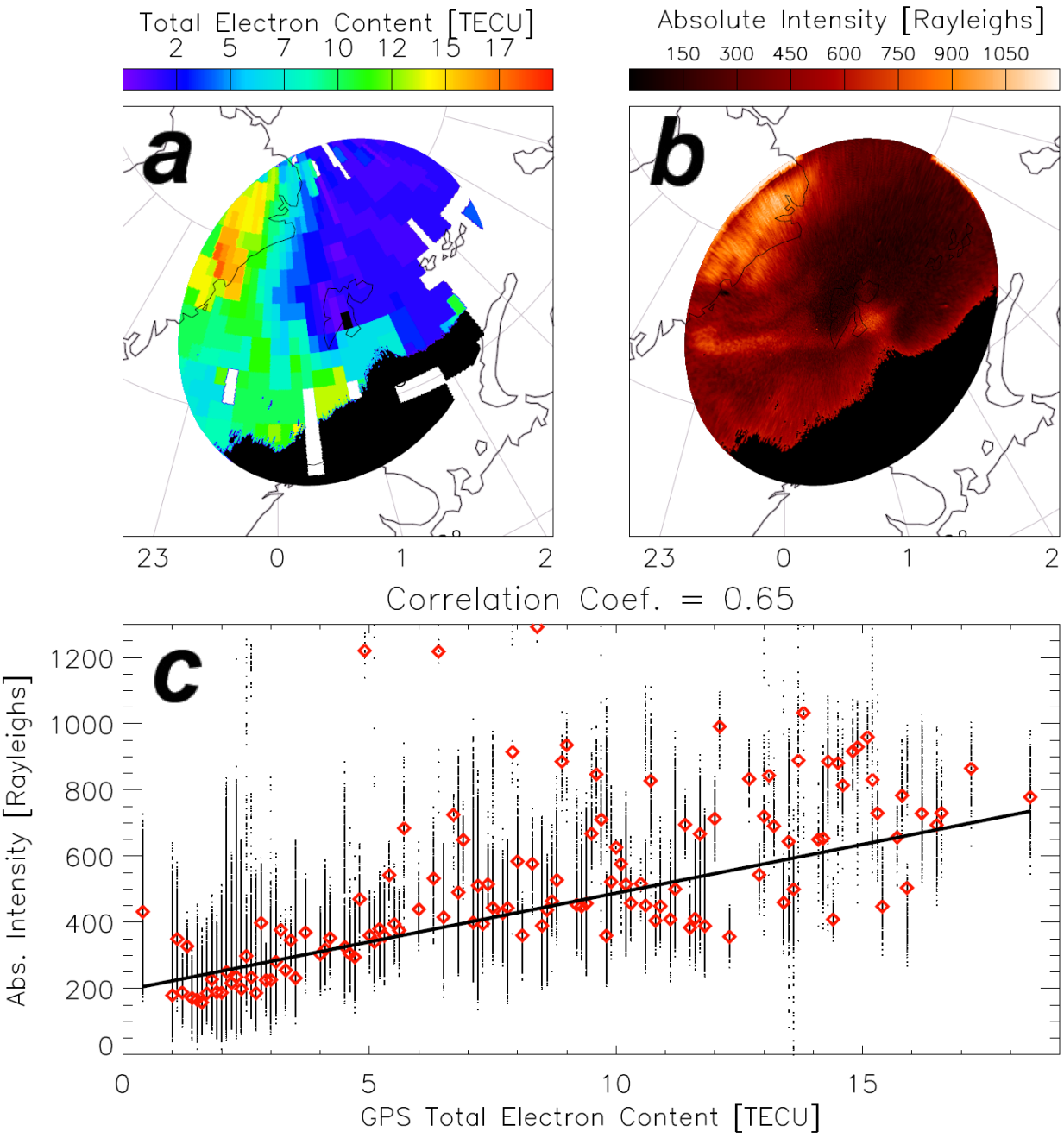

Figure 3.4: (a) GPS TEC for 22:40–22:45 UT mapped into each pixel of LYR FOV and (b) LYR 630.0 nm airglow measurements at 22:42 UT in MLT/MLAT coordinates. Blank spaces in Figure 3.4a indicate missing TEC values while black regions in Figures 3.4a and 3.4b have been filtered to remove auroral airglow emissions. (c) Scatterplot of LYR airglow measurements versus GPS TEC data used to calculate the Pearson correlation coefficient (0.65). Solid line represents the linear fit to all data points (slope = 29.4); red diamonds indicate median values at each TEC bin.

from the analysis. Figure 3.4c presents the LYR airglow intensity as a function of GPS TEC. Red diamonds indicate the median value at each TECU bin while the heavy black line is a linear fit to all of the data. There is a strong positive correlation between the two data sets, with a Pearson correlation coefficient of 0.65 for this interval. This indicates that the optical patch makes the dominant contribution to the height-integrated electron density in the TEC column. While this analysis is limited to one image from a single ASI, it clearly demonstrates the utility of using GPS TEC maps for identifying and tracking polar cap patches and illustrates that the patch-related density perturbation can be the dominant contributor to TEC.

3.3.4 Patch Width and Structuring

Recently, *Hosokawa et al.* [2014] studied the spatial extent of polar cap patches while the RSB and LYR imagers were aligned in a more dawn-dusk geometry during a weakly disturbed period on 12 November 2012. They found the dawn-dusk extent of the patches to be about 1500–2000 km, which overlapped ∼70% of the antisunward plasma flow region. The patches near the dayside convection throat shown in the present study appear much narrower in both the GPS TEC and airglow measurements (500–800 km) and cover only ∼30% of the antisunward flow. This is demonstrated in Figure 3.5, where the SuperDARN global convection contours are overlaid onto the airglow and TEC measurements at 22:42 UT. As suggested by *Hosokawa et al.* [2014], this is likely because the source of the patches (poleward extent of SED plume) was already much more confined in the dawn-dusk direction. In contrast, several patches observed on the nightside within the FOV of the LYR ASI possess a more elongated dawn-dusk appearance. This discrepancy between narrow dayside and wider nightside patches can be explained in terms of the global ionospheric convection pattern. Statistical models of convection [e.g., *Ruohoniemi and Greenwald*, 2005] regularly

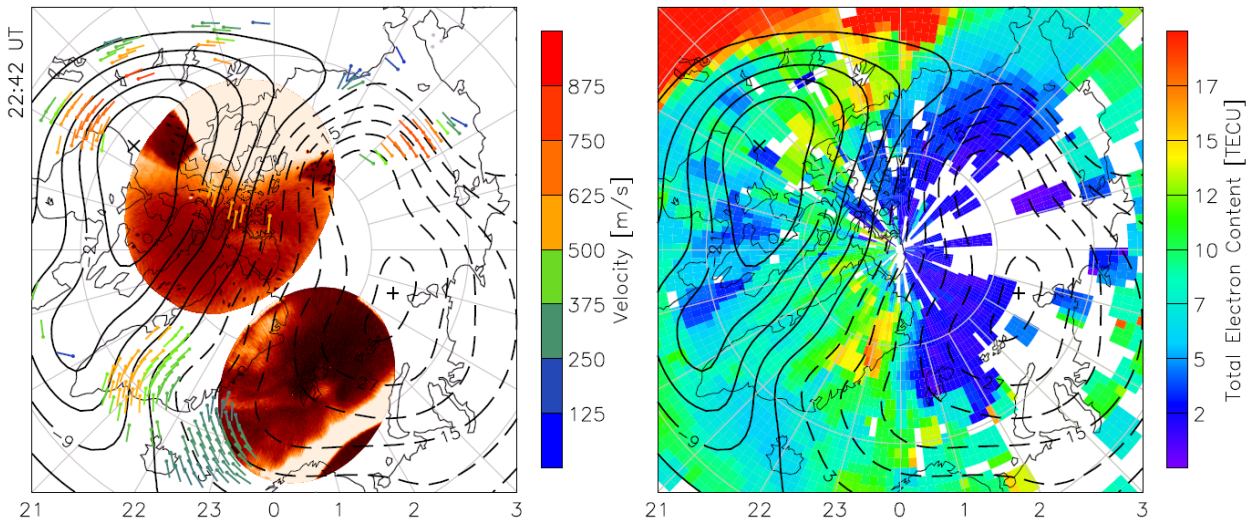

Figure 3.5: Snapshot of (a) RSB/LYR 630.0 nm airglow and (b) GPS TEC observations at 22:42 UT with SuperDARN global convection contours and estimated fitted velocity vectors overlaid in MLT/MLAT coordinates.

predict dense streamlines of plasma drift near the dayside cusp and a broader, more relaxed pattern on the nightside. Such a relaxation of the ionospheric convection would allow narrow patches originating from an SED plume to elongate as they are transported further toward the nightside. Future studies using the multi-instrument, high-resolution technique presented here will be able to test the degree to which the spatial structure of polar cap patches differ under varying geomagnetic conditions and their relation to SED plumes.

Here we characterize the structuring of an individual nightside polar cap patch observed by the LYR ASI (previously shown in Figure 3.2c). The evolution of this patch is tracked from 22:05 to 22:30 UT at 5 min cadence in Figures 3.6a–3.6f with SuperDARN global convection contours and locations of radar velocity vectors again overlaid. Beginning with the image at 22:05 UT (Figure 3.6a) the patch has an almost classical "blob" shape, with a bright center and radially decreasing optical intensity. However, there is also a dimmer "tail" feature extending away from the equatorward, or leading, edge of the patch toward earlier MLT regions and perpendicular to the streamlines of ionospheric convection. The

trailing edge of this tail feature is filled with radar velocity measurements indicating the presence of decameter-scale field-aligned plasma irregularities, while the main body of the patch is nearly devoid of similar irregularity signatures. In the next image at 22:10 UT (Figure 3.6b) the optical intensity of the patch has decreased and a reduction in the amount of radar backscatter is observed. This coincides with a transition in the large-scale convection pattern as the patch encounters a kink in the dawn cell of the convection streamlines.

Moving on to the image at 22:15 UT in Figure 3.6c, the smooth edges of the main body of the patch have become less well defined. There is also a clear spatial separation between the radar backscatter observed along the patch tail and the higher-velocity auroral flows measured at lower latitudes. This gap is well defined in the 630.0 nm airglow as a persistent low-density trough convecting equatorward in advance of the optical patch. Five minutes later at 22:20 UT (Figure 3.6d) this separation between the two irregularity regions is even more apparent, with some lower velocity signatures observed near the leading edge of the tail feature. In Figures 3.6e and 3.6f corresponding to 22:25 and 22:30 UT, the previously smooth main body of the bright optical patch has become increasingly deformed with a great deal of mesoscale structuring observed by the LYR ASI. Narrow finger-like structures are seen extending radially outward from the northern and eastern edges of the patch which are still devoid of any decameter-scale plasma irregularities observable by the SuperDARN radars.

In hindsight, the low-density trough can be traced through the images as it progresses from the northern edge of Svalbard to almost the northern edge of the Scandinavian mainland. This displacement follows the equatorward plasma flow indicated by the convection contours. The tail of the patch defines the poleward edge of the trough and clearly produces radar backscatter that follows the movement of the tail itself. The main body of the patch encounters more distorted convection associated with the rotation of the flow streamlines

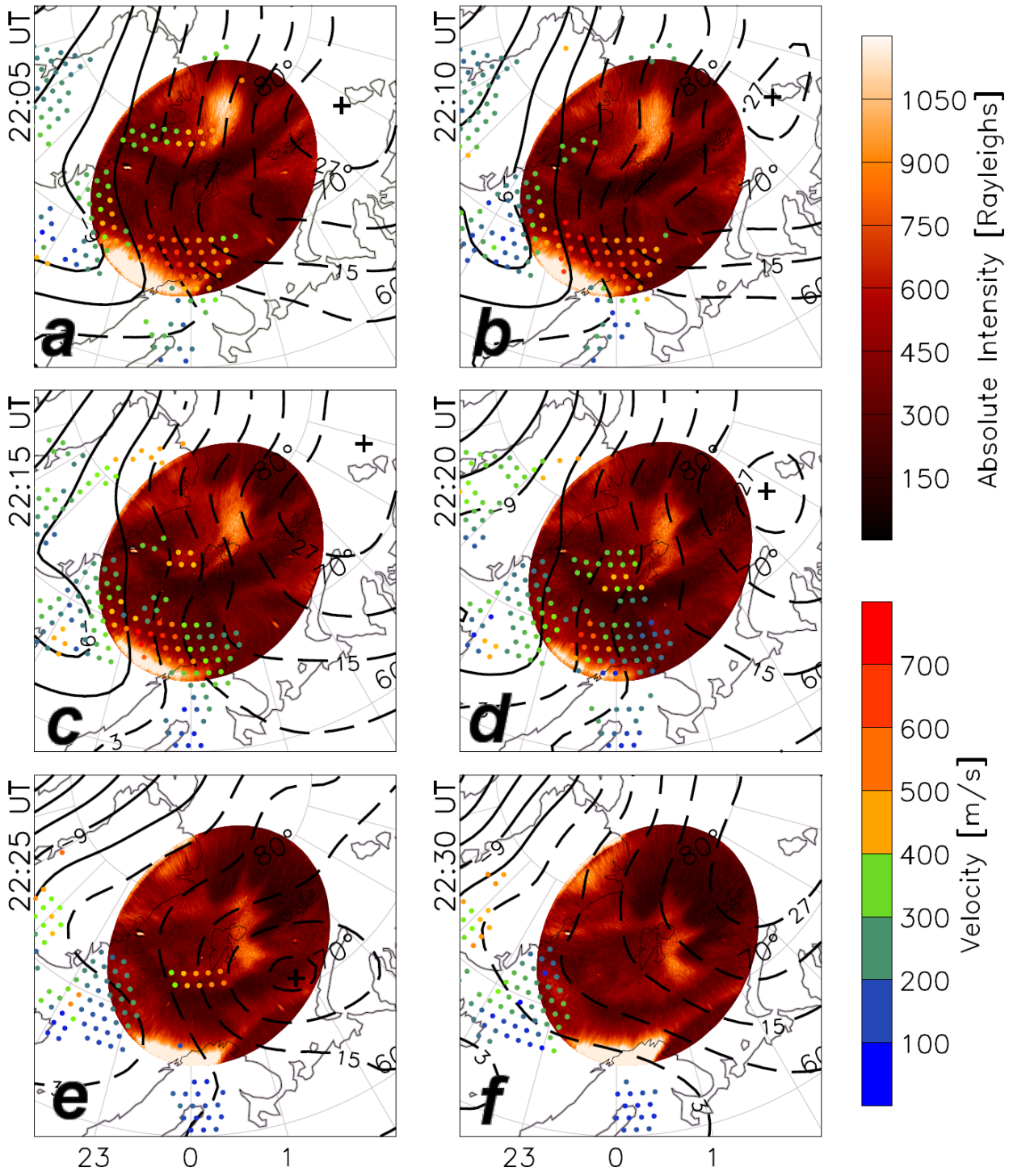

Figure 3.6: (a–f) LYR 630.0 nm airglow images of patch evolution and structuring from 22:05 to 22:30 UT at 5 min intervals with SuperDARN convection contours overlaid in MLT/MLAT coordinates. Locations of radar velocity vectors corresponding to regions of HF backscatter from decameter-scale irregularities are also identified; color scale indicates magnitude of plasma motion along the convection streamlines.

from equatorward to eastward, i.e., toward the dayside. The impact can be viewed in the reshaping of the main body of the patch from a curvature that is oriented westward at higher latitudes to eastward at lower latitudes. Because of their different experiences of convection, the body and the tail of the patch gradually lose the appearance of connectedness. Within the context of this relatively low resolution depiction of the convection, there is no obvious source for the extensive mesoscale structuring that occurs within the main body of the patch. We conclude that patches exiting the polar cap on the nightside are subject to extensive reshaping by convection and quickly lose the spatial imprint of their dayside formation mechanism.

3.4 Discussion and Summary

We have presented observations of polar cap plasma transport during the moderate geomagnetic storm on 22 January 2012 using GPS TEC, 630.0 nm airglow, and SuperDARN measurements. Here, for the first time, we have achieved global high-resolution imaging and tracking by combining these three types of instruments, which opens new possibilities for simultaneously analyzing patch structuring and global transport. An SED plume was observed to form at midlatitudes over North America which provided the source plasma for entry to the polar cap ionosphere. High-density patches originating from this SED plume were then convected across the polar cap at speeds exceeding 500 m/s toward the nightside auroral oval.

As both data sets are often treated as proxies for horizontal F region electron density structure, the correspondence between GPS TEC and 630.0 nm airglow observations of patches has been expected and is now demonstrated with the present paper (Figure 3.4). However, the globally gridded TEC data cannot resolve the fine-scale structure of patches visible at $\sim$2 and $\sim$4 km resolution with the ASIs. Our assumption of the peak emission

altitudes for the airglow images has been confirmed through spatial comparison with the GPS TEC and SuperDARN data. The newly formed patches are also demonstrated to have a clear counterpart in HF radar observations. Decameter-scale plasma irregularities observed by the INV SuperDARN radar appear to be distributed throughout entire patches near the dayside cusp (Figure 3.3a), consistent with previous studies by *Hosokawa et al.* [2009] and *Thomas et al.* [2013]. To within the uncertainties due to the coarser spatial resolution of the radar measurements and variability in HF propagation, the appearance and movement of the backscatter features matches those of the optical patches and can even extend their observation into sunlit conditions.

The relationship between HF radar observations and optical patches on the nightside is more complicated. In the previous section we tracked the evolution and structuring of a bright optical patch as it moved through the FOV of the LYR ASI (Figure 3.6). No HF radar backscatter is observed within the smooth body of the patch or on its edges. However, decameter-scale irregularities appear to be located along the less dense tail feature extending away from the body of the patch with a possible preference for the trailing edge of the tail. This feature was generally oriented perpendicular to the streamlines of plasma convection, suggesting an $\mathbf{E} \times \mathbf{B}$ drift parallel to the positive density gradient on its trailing edge which satisfies the growth condition for field-aligned irregularities via the gradient drift instability. Over the next 30 min the previously smooth body of the patch became increasingly deformed and narrow finger-like structuring is observed on its edges. The patches quickly distort as they exit the polar cap on the nightside and encounter more spatially structured convection. Such finger-like structuring of patches has been reproduced in three-dimensional nonlinear simulations of the gradient drift instability [*Gondarenko and Guzdar*, 2004]. This instability process may be further affected by the presence of a time-varying electric field [*Gondarenko et al.*, 2003], which is clearly indicated by temporal changes in the ionospheric convection

pattern and magnitudes of the radar velocity measurements. Changes in the ionospheric convection driven by variability in the solar wind and magnetosphere-ionosphere coupling processes represent another possible structuring mechanism.

The current study has demonstrated that the shape of patches (i.e., dawn-dusk extent) is clearly different during quiet-moderate and storm time conditions. As mentioned above, this difference is primarily due to the difference in the spatial distribution of the source plasma on the dayside. However, there is another possibility, namely, that the difference in the generation process (how the source plasma is cut or injected near the dayside cusp) may be the cause of the observed difference in the shape. The tendency for wider patches on the nightside can be explained in terms of a relaxation or broadening of the streamlines of ionospheric convection in the nightside polar cap. Need for further comparative study of patch generation during quiet and storm periods is indicated, which could be achieved by combining the type of ground-based measurements described here with in situ rocket or low-altitude spacecraft observations.

Acknowledgments

The authors from Virginia Tech thank the National Science Foundation for support under grants AGS-0946900 and AGS-0838219. E.G.T. also thanks the National Science Foundation for support under grant IIA-1310774 and acknowledges support provided by the Virginia Space Grant Consortium under a graduate research fellowship. The authors from UEC were supported by Grants-in-Aid for Scientific Research (22340143, 23740366, and 20244080) from the Japan Society for the Promotion of Science (JSPS). The optical observation at Resolute Bay was carried out by the joint research program of the Solar-Terrestrial Environment Laboratory (STEL), Nagoya University and was also supported by the NSF cooperative agreement ATM-0608577. *AE* and *Sym-H* indices were obtained from the World

Data Center in Kyoto. The OMNI data were obtained from the GSFC/SPDF OMNIWeb interface at http://omniweb.gsfc.nasa.gov. The TEC data were downloaded through the Madrigal database at Haystack Observatory. The authors acknowledge the use of SuperDARN data. SuperDARN is a collection of radars funded by national scientific funding agencies of Australia, Canada, China, France, Japan, South Africa, United Kingdom, and the United States of America.

Chapter 4

The geomagnetic storm-time response of GPS total electron content in the North American sector

E. G. Thomas[1], J. B. H. Baker[1], J. M. Ruohoniemi[1], A. J. Coster[2], and S.-R. Zhang[2]
Journal of Geophysical Research: Space Physics, Accepted 2016.

[1] Bradley Department of Electrical and Computer Engineering, Virginia Tech, Blacksburg, Virginia, USA.
[2] Haystack Observatory, Massachusetts Institute of Technology, Westford, Massachusetts, USA.

Abstract

Over the last two decades, maps of GPS total electron content (TEC) have improved our understanding of the large perturbations in ionospheric electron density which occur during geomagnetic storms. However, previous regional and global studies of ionospheric storms have performed only a limited separation of storm-time, local time, longitudinal, and seasonal effects. Using 13 years of GPS TEC data, we present a complete statistical characterization of the ionospheric response to geomagnetic storms for midlatitudes in the North American sector where dense ground receiver coverage is available. The rapid onset of a positive phase is observed across much of the dayside and evening ionosphere followed by a longer-lasting negative phase across all latitudes and local times. Our results show clear seasonal variations in the storm-time TEC, such that summer events tend to be dominated by the negative storm response while winter events exhibit a stronger initial positive phase with minimal negative storm effects. We find no discernable difference between spring and fall equinox events with both being equivalent to the average storm-time response across all seasons. We also identify a prominent magnetic declination effect such that stronger dayside positive storm effects are

observed in regions of negative declination (i.e., eastern North America). On the nightside, asymmetries in the TEC response are observed near the auroral oval and midlatitude trough which may be attributed to thermospheric zonal winds pushing plasma upward/downward along field lines of opposite declination.

4.1 Introduction

An ionospheric storm is the specific response of the ionosphere to dynamic features in the solar wind that trigger geomagnetic disturbances throughout the coupled magnetosphere-ionosphere-thermosphere (M-I-T) system. This phenomenon has been studied since the early days of space physics, often in terms of the peak F-layer electron density (*NmF2*) [see Table 1 in *Prölss*, 2008]. The storm-time variation in electron density has traditionally been classified as either a positive (increase) or negative (decrease) effect or phase [*Matsushita*, 1959]. In general, the initial phase tends to be positive across much of the dayside ionosphere and commences soon after storm main phase onset [*Thomas and Venables*, 1966]. This is thought to be the result of storm-time neutral winds and electrodynamical effects which lift the F-layer plasma to higher altitudes where molecular recombination is decreased while solar EUV photoionization persists [*Blanc and Richmond*, 1980; *Foster*, 1993; *Buonsanto*, 1995]. The initial positive phase is often followed by a prolonged negative phase caused by storm-induced thermospheric circulation and composition changes that lead to enhanced recombination of plasma at F-region altitudes [*Prölss*, 1980, 1987]. The progression of this neutral composition disturbance feature to different latitudes and local times is modulated by the background wind field pattern [*Fuller-Rowell et al.*, 1994]. Seasonal variations in positive and negative storm effects are thus related to thermospheric wind morphology. Specifically, equatorward-directed summertime neutral winds tend to reinforce the extension of composition changes toward lower latitudes, while during winter the typically poleward-directed winds will oppose this equatorward expansion [*Fuller-Rowell et al.*, 1996; *Rishbeth*,

1998]. Positive storm effects are thus more prevalent during winter while the negative phase tends to dominate during summer. For additional details, the reader is referred to the excellent ionospheric storm reviews by *Prölss* [1995] and *Buonsanto* [1999].

Total electron content (TEC) is a parameter which has been widely used to characterize the morphology of ionospheric electron density. Whereas *NmF2* is a measure of the F-layer peak density, TEC describes the total number of electrons integrated along a path through the ionosphere. Early studies of storm-time TEC response were obtained by measuring the Faraday rotation of transionospheric radio signals reflected from the moon [*Evans*, 1957; *Taylor*, 1961] and later broadcast by geostationary (GEO) and low Earth orbit (LEO) spacecraft [e.g., *Hibberd and Ross*, 1967; *Klobuchar et al.*, 1971; *Mendillo*, 1971; *Hearn*, 1974; *Lanzerotti et al.*, 1975; *Balan and Rao*, 1990]. More recent statistical studies have used the differential time and phase delay of Global Positioning System (GPS) signals to measure the storm-time TEC response over both regional [*Stankov et al.*, 2010; *Borries et al.*, 2015; *Chen et al.*, 2015] and global scales [*Zhao et al.*, 2007; *Liu et al.*, 2010; *Immel and Mannucci*, 2013]. Most TEC studies have found that positive storm effects tend to occur within the first 24 hours after onset while the subsequent negative phase may persist for up to several days [e.g., *Mendillo*, 2006]. Seasonal variations in thermospheric circulation often produce stronger and longer-lasting positive/negative TEC changes during winter/summer [*Liu et al.*, 2010], although some studies have reported the largest negative storm effects during equinox rather than in summer [*Mendillo and Klobuchar*, 2006; *Stankov et al.*, 2010]. The American longitude sector has been shown to exhibit the largest positive storm response in comparison with other geographic regions [*Zhao et al.*, 2007; *Chen et al.*, 2015] due to the local magnetic dipole tilt and proximity to the South Atlantic Anomaly [*Yizengaw et al.*, 2006].

What has yet to emerge from these previous studies is a clear and intuitive description of TEC response to geomagnetic activity which fully separates storm-time, local time, lon-

gitudinal, and seasonal effects. Many regional TEC studies still cast their results from the perspective of a single site or meridian rotating through different local times as the storm activity evolves. For example, one commonly used technique is to divide storm events by their onset time, thus creating separate TEC patterns for "daytime" and "nighttime" onsets. *Mendillo and Klobuchar* [2006] used an alternative approach by creating average TEC patterns as a function of latitude and local time that describe each day after storm onset, effectively limiting their ability to resolve the storm-time evolution of features to once per 24 h. This issue of separating storm-time and local time effects can be mitigated through use of global GPS TEC maps with simultaneous coverage across all local times. However, such a global approach introduces two additional challenges: 1) data interpolation is necessary over large geographic areas such as oceans where GPS receiver coverage is sparse, and 2) significant variations in storm-time TEC response have been identified for different longitude sectors [*Zhao et al.*, 2007]. Furthermore, several recent studies of quiet-time TEC climatology in the North American and Asian regions have reported localized asymmetries in density as a function of magnetic declination geometry and thermospheric zonal winds [*Zhang et al.*, 2011, 2012, 2013; *Zhao et al.*, 2013; *Chen et al.*, 2015]. The importance of this declination effect under geomagnetically disturbed conditions has yet to be examined in proper detail.

The goal of this paper is to provide a complete statistical characterization of the TEC storm response in the North American sector by fully separating storm-time, local time, and seasonal phenomena. We focus on midlatitudes due to the dense coverage of GPS receivers which have accumulated continuous TEC measurements for more than a solar cycle, significantly reducing the need for spatial/temporal interpolation that is often required when using global maps of GPS TEC. A superposed epoch approach is used to describe the storm-time TEC response using data from all events and as a function of season. Finally,

the existence of a pronounced gradient in magnetic declination across the North American continent allows us to test whether or not the quiet-time zonal wind effect is significant during ionospheric storms.

4.2 Methodology

4.2.1 Storm Identification

In this study, we set a threshold of Sym-H ≤ -50 nT to indicate geomagnetic storm activity. An automated approach was used to identify all times from 2001-2013 when this criterion was satisfied. Consecutive Sym-H values were then grouped together to estimate the time of storm main phase onset (sharp decrease to negative Sym-H values) and minimum Sym-H magnitude for each unique interval. Next, these onset times were manually adjusted where necessary and events with multiple onset signatures were discarded. We have also removed eight "superstorm" events with Sym-H magnitudes exceeding -200 nT from our analysis. The resulting storm list contains a total of 139 events of moderate storm intensity from 2001-2013 and is provided in the online supporting information as Data Set S1 to aid future statistical studies. This text file contains storm main phase onset dates and times, minimum Sym-H values, and the dates and times of minimum Sym-H (i.e., the time of transition between the main phase and recovery phase).

Figure 4.1 presents an overview of the storm events considered in this study. The top panel (Figure 4.1a) shows the Sym-H index for each individual event in a superposed epoch format ranging from one day before to three days after storm main phase onset. The heavy and thinner black lines indicate the median and upper/lower quartiles respectively. As expected, the median Sym-H is approximately zero until just a few hours before onset when there is a brief positive excursion followed by a sharp decrease to negative values.

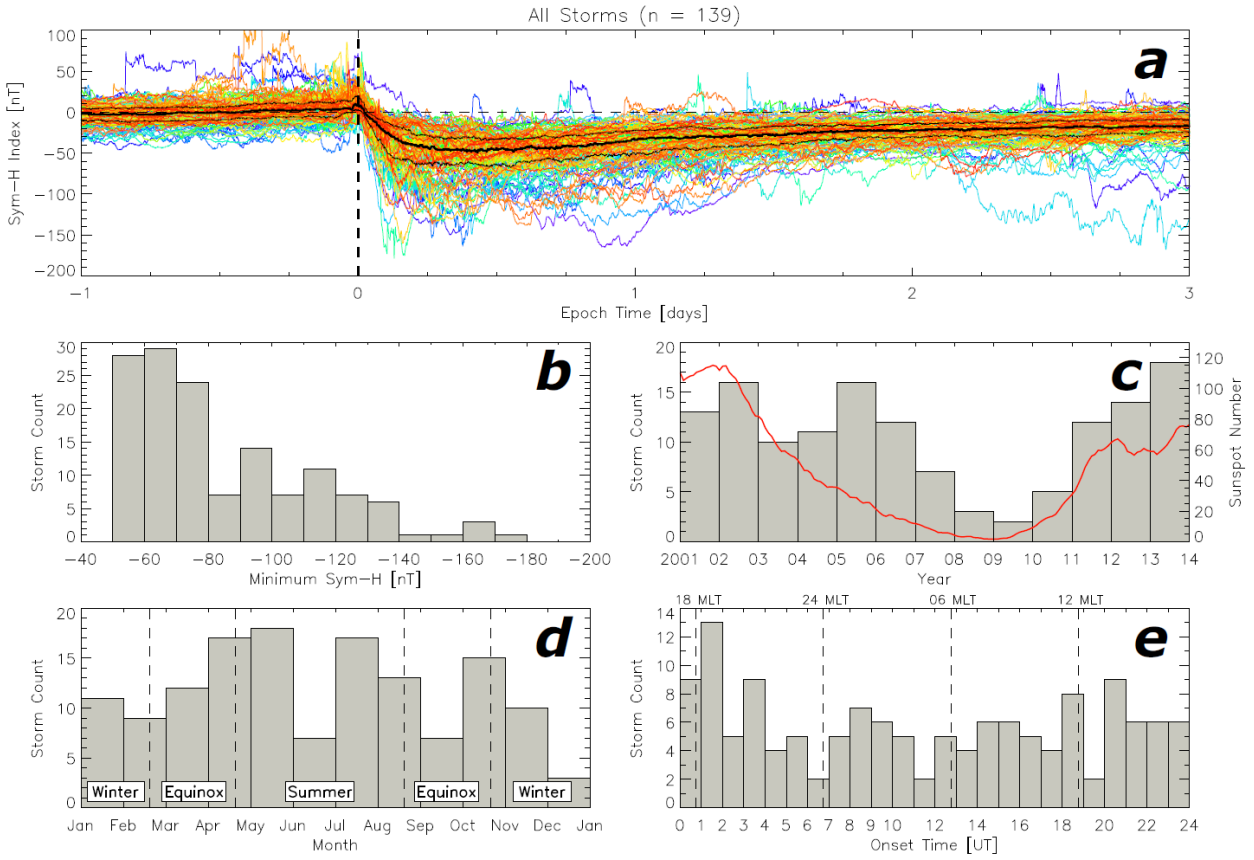

Figure 4.1: (a) Superposed epoch plot of Sym-H index values for 139 storm events from 2001-2013 ordered by time of main phase onset; heavy and thinner black lines indicate the median and upper/lower quartiles. Bottom four panels illustrate geomagnetic storm occurrence sorted by (b) minimum Sym-H magnitude, (c) year, (d) month, and (e) UT onset time. Smoothed monthly sunspot number is overlaid on Figure 4.1c in red to demonstrate the 11-year solar cycle. Approximate seasonal boundaries and MLT location of central North America are marked by vertical dashed lines in Figures 4.1d and 4.1e, respectively.

This sudden positive impulse in Sym-H can often be attributed to a compression of the magnetopause due to an interplanetary shock structure in the solar wind, although it is not present in all geomagnetic storms [*Gonzalez et al.*, 1992]. We next examine the distribution of storm events as a function of Sym-H magnitude (Figure 4.1b). The overall distribution resembles the exponential form identified in previous statistical studies [*Loewe and Prölss*, 1997; *Hutchinson et al.*, 2011] with more than half (81) of the 139 events located in the $-50 \leq$ Sym-H < -80 nT range corresponding to moderate geomagnetic activity.

The remaining panels in Figure 4.1 describe the distribution of events over various timescales. Figure 4.1c shows the occurrence of storms as a function of year and solar cycle, which is indicated here by the smoothed monthly sunspot number overlaid in red. The yearly storm distribution tracks the solar variability quite closely except for the declining phase of Solar Cycle 23 (2004-2007) when high-speed solar wind streams originating from coronal holes become a more frequent driver of geomagnetic activity [*Tsurutani et al.*, 2006]. The seasonal occurrence of storms for the northern hemisphere is shown in Figure 4.1d with vertical lines marking approximate summer, equinox, and winter boundaries. In our event list the greatest number of storms occurred during northern summer (55), followed by equinox (45) and winter (39). Finally, in Figure 4.1e we present the distribution of storm onsets as a function of Universal Time (UT). A fairly uniform distribution of onsets with UT is crucial to our analysis for obtaining sufficient coverage in local time.

4.2.2 GPS Total Electron Content

Global maps of GPS TEC binned into $1^\circ \times 1^\circ$ cells at 5 min cadence were obtained from the online Madrigal database at MIT Haystack Observatory (http://madrigal.haystack.mit.edu/). These maps are produced using the MIT Automated Processing of GPS (MAPGPS) algorithm [*Rideout and Coster*, 2006] that currently ingests measurements from over 5,000 GPS receivers worldwide. One TEC unit (TECU) is given as $1{\times}10^{16}$ el/m^2 and represents the total number of electrons contained in a column extending through the ionosphere with a cross-sectional area of 1 m^2. This means that a simple vertical redistribution of plasma has no direct impact on the TEC parameter. Because GPS spacecraft orbit the Earth at an altitude of $\sim$20,200 km ($3.2R_E$) this column measurement also includes a contribution from the overlying plasmasphere as a function of latitude, local time, storm activity, and solar cycle. *Yizengaw et al.* [2008a] found the average plasmaspheric contribution at midlatitudes

to be ∼10% on the dayside and ∼30% on the nightside. Therefore one must be careful when attributing variations in GPS TEC solely to ionospheric phenomena.

In this study, the original 5 min GPS TEC values over North America have been re-binned onto a new 2° × 4° latitude/longitude grid spanning 29.5°-53.5°N and 68°-128°W as 30 min average values. The resulting data set consists of 48 TEC maps per day for the years 2001-2013. An example of this procedure can be seen in Figure 4.2a where the outline of the new grid is overlaid onto the original Madrigal TEC data during a storm-time SED plume interval from 22:15-22:20 UT on 26 Sep 2011 [*Thomas et al.*, 2013]. Figure 4.2b shows the re-gridded TEC values from the corresponding 30 min interval for comparison. Blank regions over the oceans and central Canada in Figure 4.2a indicate missing TEC data; empty bins in Figure 4.2b are missing data from the entire 30 min averaging interval. While there is a decrease in spatial and temporal resolution, large-scale morphological features such as the SED plume [*Foster*, 1993] and density trough [*Rodger*, 2008] are still captured in the re-gridded data.

Instantaneous (TEC) and 27-day median (TECq) values are then recorded from the re-gridded data set for each 30 min bin in the interval ranging from 1 day before to 3 days after each of the 139 storm onset times identified from the Sym-H index. Note that the TECq values are obtained by taking a 27-day median centered on the UT interval of each 30 min bin. Similar to *Zhao et al.* [2007], these TEC and TECq values are then used to calculate the storm-time relative change in total electron content (RTEC) as

$$RTEC = \frac{TEC - TECq}{TECq} \tag{4.1}$$

Thus positive RTEC values indicate a storm-time increase in TEC relative to the 27-day median while negative values indicate a relative decrease. Here we use a relative change

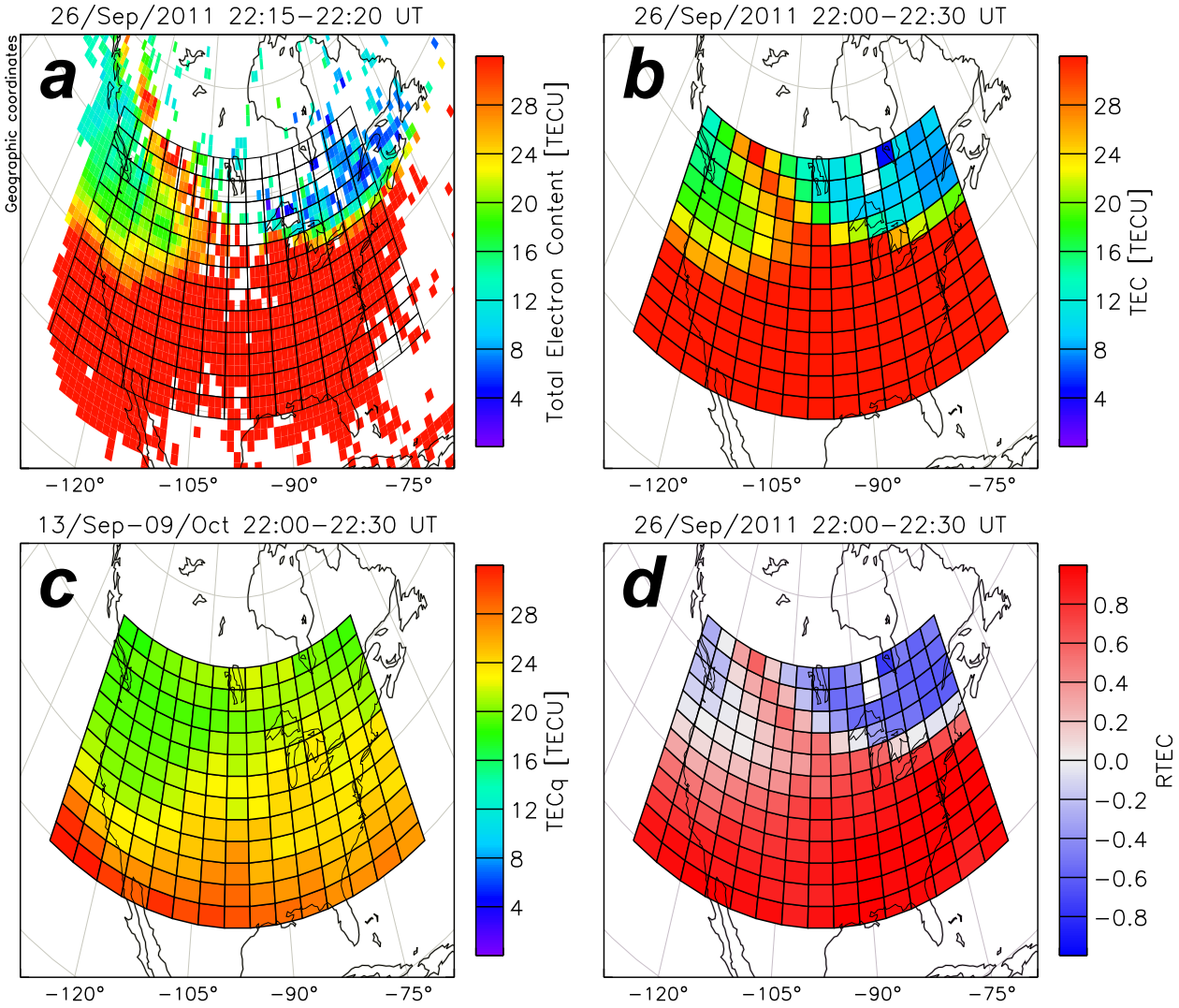

Figure 4.2: (a) Original 5 min GPS TEC values at $1° \times 1°$ resolution obtained from Madrigal for 22:15-22:20 UT on 26 Sep 2011, with outline of new $2° \times 4°$ geographic latitude/longitude grid overlaid. (b) Re-binned TEC values averaged over comparable 30 min interval from 22:00-22:30 UT on 26 Sep 2011. (c) 27-day median (TECq) values for same 22:00-22:30 UT interval. (d) Relative storm-time change (RTEC) values for 22:00-22:30 UT on 26 Sep 2011; positive (red) values indicate an increase in TEC relative to the 27-day median (TECq) while negative (blue) values indicate a relative decrease. Note that GPS TEC data in Figure 2a correspond to one of six TEC maps used to calculate the 30 min average shown in Figure 2b.

(RTEC) rather than an absolute storm-time difference because of the variation in background TEC with diurnal, seasonal, and solar cycle effects. For example, a factor of 2 increase in TEC from 30 to 60 TECU associated with a storm during solar cycle maximum would mask the same relative increase from 10 to 20 TECU during a solar cycle minimum event.

Returning to the example in Figure 4.2, the bottom left panel (Figure 4.2c) shows the corresponding median (TECq) values for the 22:00-22:30 UT interval from a 27-day window centered on this sample event. TECq values are generally observed to decrease with increasing latitude in accordance with solar EUV photoionization being the dominant dayside production mechanism, as is the case for 22:00-22:30 UT when North America is in the post-noon sector. Comparing Figures 4.2b and 4.2c, the storm-time TEC values represent a clear departure from the 27-day median TECq values. This is explicitly demonstrated by the corresponding RTEC values calculated using equation (4.1) and shown in Figure 4.2d. The bright red RTEC values (> 0.8) over much of the lower half of North America correspond to almost a factor of 2 increase in TEC relative to the 27-day median in Figure 4.2c, while the low-density trough at higher latitudes corresponds to a $\sim$50% decrease in TEC.

Using this approach storm-time TEC variations are next organized by magnetic latitude (MLAT) and magnetic local time (MLT) coordinates for each event. Specifically, RTEC values are converted from geographic to Altitude-Adjusted Corrected Geomagnetic (AACGM) coordinates [*Baker and Wing*, 1989] using the refined approach developed by *Shepherd* [2014]. Finally, median values of RTEC within each MLAT/MLT bin are calculated using data from all (or a subset) of storm events and are presented as a function of storm epoch time. Thus we obtain a complete separation between storm-time and local time features as called for in the Introduction.

4.3 Results

In this section we present results from the superposed epoch study of GPS TEC storm response described above. First, the general case is considered using RTEC values from all storm events. Next, we evaluate seasonal variations by separating events into summer, equinox, and winter categories. Finally, we examine TEC storm response in terms of the asymmetry in magnetic field declination over North America.

4.3.1 Storm Response Overview

Figure 4.3 shows an overview of the general TEC storm response using data from all 139 events as a series of MLAT/MLT maps of median RTEC at 3 hr intervals following main phase onset. The same color scale from the example in Figure Figure 4.2d is used and bins containing fewer than 3 data points are shaded black. At the zero epoch time (top left panel) RTEC values are only very weakly positive (< 0.10) across all latitudes and local times. In the initial 6 hours following storm onset, a clear positive response is observed at all latitudes over much of the dayside and evening ionosphere with peak RTEC values located in the 12-18 MLT sector. A strongly positive RTEC feature is also found at high latitudes on the nightside (21-06) which evolves in both magnitude and spatial extent before fully disappearing 27 hours after onset. A weaker positive response located at subauroral latitudes on the nightside is the last remaining feature of the initial large-scale TEC enhancement.

The first signatures of negative storm effects are observed separately in the dusk and dawn regions within ∼3-6 hours after onset. Near 18 MLT, a narrow band of decreased TEC is observed first at high latitudes just westward of the nightside enhancement which then gradually expands equatorward down to about 55° MLAT. In the dawn sector, a region of negative RTEC can be seen developing just equatorward of the auroral zone before progress-

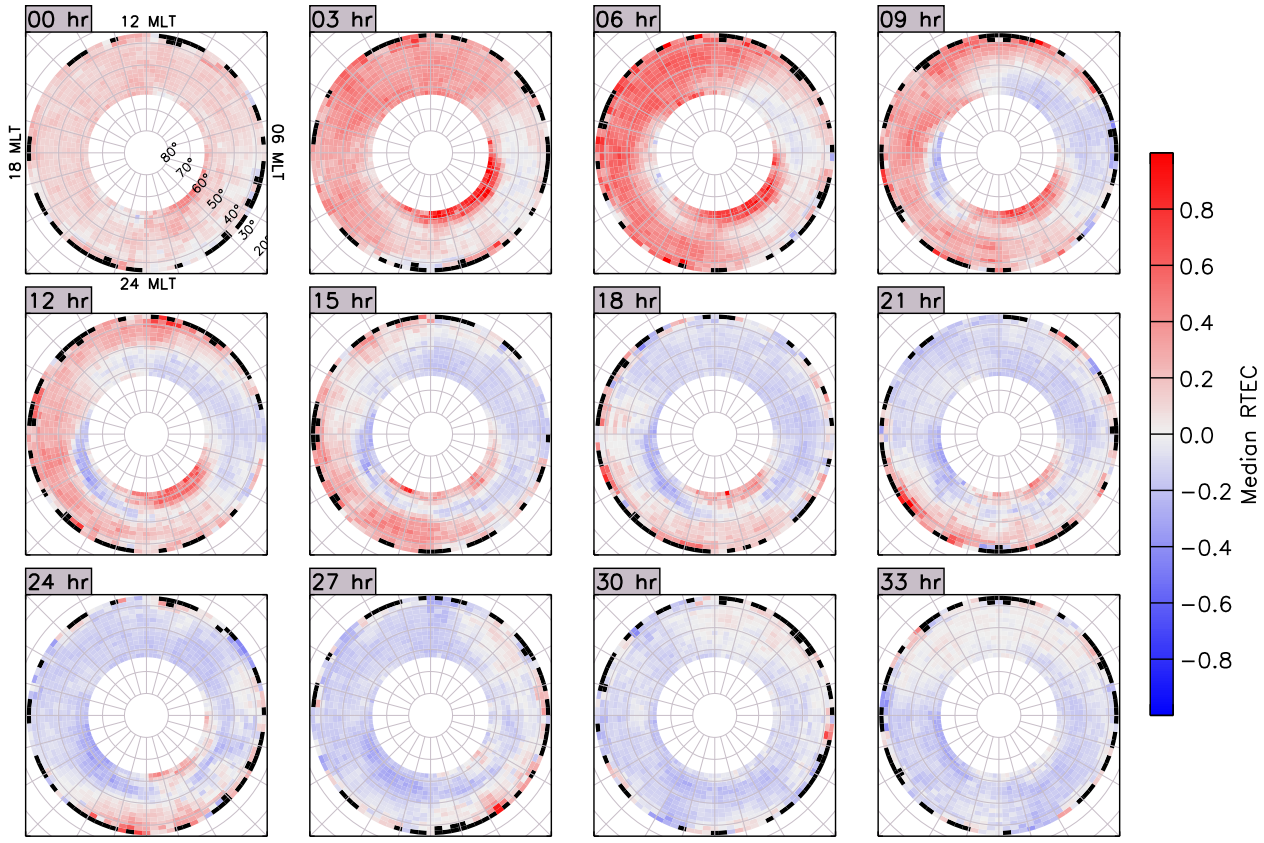

Figure 4.3: Maps of median RTEC at 3 hr intervals after storm onset in magnetic latitude (MLAT) and magnetic local time (MLT) coordinates using data from all 139 events. Positive (red) values indicate an increase in TEC relative to the 27-day median (TECq) while negative (blue) values indicate a relative decrease; bins shaded black contain fewer than 3 data points.

ing toward later local times on the dayside ionosphere. By the +9 hr epoch this negative storm effect reaches the 12 MLT meridian and begins to define the equatorward edge of a positive RTEC plume. Simultaneously, the nightside trough-like feature also expands in local time across 17 to 24 MLT as it defines the poleward edge of the plume. After 21-24 hours the negative storm effects originating in the dawn sector are the dominant TEC feature as the ionosphere and thermosphere slowly recover to their pre-storm state. The reader is referred to Movie S1 in the online supplementary information for the storm-time evolution of median RTEC values from 1 day before to 2 days after storm onset in the same MLAT/MLT format as Figure 4.3.

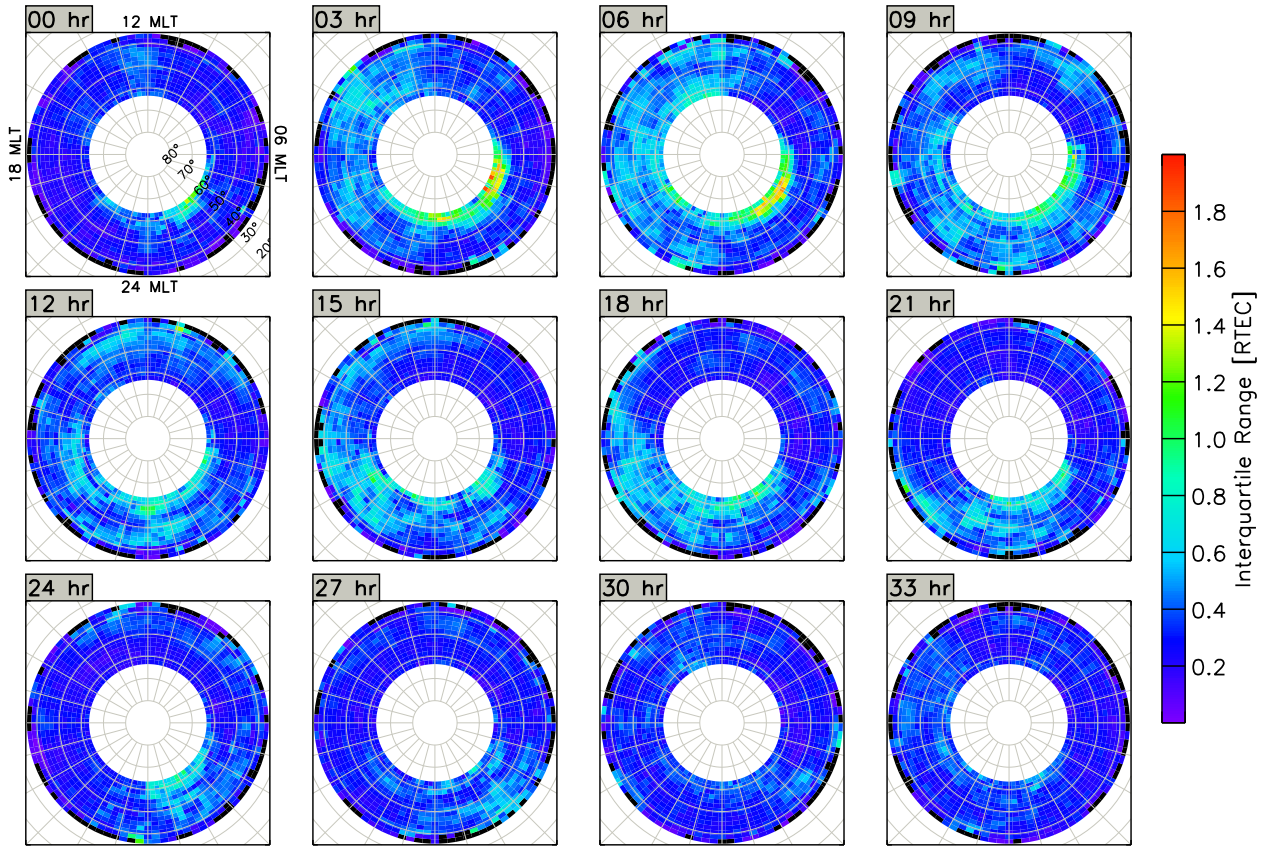

Figure 4.4: Interquartile range (IQR) of RTEC values using data from all 139 storm events, in the same MLAT/MLT format as Figure 4.3.

To assess the quality of the superposed epoch results, we examine the variability of the RTEC data in terms of their interquartile range (IQR). Figure 4.4 shows the IQR of each MLAT/MLT bin at 3 hr intervals following main phase onset in the same manner as Figure 4.3. For the entire duration of the ionospheric storm the greatest variability is located within the nightside positive enhancement region, with IQR values exceeding 1.6 RTEC during the first 6 hrs following onset. Regions of positive RTEC on the dayside in Figure 4.3 also tend to exhibit greater variability than negative RTEC regions, although IQR values typically remain below about 0.8 RTEC. This is to be expected given the nature of the RTEC parameter: negative values may not exceed -1.0 in magnitude while positive values have no inherent upper limit. We remind the reader that while the data representation in

Figures 4.3 and 4.4 may give the appearance of truly global data coverage, the superposed epoch results are valid only for the North American sector.

4.3.2 Day/Night and Dusk/Dawn Asymmetries

We next consider RTEC values along selected MLT meridians as a function of storm epoch time to more closely investigate the temporal evolution of the TEC response. Figure 4.5a shows median RTEC along the noon (11-13 MLT) meridian versus magnetic latitude in a keogram format, while Figure 4.5b shows the distribution of RTEC values from all latitude/longitude bins within that 2 hr MLT span. Here we see that the positive storm response occurs almost simultaneously across all latitudes. This is followed by a negative phase beginning $\sim$7 hours after onset which progresses from higher latitudes down to 50° where it stalls or even reverses for 6 hours until resuming its equatorward progression. From the distribution in Figure 4.5b, peak RTEC values are observed approximately 5 hours after onset and can be as large as a factor of 2 increase relative to background conditions. The persistence of positive RTEC values below 50° is also reflected in the double-peaked structure of the RTEC distribution in Figure 4.5b. The magnitude of the negative storm response from 15-27 h remains nearly constant at a level corresponding to a $\sim$20% decrease in TEC. Within 30 hours the RTEC data have largely returned to their pre-storm state but with a slightly greater variability.

Figures 4.5c and 4.5d describe the RTEC response along the midnight (23-01 MLT) meridian in a similar fashion. The high-latitude enhancement previously identified in Figure 4.3 extends down to about 57° and persists for a full 24 hours following storm onset. In comparison to the noon-time response, the midnight positive effect at subauroral latitudes is much less intense and more variable and persists about 10 hours longer before the complete

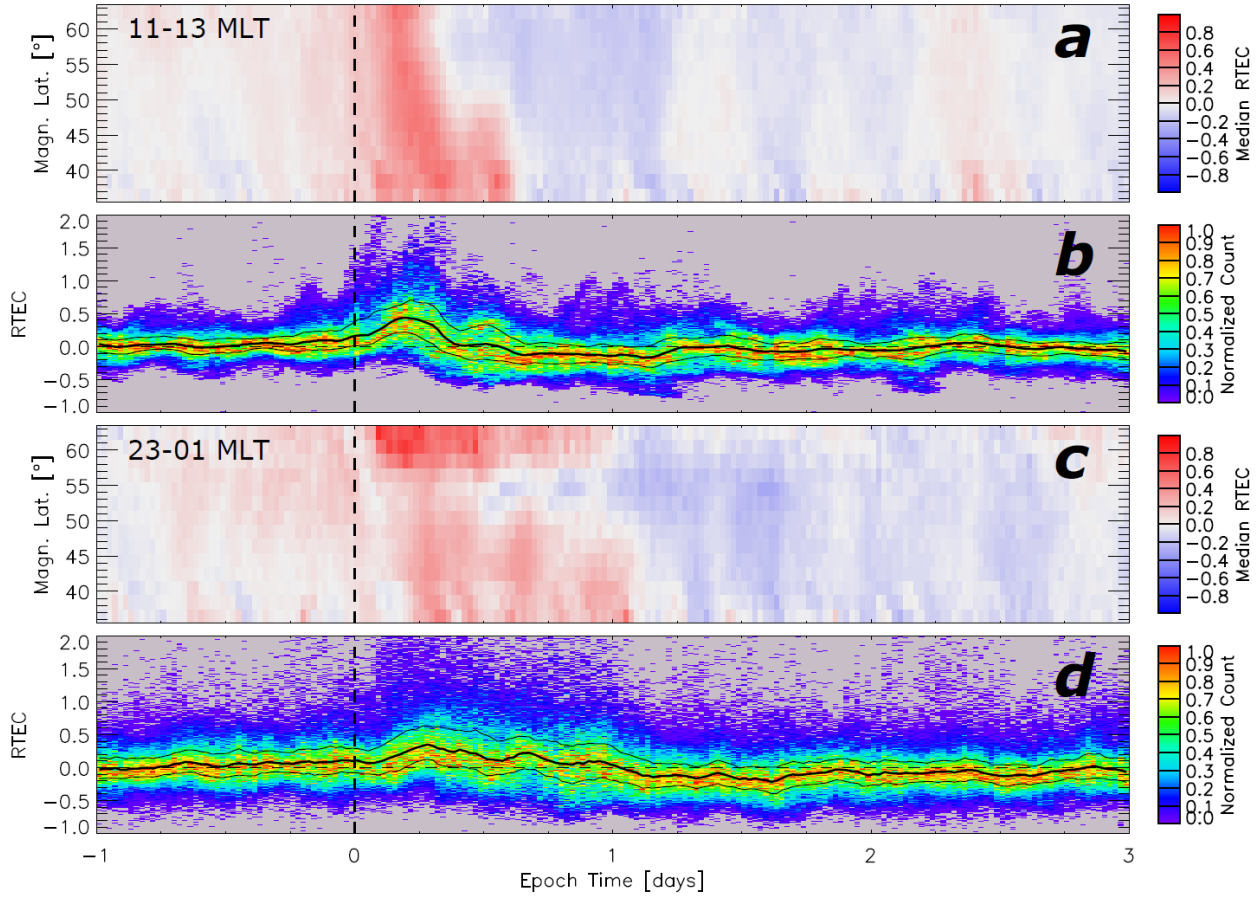

Figure 4.5: Overview of RTEC values from all storm events along the 11-13 MLT (noon) and 23-01 MLT (midnight) meridians. (a,c) Keogram of median RTEC values along the noon/midnight meridian versus magnetic latitude. (b,d) Distribution of RTEC values from all storms and latitude bins along the noon/midnight meridian, normalized by the maximum count at each 30 min time step; heavy and thinner black lines indicate the median and upper/lower quartiles, respectively. Empty bins have been shaded gray and vertical dashed line indicates storm main phase onset.

transition to negative storm effects across all latitudes. Twelve hours before this long-lasting negative phase begins, a latitudinally narrow region of decreased TEC can be observed just equatorward of the auroral enhancement. The presence of this negative storm feature simultaneously with the high-latitude and subauroral TEC enhancements likely contributes to the large spread in the distribution of RTEC values during the first storm day in Figure 4.5d.

We perform a similar analysis in Figure 4.6 for the dusk (17-19 MLT) and dawn (05-07

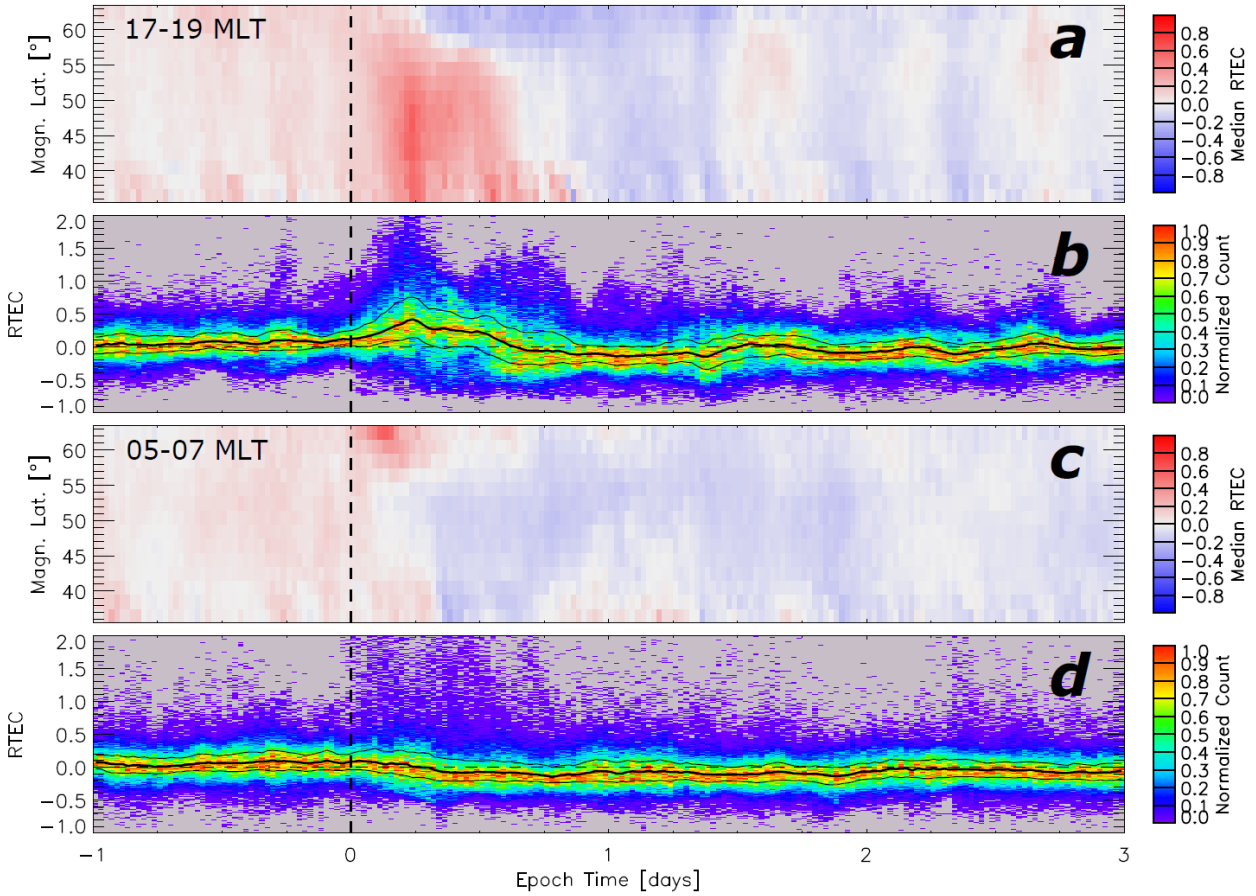

Figure 4.6: Overview of RTEC values from all storm events along the 17-19 MLT (dusk) and 05-07 MLT (dawn) meridians. (a,c) Keogram of median RTEC values along the dusk/dawn meridian versus magnetic latitude. (b,d) Distribution of RTEC values from all storms and latitude bins along the dusk/dawn meridian, normalized by the maximum count at each 30 min time step; heavy and thinner black lines indicate the median and upper/lower quartiles, respectively. Empty bins have been shaded gray and vertical dashed line indicates storm main phase onset.

MLT) meridians. Starting with the dusk sector in the upper two panels, we see a gradual increase in RTEC across all latitudes which maximizes 6 h after onset. Less than an hour later the trough-like feature can be seen expanding equatorward for the next 8 h before becoming indistinguishable from the larger negative storm phase at lower latitudes. The TEC response across all latitudes is largely negative until 36 h after the initial storm onset. Moving to the dawn sector in Figures 4.6c and 4.6dc, the positive phase of the storm is almost absent except

for a short-lived high-latitude feature. The strongly positive RTEC values above 60°N which last until 18 h after storm onset are related to the sunward/dawnward extent of the midnight feature seen in Figure 4.5c. After this high-latitude enhancement disappears the distribution of RTEC values in Figure 4.6d becomes much more symmetric about the median.

To summarize, positive storm effects are observed across much of the dayside and evening ionosphere (09-24 MLT) for the North American sector during the initial 6 h after storm onset, maximizing within the plume feature near 15 MLT. A large positive enhancement is also found at high latitudes on the nightside centered at around 03 MLT. After 6 h negative storm effects are observed simultaneously in the dusk and dawn regions corresponding to a trough-like feature and broader TEC depletion, respectively. While the trough-like feature is a latitudinally-narrow TEC depletion from 17-24 MLT with an equatorward boundary of only about 55° MLAT, the post-midnight negative storm effect gradually progresses across all latitudes and local times over the next 24 h.

4.3.3 Seasonal Asymmetries

In this section we present seasonal variations observed in the storm-time GPS TEC response over North America. The 139 storms are now subdivided into summer, equinox, and winter categories according to their onset date and time (Figure 4.1d). As a reminder, the greatest number of events occur during northern summer (55) followed by equinox (45) and winter (39). We have examined the distribution of events for each season by their minimum Sym-H magnitude (e.g., Figure 4.1b) and UT onset time (Figure 4.1e) and found them to be consistent with the results for all events shown in Figure 4.1. These distributions are available for reference in the online supplementary material as Figure S1. With confirmation that the statistics will not be affected by either outliers in storm magnitude or insufficient UT

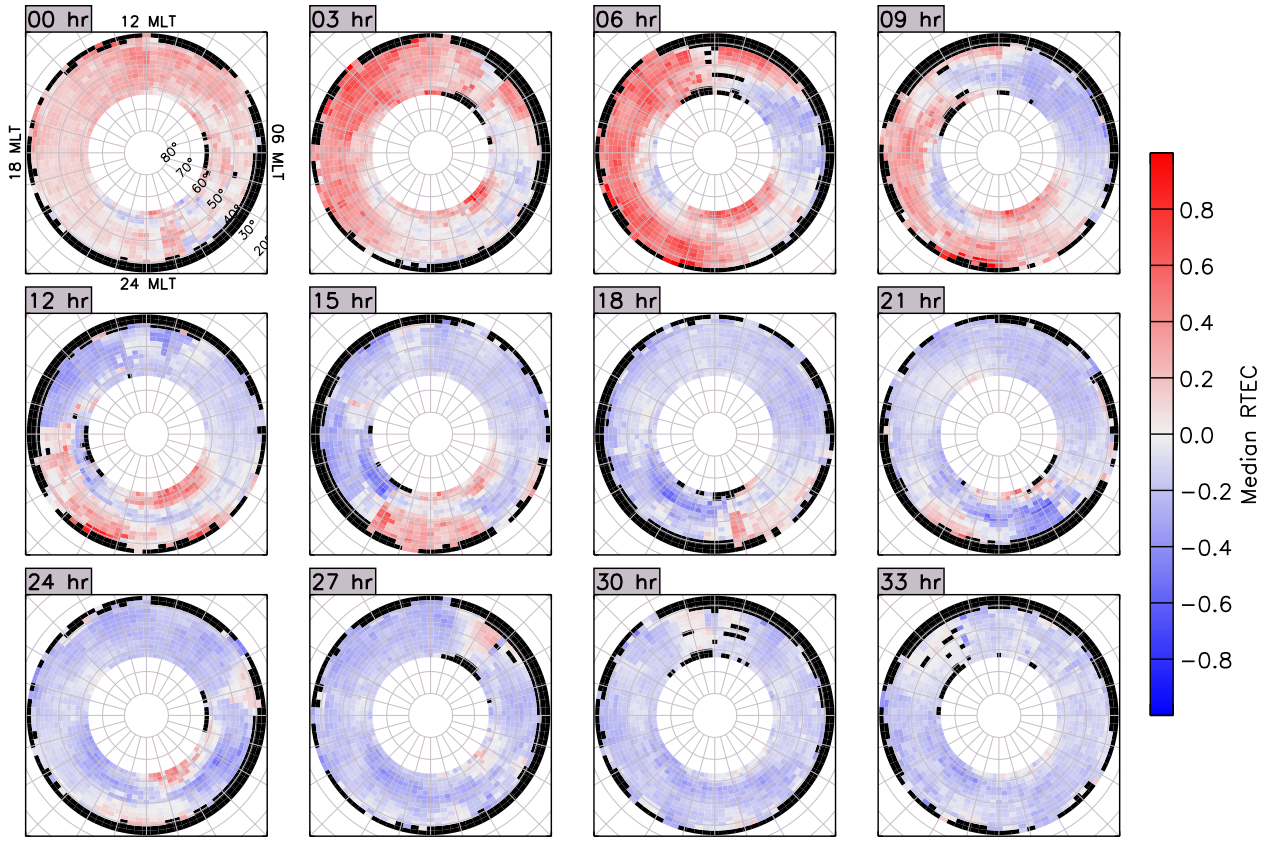

Figure 4.7: Maps of median RTEC using data from 55 summer events, in the same MLAT/MLT format as Figure 4.3; bins shaded black contain fewer than 3 data points.

coverage, we apply the RTEC analysis separately for summer, equinox, and winter seasons.

Figure 4.7 shows an overview of the median RTEC response for the 55 summer events at 3 hr intervals in the same MLAT/MLT format as Figure 4.3. During the first 6 hours after storm onset we again observe an initial positive RTEC enhancement across much of the dayside ionosphere and at high latitudes near midnight. Similarly, regions of negative RTEC are also observed at high latitudes near dusk (trough-like depletion) and at subauroral latitudes in the post-midnight sector. Here we begin to see a marked departure from the general case (Figure 4.3) as the negative storm feature originating near dawn advances across the dayside ionosphere much more rapidly. Within 12 hours the dayside positive enhancement has almost entirely disappeared with only faint signatures of a possible plume-

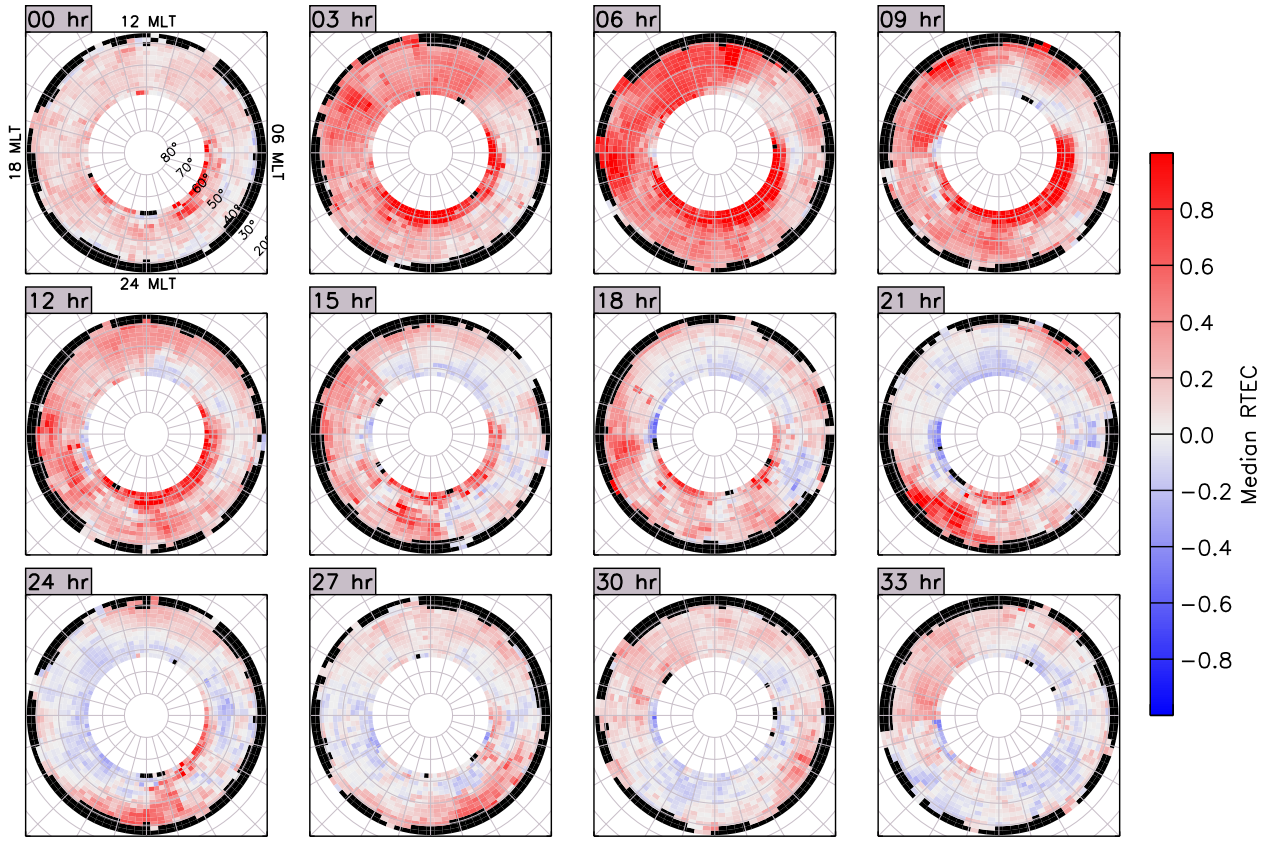

Figure 4.8: Maps of median RTEC using data from 39 winter events, in the same MLAT/MLT format as Figure 4.3; bins shaded black contain fewer than 3 data points.

like enhancement remaining near 18 MLT. The magnitude of the relative TEC decrease during summer is also much larger than for the general case using data from all events. This negative storm phase persists across all latitudes and local times for another 24 hours beyond the interval shown in Figure 4.7 and can be considered the dominant characteristic of summer TEC storm response.

Next we consider results for storm onsets occurring in winter. Similar to the previous figures, Figure 4.8 shows the median RTEC response for 39 winter events. Again many of the same positive RTEC features are observed early after storm onset such as the broad dayside and high-latitude nightside enhancements. In contrast to the summer results however, a much stronger and longer-lasting postive phase is observed across nearly all latitudes and

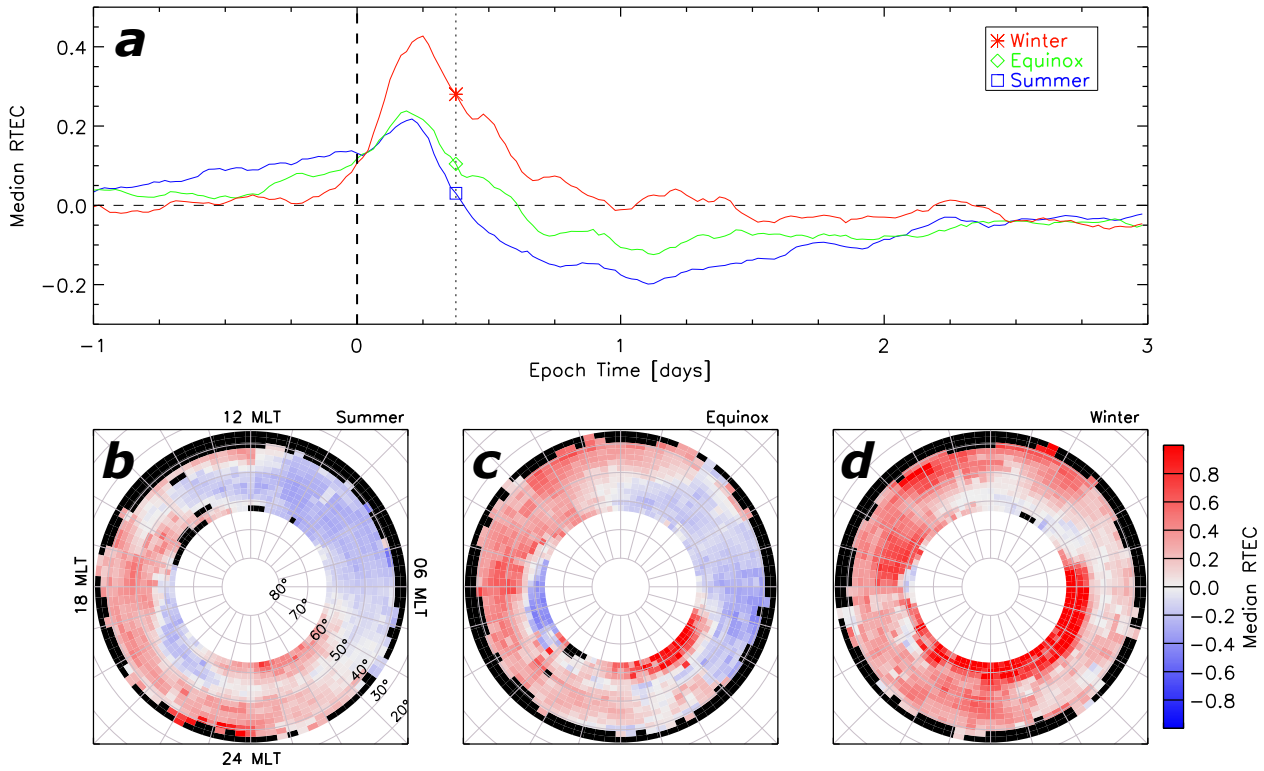

Figure 4.9: Summary of seasonal RTEC variability as a function of storm epoch time. (a) Time series of median RTEC values from all MLAT/MLT bins for summer (blue), equinox (green), and winter (red) events. Bottom row: snapshots of median RTEC in MLAT/MLT format 9 hours after storm onset for (b) summer, (c) equinox, and (d) winter seasons.

local times. Negative storm effects are not observed until 9-12 h after onset and are primarily restricted to high latitudes ($> 55°$) for the initial 18 hours. Afterwards, relatively weaker TEC depletions are seen progressing toward the midnight sector. The high-latitude TEC depletion appearing ∼12 hrs after onset near dusk is much narrower in latitude and local time and does not penetrate as far equatorward as was seen for the general or summer case. The results in Figure 4.8 clearly demonstrate the dominance of positive storm effects during winter compared to summer (Figure 4.7).

Interestingly, repeating the same analysis for equinox events produces nearly identical results to the general TEC response found using data from all storms (Figure 4.3), regardless of spring or fall categorization. Seasonal variations in the summer, equinox, and winter

storm-time TEC response are summarized in Figure 4.9: the top panel (Figure 4.9a) shows median RTEC across all magnetic latitudes and local times, while the bottom panels (Figures 4.9b–4.9d) are representative snapshots for each seasonal response at 9 hrs after storm onset. Both positive and negative storm effects are observed in all seasons, however, negative features are much more pronounced during summer while positive effects dominate the winter storm response. The transition to negative storm phase also occurs earliest in summer (10 h) compared to equinox (15 h) and winter (24-36 h). The equinox storm response can be considered an intermediate case between the negative summer and positive winter extrema described above.

4.3.4 Magnetic Declination Asymmetries

We now consider the relationship between magnetic field line geometry and the storm-time TEC response. In particular, we focus on the fact that the 90°W meridian divides the North American sector into two zones of positive and negative declination. Figure 4.10a shows a color-coded map of magnetic declination in this region at 300 km altitude obtained from the International Geomagnetic Reference Field (IGRF) model [*Finlay et al.*, 2010]. The narrow white band running from northern Canada to the Gulf of Mexico indicates where the transition from negative (blue) to positive (red) declination goes to zero, i.e., there is no east-west tilt of the magnetic field line. This geometry is demonstrated in Figure 4.10b, where the east-west orientation of field lines centered about the declination reversal boundary is shown as a function of geographic longitude and altitude for 41°N. Thus we see how an eastward zonal wind might push plasma downwards (upwards) along field lines in the positive (negative) declination region to altitudes of increased (decreased) recombination, leading to a decrease (increase) in the F-layer density and electron content. Similarly, a westward zonal wind would have the opposite effect on density in each declination region.

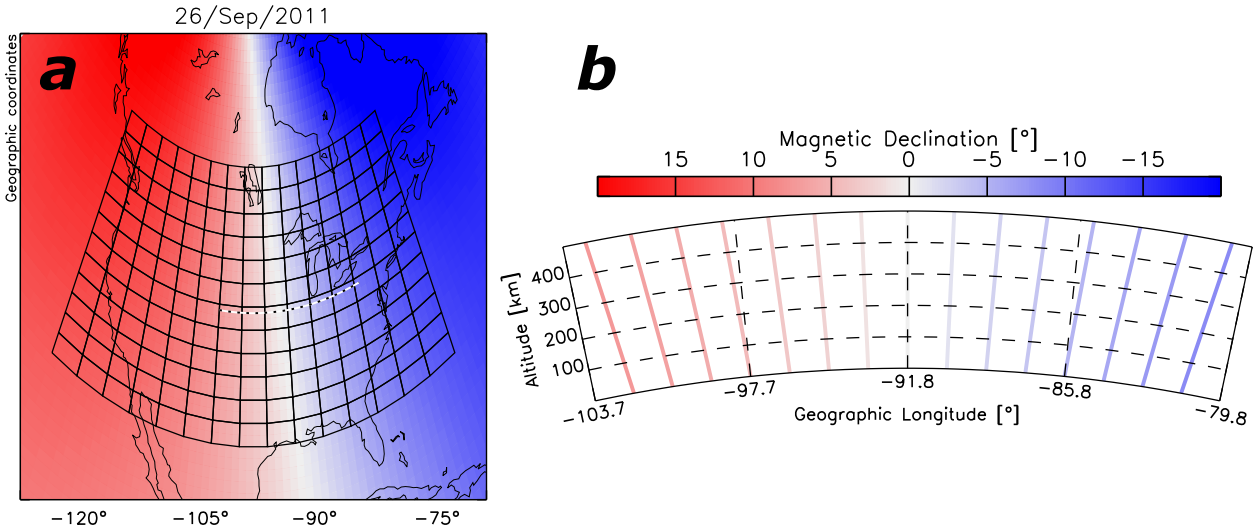

Figure 4.10: (a) Geomagnetic field declination in the North American sector for 26 Sep 2011 obtained from the IGRF model [*Finlay et al.*, 2010]. (b) Schematic illustrating magnetic field line geometry as a function of geographic longitude and altitude centered on the declination reversal boundary at 41°N geographic latitude, marked by the dotted line in Figure 4.10a.

While this longitudinal dependence has been examined in terms of TEC climatology during geomagnetically quiet intervals [e.g., *Zhang et al.*, 2013] it has yet to be tested statistically under storm-time conditions.

Rather than sorting results according to season, we now organize them by the sign of magnetic declination in each geographic latitude/longitude bin as obtained from the IGRF model (e.g., Figure 4.10a). In this manner we calculate results separately for regions of negative and positive declination, corresponding to eastern and western North America respectively. The maximum change in declination in the region of interest over North America was 2.9° between 2001 and 2013 with an average change in declination of about 1.35°. Therefore the bins closest to the white 0° declination line in Figure 9a may contribute values to either the $RTEC_{East}$ or $RTEC_{West}$ data sets depending on the date of each particular event. Figure 4.11 shows median RTEC values during the initial 12 hours following storm onset for negative ($RTEC_{East}$, top row) and positive ($RTEC_{West}$, middle row) declination regions in

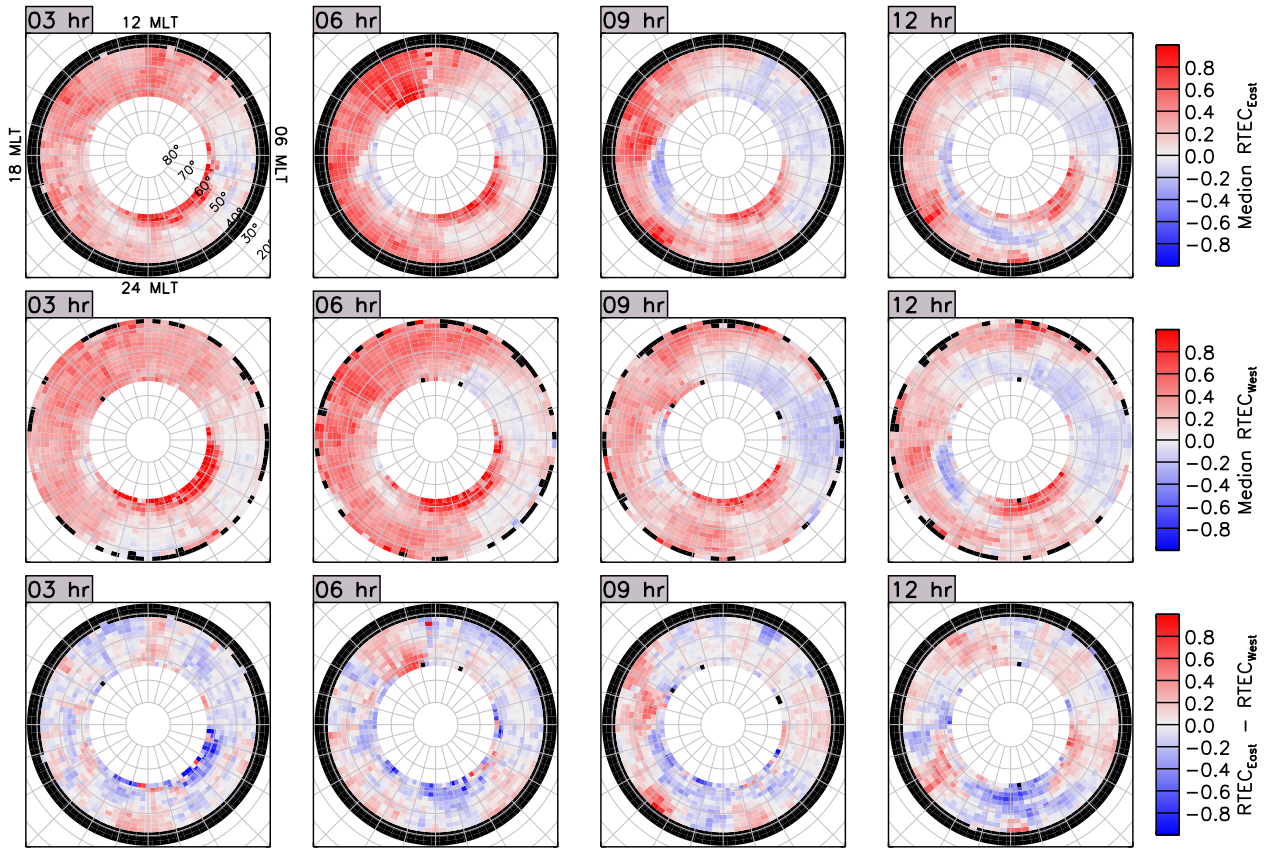

Figure 4.11: Maps of median RTEC using data from (top row) negative and (middle row) positive declination bins, in the same MLAT/MLT format as Figure 4.3. Bottom row shows the difference between the upper and middle panels. Note that regions of negative (positive) declination correspond to bins in the eastern (western) North American sector as depicted in Figure 4.10a.

MLAT/MLT format. Many of the same large-scale morphological features described earlier are observed for both regions but with a few notable differences. First, we find a larger postive enhancement in the post-noon sector for $RTEC_{East}$ ($\sim$0.7) compared to $RTEC_{West}$ ($\sim$0.5). The progression of a dusk trough-like feature to middle latitudes is also observed $\sim$3 hours earlier in the $RTEC_{East}$ results. Furthermore, 12 hours after onset the negative storm effects originating in the dawn sector penetrate 2-3 h deeper into the afternoon region for the $RTEC_{West}$ case.

In the bottom row of Figure 4.11 we highlight these asymmetries more clearly by plot-

ting the difference between median $RTEC_{East}$ and $RTEC_{West}$ values for each 3 h snapshot. Here the positive (red) values indicate a larger increase in TEC for the negative declination region ($RTEC_{East}$) while the negative (blue) values correspond to a larger TEC increase in the positive declination region ($RTEC_{West}$). In this manner we observe the larger dayside positive response in the $RTEC_{East}$ data originating near noon and co-rotating toward midnight in each consecutive frame. We also draw the reader's attention toward higher latitudes on the nightside where darker blues corresponding to more negative values indicate that the positive storm response is stronger over western North America where the declination is positive. These results suggest that there is indeed a longitudinal asymmetry in storm-time TEC changes ordered by the sign of the magnetic field line declination.

4.4 Discussion

We have presented a superposed epoch analysis of GPS TEC variations in the North American sector as a response to geomagnetic storms by fully separating storm-time, local time, and seasonal effects. The TEC response is generally well-ordered by the time of storm main phase onset obtained from the Sym-H index as first suggested by *Thomas and Venables* [1966]. Within the first 3 h after onset a broad positive phase is observed across much of the dayside ionosphere (Figure 4.3), corresponding to a storm-time increase in TEC relative to the 27-day median. At noon the positive storm effect is observed nearly simultaneously across all latitudes (Figure 4.5a). This initial positive phase appears to be a penetration electric field effect as a neutral wind disturbance would take several hours to propagate from high to low latitudes due to the opposition of the poleward-directed background winds. Soon afterwards, the location of the peak positive storm response at noon can be seen progressing toward lower latitudes. This subsequent equatorward progression may instead be the signature of disturbance neutral winds which produce the sustained dayside positive

phase at lower latitudes. We have estimated the velocity of this equatorward progression to be about 200 m/s, which is significantly slower than is often associated with storm-time neutral atmosphere disturbances [*Buonsanto*, 1995; *Lu et al.*, 2008]. While lacking direct observations of storm-time electric field or thermospheric winds, our results suggest that both mechanisms may play a role in uplifting dayside F-region plasma to produce the positive storm effects observed soon after onset.

The dayside positive storm effect maximizes in the post-noon sector near 15 MLT as what is known as a storm enhanced density (SED) plume [*Foster*, 1993]. Previous work has suggested the formation of SED plumes is an episodic phenomenon highly dependent on the time-varying interplanetary magnetic field (IMF) control of the high-latitude convection pattern [*Foster et al.*, 2005; *Thomas et al.*, 2013]. However, we find the SED plume to be a consistently identifiable feature in the North American sector which forms during the first 3 h after onset and disappears 15 h after onset. The SED feature persists longer in winter ($\sim$20 h) than in summer ($\sim$12 h), suggesting its duration is modulated by the progression of negative storm effects originating in the morning sector driven by large-scale thermospheric circulation and composition changes. For comparison, using global TEC data *Liu et al.* [2010] found the winter positive storm response in the afternoon sector (i.e., the SED region) to last for 9-10 h and 12-13 h during moderate and severe disturbance levels. They also reported slightly shorter positive phase durations during summer months of about 7-8 h and 9-10 h respectively. In their study, *Liu et al.* [2010] considered the average TEC response across all longitudes whereas our results indicate longer-duration dayside positive storm effects for the North American sector where SED plumes are believed to occur more frequently [*Yizengaw et al.*, 2008b]. In our future work we will examine the statistical relationship between the occurrence of these SED plumes and solar wind IMF parameters.

Next, we consider the positive and negative storm effects observed at mid- to high lati-

tudes in the nightside ionosphere. Immediately following storm onset, increasingly positive RTEC values are observed in the post-midnight sector between 22-06 MLT. Just equatorward of the auroral oval lies a region of decreased electron density known as the midlatitude ionospheric trough [*Moffett and Quegan*, 1983; *Rodger*, 2008]. Large positive storm effects are observed where the quiet-time low-density trough is "filled in" by the auroral ionization as it expands equatorwards. The trough may also shift equatorward during geomagnetically active conditions [*Rodger et al.*, 1992], forming the latitudinally-narrow negative RTEC feature observed near dusk. Over the next 15 hours this storm-time trough evolves in both latitude and local time before becoming indistinguishable from the broader negative storm effects originating in the morning sector (Figure 4.3). Significant asymmetries are also observed on the nightside when sorting results by season (Figure 4.9). Much broader positive storm effects are observed in winter while the negative trough-like feature is more apparent in summer. This variation may be attributable to the solar illumination control of the seasonal trough morphology [*Voiculescu et al.*, 2006]. Similar winter/summer variations have also been reported in nightside energetic particle precipitation under geomagnetically active conditions [*Newell et al.*, 2010]. Future work is necessary to determine the degree to which the seasonal trough and auroral precipitation morphology may influence the nightside TEC storm response.

The other dominant storm feature identified in our study is the negative RTEC response originating in the post-midnight sector. For the general storm case, this region of decreased TEC is first observed near dawn about 2 hours after storm onset (Figure 4.6c) and reaches the noon and dusk meridians within 8 and 16 hours after onset (Figures 4.5a and 4.6a). The rate at which this negative storm response advances toward later local times is found to be highly dependent on season (Figure 4.9). For instance, during summer we observe negative RTEC values reaching midlatitudes at the noon and dusk meridians within only 7 and 13

hours after storm onset (Figure 4.7) while during winter negative effects are largely restricted to higher latitudes and there is an associated time delay of approximately 16 and 22 hours respectively. Overall we find the largest relative TEC decreases during summer compared to equinox and winter seasons (Figure 4.9a). This is in contrast to some recent statistical studies of the North American [*Mendillo and Klobuchar*, 2006] and European [*Stankov et al.*, 2010] sectors which found the largest negative storm effects to occur during equinox. Overall the results of our seasonal analysis are in good agreement with the classical description of seasonal variations in the ionospheric storm response due to thermospheric circulation and composition changes [*Fuller-Rowell et al.*, 1996; *Rishbeth*, 1998].

For the first time, we have examined TEC storm response as a function of magnetic declination. Previous climatology studies of TEC in North America and Asia have identified a longitudinal asymmetry caused by diurnal variations of zonal thermospheric winds which drive F-region plasma up/down along magnetic field lines depending on the local declination [*Zhang et al.*, 2012; *Zhao et al.*, 2013]. As thermospheric circulation is strongly modified during geomagnetic storms, it has been unclear whether this neutral wind phenomenon remains effective under disturbed conditions. Sorting our results by regions of negative/positive declination (eastern/western North America), we find larger storm-time TEC increases for the negative declination regions on the dayside soon after onset (Figure 4.11, bottom). This region of comparatively-enhanced TEC is observed 3 h after onset and appears to co-rotate in MLT over the next 9 h. Such an enhancement is the opposite response expected for an equatorward-directed meridional wind surge in the dayside ionosphere launched by enhanced Joule heating in the high-latitude auroral zone [*Lu et al.*, 2008]. As the neutral winds reach midlatitudes they acquire a westward motion due to the Coriolis force, which would actually produce a downward plasma drift in regions of negative declination, thus decreasing F-layer densities rather than enhancing them. Our lack of storm-time zonal wind measurements

prevents us from ascribing this dayside RTEC asymmetry to the longitudinal declination effect.

Variations in the nightside TEC storm response shown in Figure 4.11 are more easily understood in terms of the longitudinal declination gradient. *He et al.* [2011] recently examined the global behavior of trough formation under different geomagnetic, seasonal, and declination conditions. They suggested that a deeper trough will form in regions of positive declination during local evening when the quiet-time neutral winds are directed primarily eastward, pushing plasma downward along field lines to altitudes of increased molecular recombination. Similar to the winter scenario, a storm-time trough will therefore produce a smaller negative response in the positive declination region due to the pre-existance of a deeper quiet-time trough. Likewise a larger positive RTEC response will be observed for the same declination geometry as the background trough is ionized by the expanding auroral precipitation. Furthermore, storm-time observations of nightside thermospheric winds have identified a large westward disturbance zonal wind [*Fejer et al.*, 2002] which would also increase the F-layer height of plasma in the positive declination region. Our results appear consistent with this neutral wind mechanism in terms of the relative storm-time changes in TEC observed on the nightside for the positive ($RTEC_{West}$) and negative declination ($RTEC_{East}$) regions.

4.5 Summary

In this paper, we have examined the statistical response of GPS total electron content (TEC) in the North American sector to geomagnetic storms. The Sym-H index was used to identify the main phase onset time of 139 geomagnetic storms from 2001-2013 for a superposed epoch analysis of storm-time changes in GPS TEC relative to a 27-day median. We first presented results for the general case using TEC measurements from all events,

identifying features related to the storm enhanced density (SED) plume, midlatitude density trough, auroral oval, and disturbance composition bulge. The observed progression from an initial positive phase to a longer-lasting negative phase was in good agreement with the classical storm scenario described in terms of peak F-region electron density in review papers such as those by *Prölss* [1995] and *Buonsanto* [1999]. Next, we examined the seasonal variations in TEC storm response for summer, equinox, and winter months. The strongest and longest-lasting positive storm effects are observed in winter while the negative storm response is deepest in summer and progresses across all latitudes/local times more quickly than in other seasons. Finally, we considered the TEC storm response in terms of magnetic declination by separating results according to regions of positive and negative declination. A larger dayside positive response is observed in the negative declination region (eastern North America) with the opposite response expected of a storm-time meridional wind surge. On the nightside, differences in positive and negative storm effects are more easily interpreted in terms of thermospheric zonal winds [*Fejer et al.*, 2002; *He et al.*, 2011].

Acknowledgments

The authors from Virginia Tech thank the National Science Foundation for support under grants AGS-1243070 and AGS-1341918. A.J.C. also thanks the National Science Foundation for support under grant AGS-1243058. S.R.Z. acknowledges NASA LWS funding support (NNX15AB83G). Sym-H indices were obtained from the World Data Center for Geomagnetism in Kyoto (http://wdc.kugi.kyoto-u.ac.jp/). Monthly averaged sunspot numbers were obtained from NASA Marshall Space Flight Center (http://solarscience.msfc.nasa.gov/greenwch/spot_num.txt). GPS TEC data products and access through the Madrigal distributed data system are provided to the community by the Massachusetts Institute of Technology under support from US National Science Foundation grant AGS-1242204. Data for

the TEC processing is provided from the following organizations: UNAVCO; Scripps Orbit and Permanent Array Center; Institut Géographique National, France; International GNSS Service; The Crustal Dynamics Data Information System (CDDIS); National Geodetic Survey; Instituto Brasileiro de Geografia e Estatística; RAMSAC CORS of Instituto Geográfico Nacional de la República Argentina; Arecibo Observatory; Low-Latitude Ionospheric Sensor Network (LISN); Topcon Positioning Systems, Inc.; Canadian High Arctic Ionospheric Network; Institute of Geology and Geophysics; Chinese Academy of Sciences, China Meteorology Administration; Centro di Ricerche Sismologiche; Système d'Observation du Niveau des Eaux Littorales (SONEL); RENAG: REseau NAtional GPS permanent; GeoNet New Zealand; and GNSS Reference Networks. Data from all of these networks were used when computing system biases for the GPS TEC measurements included in this study.

Chapter 5

GPS total electron content observations of ionospheric plasma structures

5.1 Introduction

In Chapter 1 we introduced the topic of ionospheric storms and discussed their relationship to the simultaneous thermospheric storm response. Section 1.5 highlighted several important storm-time phenomena such as the subauroral polarization stream (SAPS), storm enhanced density (SED), tongue of ionization (TOI), polar cap patches, and ionospheric scintillation. So far, we have examined polar cap patch transportation and structuring during a geomagnetic storm (Chapter 3) and the statistical occurrence of SED plumes in the North American sector (Chapter 4). Here, we present an overview of co-authored findings which were enabled by the GPS TEC mapping tools developed for this dissertation research. We emphasize the GPS TEC figures which were contribute/supported and describe how they were used to address the science questions raised in Section 1.5.

5.2 Instantaneous longitudinal variations of the subauroral polarization stream

Previous studies of the subauroral polarization stream (SAPS) derived statistical characterizations from low-altitude spacecraft or incoherent scatter radar measurements restricted

in local time. Using a chain of 6 midlatitude SuperDARN radars in the North American sector, *Clausen et al.* [2012] presented the first simultaneous velocity measurements within a SAPS feature across 3 hours of Universal Time and 6 hours of MLT (Figure 5.1). They found the SAPS velocity magnitude to decrease exponentially with MLT in the morning sector, in contrast to the linear relationship previously reported by *Erickson et al.* [2011]. This longitudinal variation was suggested to be the result of pressure gradients in the ring current. Although the GPS TEC data were not able to contribute direct measurements of the SAPS structure, they did play a valuable role by demonstrating that the SAPS irregularities observed by the SuperDARN radars were located near the poleward wall of a trough-like depletion (top panel in Figure 5.1). This collocation of the velocity and density measurements supported the mechanism of SAPS electric field developing in a region of low ionospheric conductivity. Additional investigation of SAPS events observed by midlatitude SuperDARN radars indicate this is a repeatable characteristic of the backscatter location.

Clausen, L. B. N., J. B. H. Baker, J. M. Ruohoniemi, R. A. Greenwald, **E. G. Thomas**, S. G. Shepherd, E. R. Talaat, W. A. Bristow, Y. Zheng, A. J. Coster, and S. Sazykin (2012), Large-scale observations of a subauroral polarization stream by midlatitude SuperDARN radars: Instantaneous longitudinal velocity variations, *J. Geophys. Res.*, 117, A05306, doi:10.1029/2011JA017232.

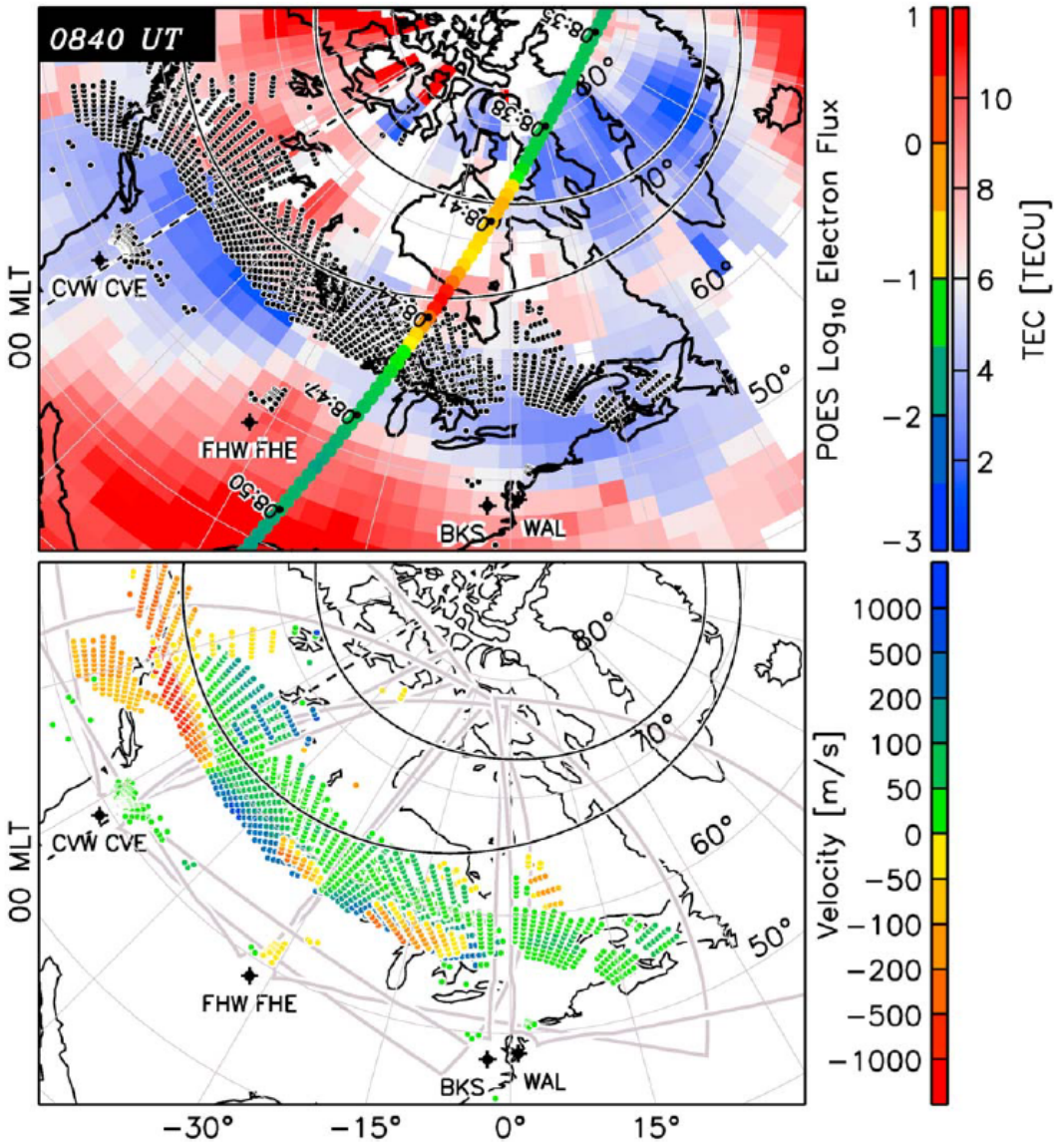

Figure 5.1: Overview of the measurements made of the SAPS channel by all six midlatitude radars on 09 April 2011, 0840 UT in magnetic coordinates. (top) Median- filtered GPS TEC measurements colored blue to red. The large colored dots show the down-going electron flux measured by the POES-18 satellite along its track; the times of the measurements are given next to the track. The small black dots give the locations of velocity measurements made by the six radars. (bottom) The measured velocities, now color-coded according to the color bar on the right; note the non-linear scaling. We also show the radar FOVs as gray lines. In both panels we show the auroral oval for a Kp index of 2 and mark the 00 MLT meridian by a dashed line [*Clausen et al.*, 2012].

5.3 Electrodynamical and neutral processes in storm-time plasma structuring and transport

Zou et al. [2013] sought to address the specific formation mechanisms of an SED plume structure observed within the field of view of the Poker Flat Incoherent Scatter Radar (PFISR). Global maps of GPS TEC and SuperDARN potential patterns were again used to image the large-scale morphology of the SED plume. They identified a SAPS feature which, coupled with an equatorward expansion of the high-latitude convection pattern, transported the storm-enhanced dayside plasma toward noon as an SED plume. Other mechanisms contributing to the SED formation included a vertical componenet of the $\mathbf{E}\times\mathbf{B}$ drift further raising the plasma to regions of decreased recombination, energetic particle precipitation, and topside thermospheric winds. Next, *Zou et al.* [2014] expanded their multi-instrument analysis of SED formation and decay mechanisms to include observations during six geomagnetic storm intervals from 2010-2013. Figure 5.2 shows combined TEC/SuperDARN maps for each of the six events with the PFISR beam directions overlaid as black segments. From the PFISR observations they identified a mixture of four different plasma drift geometries within the six plumes - two cases of upwards drift during formation (vertical projection of $\mathbf{E}\times\mathbf{B}$ motion and field-aligned flow) and two cases of downward drift during decay (possibly ambipolar diffusion or poleward thermospheric winds). These results indicated the extremely dynamic nature of SED plumes from one event to another despite the consistent occurrence found in Chapter 4.

More recently, *Liu et al.* [2015] examined SED/TOI characteristics under moderately disturbed conditions during the late recovery phase of a geomagnetic storm. This is in contrast to much of the prior literature which has focused on plume features observed under strongly disturbed storm conditions [e.g., *Foster et al.*, 2005; *Zou et al.*, 2013]. Here the solar

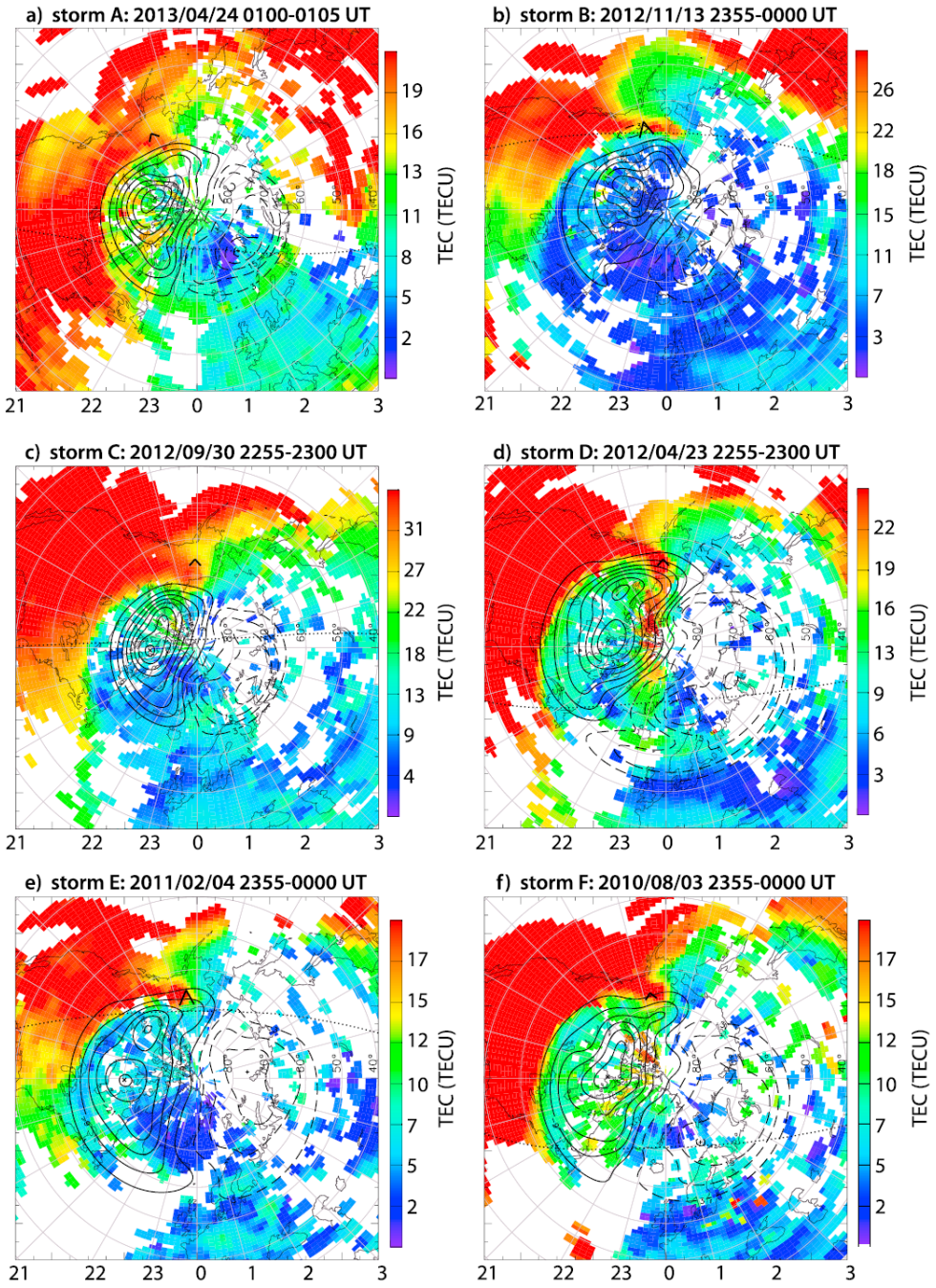

Figure 5.2: Selected 2-D GPS VTEC observations of the SED plumes during six geomagnetic storms. Ionospheric equipotential contours derived from the SuperDARN radar observations are superposed as solid and dashed black lines. PFISR field of view is outlined by black segments and the terminator is also shown as a dotted line in each frame [*Zou et al.*, 2014].

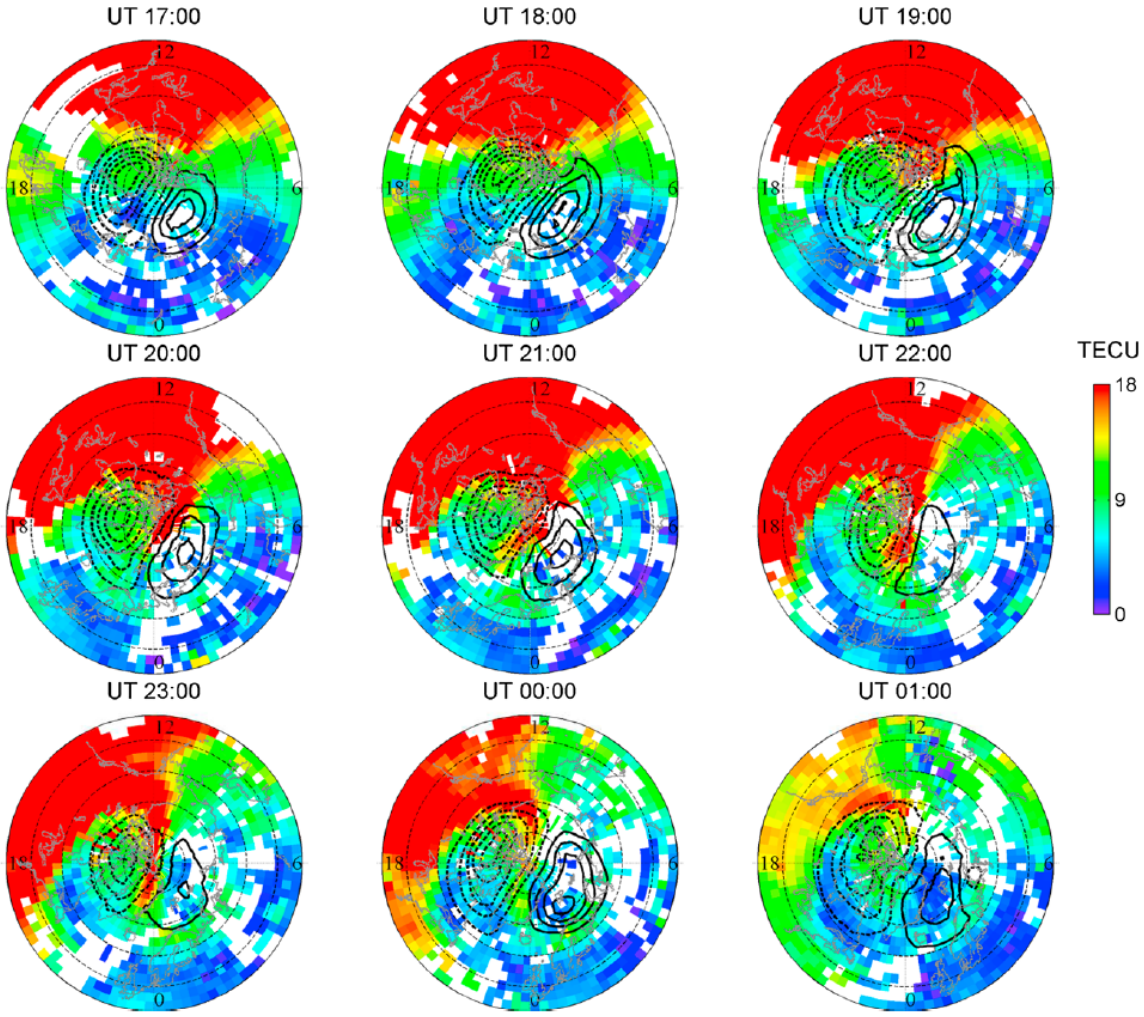

Figure 5.3: Sequences of GPS TEC maps in the coordinates of MLAT (40°)-90°) and MLT during 1700 UT on 14 October to 0100 on 15 October 2012. Plasma convection patterns observed by SuperDARN are superposed [*Liu et al.*, 2015].

wind driving parameters were quite weak with the IMF B_y and B_z components fluctuating between -5 nT and 5 nT throughout the SED/TOI interval. *Liu et al.* [2015] reported horizontal transport via an expanded high-latitude convection pattern (Figure 5.3) and SAPS electric field as the primary SED/TOI formation mechanism, with no observed signatures of penetration electric fields redistributing plasma from equatorial latitudes. Equatorward-driven storm-time neutral winds were also suggested as a possible contributor by reducing the downward ambipolar diffusion along field lines. Finally, a longitudinal preference for SED/TOI formation was invoked to explain the presence of a relatively weaker TOI structure observed earlier under much stronger driving conditions (IMF $B_z < -15$ nT) during the main phase of the storm. These results demonstrate the need for a more complete statistical characterization of SED and TOI formation mechanisms under a variety of geomagnetic activity conditions.

Polar cap patches are by definition much smaller-scale structures than the TOI which can extend across many thousands of km in the noon-midnight meridian. Until the deployment of GPS receiver networks within the polar cap, observations of patch dynamics were largely confined to a single imager or radar field of view. This also limited the capability for tracking individual patches for more than just a few hours. For the first time, *Zhang et al.* [2013] was able to track the complete lifecycle of a polar cap patch including its formation on the dayside, transport across the polar cap, exit, on the nightside, and dayside return at auroral latitudes in the dusk convection cell. The evolution of this patch can be tracked by following the TEC enhancements within the blue circles in each panel of Figure 5.4. *Zhang et al.* [2013] found that modulation of nightside reconnection occuring in the tail plays a key role in both the formation of patches and their region of exit on the nightside ionosphere. The reliance on GPS TEC observations for patch identification was in fact one of the primary motivations behind the multi-instrument comparison performed in Chapter 3.

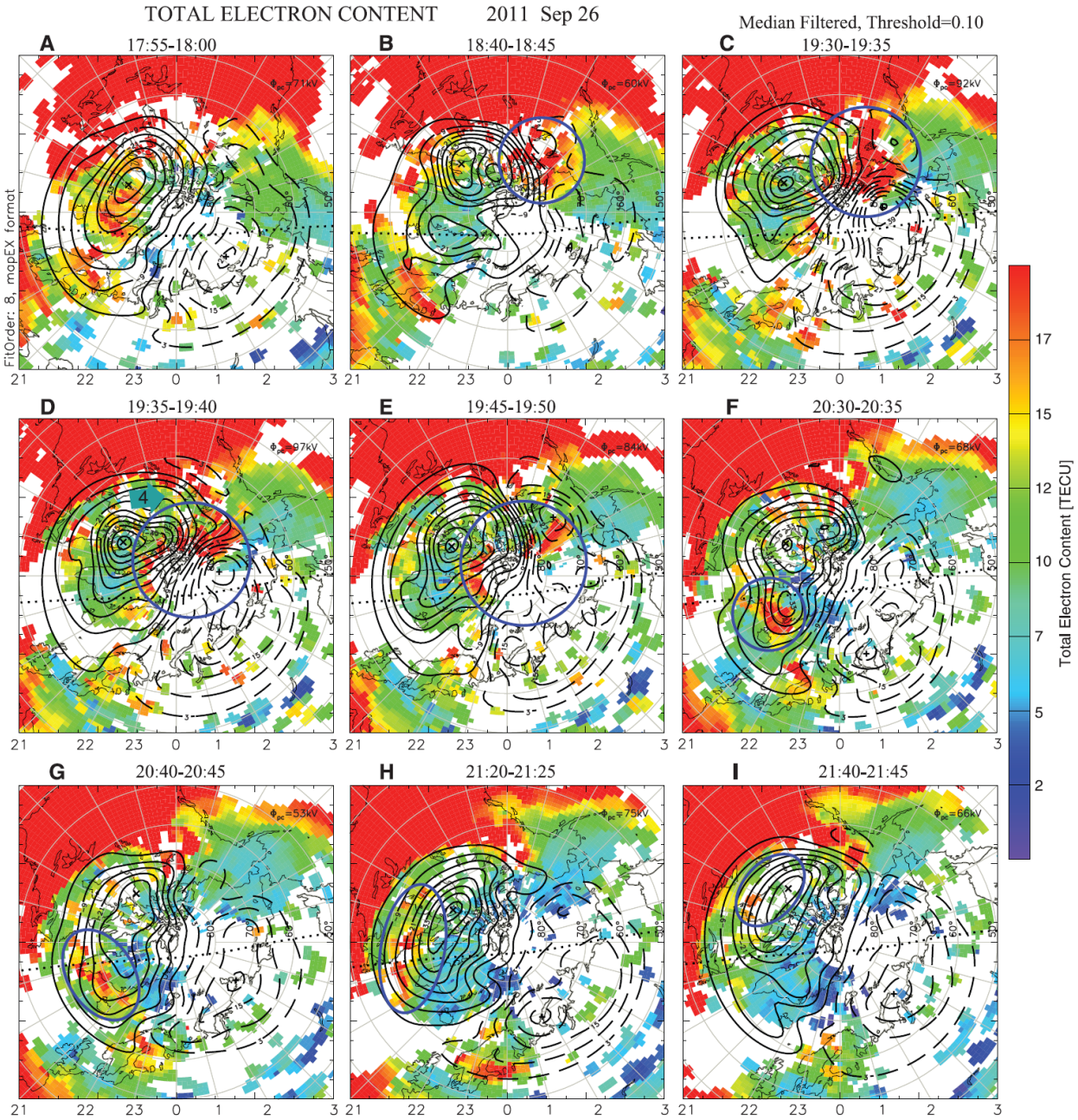

Figure 5.4: (A to I) Extracts from a full series of 2D maps of median-filtered TEC and ionospheric convection on a geomagnetic latitude/magnetic local time (MLT) grid with noon at the top. The dotted line across each panel is the day-night terminator at 100-km altitude. The blue circles and ellipses highlight the polar cap patch, the evolution of which is followed in this figure [*Zhang et al.*, 2013].

Zou, S., A. J. Ridley, M. Moldwin, M. J. Nicolls, A. J. Coster, **E. G. Thomas**, and J. M. Ruohoniemi (2013), Multi-instrument observations of SED during 24-25 October 2011 storm: Implications for SED formation processes, *J. Geophys. Res. Space Physics*, 118, 7798–7809, doi:10.1002/2013JA018860.

Zou, S., M. Moldwin, A. J. Ridley, M. J. Nicolls, A. J. Coster, **E. G. Thomas**, and J. M. Ruohoniemi (2014), On the generation/decay of the storm-enhanced density (SED) plumes: Role of the convection flow and field-aligned ion flow, *J. Geophys. Res. Space Physics*, 119, 8543–8559, doi:10.1002/2014JA020408.

Liu, J., T. Nakamura, L. Liu, W. Wang, N. Balan, T. Nishiyama, M. R. Hairston, and **E. G. Thomas** (2015), Formation of polar tongue of ionization during minor geomagnetic disturbed conditions, *J. Geophys. Res. Space Physics*, 120, 6860–6873, doi:10.1002/2015JA021393.

Zhang, Q.-H., B.-C. Zhang, M. Lockwood, H.-Q. Hu, J. Moen, J. M. Ruohoniemi, **E. G. Thomas**, S.-R. Zhang, H.-G. Yang, R.-Y. Liu, K. A. McWilliams, and J. B. H. Baker (2013), Solar control of near-Earth space: direct observations of the evolution of polar cap patches, *Science*, 339, 1597–1600, doi:10.1123/science.1231487.

5.4 Occurrence and intensity of high-latitude GPS phase scintillation during geomagnetic storms

As discussed in Section 1.5.4, GPS amplitude and phase scintillation can occur when small-scale plasma irregularities grow along electron density gradients associated with polar cap patches or TOI. These indices are typically recorded using high-precision GPS receivers with sampling rates of at least 50 Hz. Because there are a limited number of GPS receivers with such a high sampling rate located within the polar cap, a delta phase rate (DPR) proxy index has been developed to supplement localized σ_Φ measurements with additional observations from low-rate (1 Hz) GPS receivers [*Ghoddousi-Fard and Lahaye*, 2012]. A series of multi-instrument case studies have used this proxy index for characterizing scintillation occurrence and intensity during geomagnetic storm intervals. First, *Prikryl et al.* [2013] analyzed a moderate storm (Dst = -61 nT) in November 2011 where a TOI and several patches were observed. They found the most intense scintillation to be collocated with SuperDARN

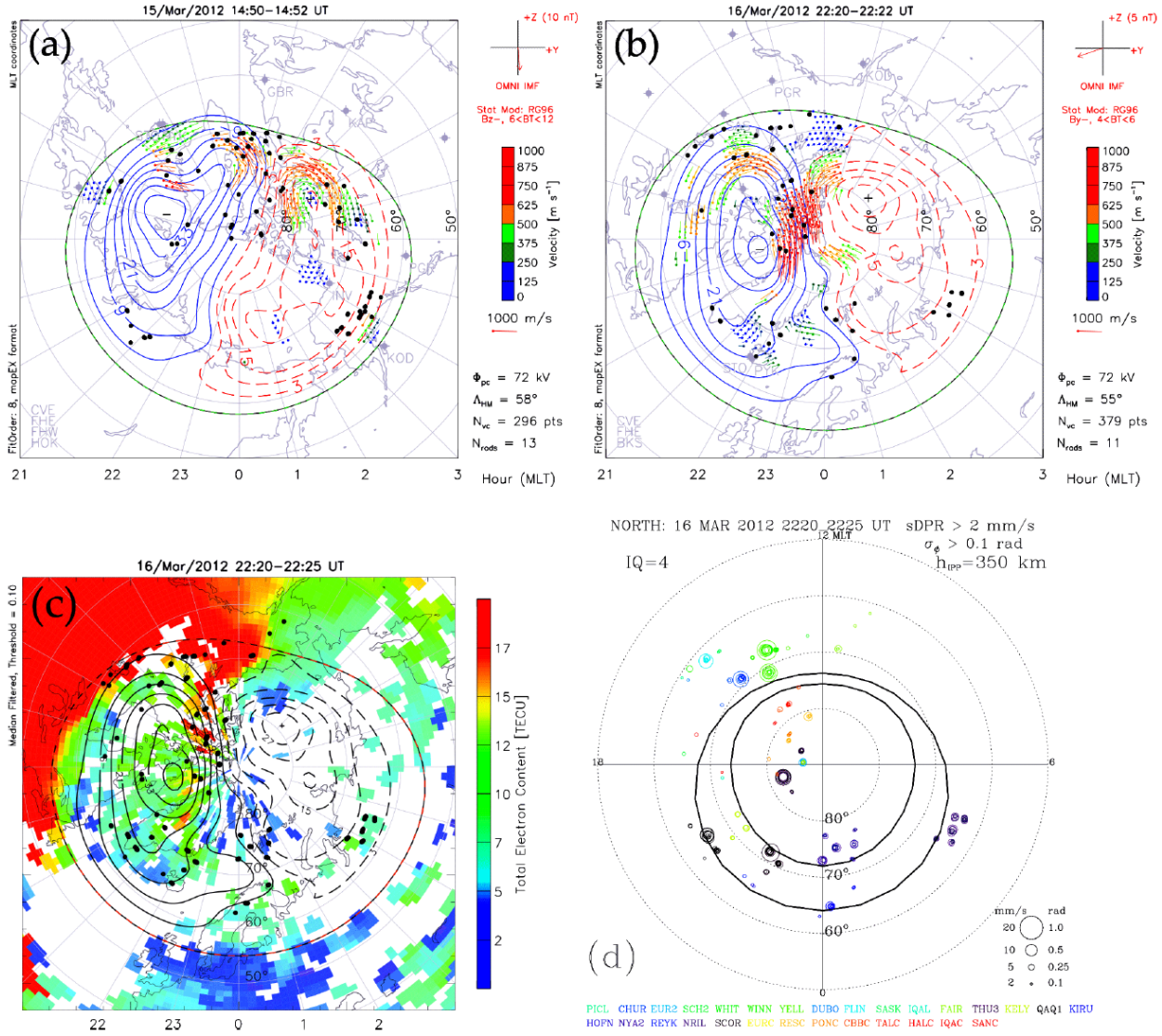

Figure 5.5: (a-b) Event S4: SuperDARN convection and potential maps on 15 and 16 March. The IPPs for PRNs with $\sigma_\Phi > 0.1$ rad and/or sDPR > 2 mms^{-1} are superposed as black dots. (c) The 5 min median-filtered TEC mapped in coordinates of AACGM latitude and MLT is overlaid with the SuperDARN potential map and IPPs (black dots) for $\sigma_\Phi > 0.1$ rad or sDPR > 2 mms^{-1}. (d) The IPPs are shown as circles scaled proportionally to σ_Φ and sDPR values [*Prikryl et al.*, 2015a].

HF radar backscatter in the cusp and within a dense TOI feature being convected across the polar cap at speeds exceeding 1500 m/s. Weaker phase scintillation was observed at midlatitudes along the poleward edge of a SAPS feature near the auroral oval.

This case study was followed by a pair of companion articles focused on the 7-17 March 2012 interval marked by a series of four geomagnetic storms driven by coronal mass ejections (CMEs). *Prikryl et al.* [2015a] examined the North American sector and compared proxy scintillation indices under negative and positive IMF B_z conditions. During southward B_z enhanced scintillation occurred in the polar cap near patches which detached from a TOI (Figure 5.5c), while under northward IMF the strongest scintillation was caused by transpolar arcs. The black dots overlaid on the GPS TEC data and convection pattern in Figure 5.5c correspond to ionospheric pierce points of intense phase scintillation. In their companion paper, *Prikryl et al.* [2015b] compared interhemispheric aspects of scintillation during the same events. They found the IMF B_y component to control the MLT of scintillation mapping to the cusp entry of SED plasma into the polar cap. Finally, *Prikryl et al.* [2015c] presented observations from a pair of storm intervals to demonstrate the relationship between scintillation occurrence in the polar cap and auroral oval with magnetospheric processes associated with patches and substorm onset.

Prikryl, P., R. Ghoddousi-Fard, B. S. R. Kunduri, **E. G. Thomas**, A. J. Coster, P. T. Jayachandran, E. Spanswick, and D. W. Danskin (2013), GPS phase scintillation and proxy index at high latitudes during a moderate geomagnetic storm, *Ann. Geophys.*, 31, 805–816, doi:10.5194/angeo-31-805-2013.

Prikryl, P., R. Ghoddousi-Fard, **E. G. Thomas**, J. M. Ruohoniemi, S. G. Shepherd, P. T. Jayachandran, D. W. Danskin, E. Spanswick, Y. Zhang, Y. Jiao, and Y. T. Morton (2015), GPS phase scintillation at high latitudes during geomagnetic storms of 717 March 2012 Part 1: The North American sector, *Ann. Geophys.*, 33, 636–656, doi:10.5194/angeo-33-637-2015.

Prikryl, P., R. Ghoddousi-Fard, L. Spogli, C. N. Mitchell, G. Li, B. Ning, P. J. Cilliers, V. Sreeja, M. Aquino, M. Terkildsen, P. T. Jayachandran, Y. Jiao, Y. T. Morton, J. M. Ruohoniemi, **E. G. Thomas**, Y. Zhang, A. T. Weatherwax, L. Alfonsi, G. De Franceschi, and V. Romano (2015), GPS phase scintillation at high latitudes during geomagnetic storms of 717 March 2012 Part 2: Interhemispheric comparison, *Ann. Geophys.*, 33, 657–670, doi:10.5194/angeo-33-657-2015.

Prikryl, P., R. Ghoddousi-Fard, J. M. Ruohoniemi, and **E. G. Thomas** (2015), *GPS Phase Scintillation at High Latitudes during Two Geomagnetic Storms, in Auroral Dynamics and*

Space Weather (eds Y. Zhang and L. J. Paxton), John Wiley & Sons, Inc, Hoboken, NJ, doi: doi:10.1002/9781118978719.ch15.

Chapter 6

Conclusions and Future Work

6.1 Summary of Results

The motivation for this research was to gain a better understanding of storm-time ionospheric density structuring in the mid- to high latitude ionosphere. In Chapter 2, we introduced the primary data sets used in this research: global maps of GPS total electron content (TEC), HF radar measurements of Doppler velocity and backscatter from small-scale plasma irregularities, 630.0 nm red line all-sky airglow images, the *Dst* and Sym-H ring current indices, the auroral electrojet (AE) index, and OMNI interplanetary solar wind measurements. This chapter concluded with a discussion of newly available online plotting tools which allow users to generate figures combining TEC, SuperDARN, and airglow data.

Next, an analysis of polar cap patch structuring and transport during a moderate geomagnetic storm was presented in Chapter 3. These patches were simultaneously tracked from their dayside origin across the polar cap to the nightside auroral oval, allowing for comparison of patch location, velocity, and horizontal extent across the three independent data sets (optical, radar, and GPS TEC). On the dayside near the cusp, small-scale irregularities producing HF backscatter were distributed throughout newly formed patches. This allowed SuperDARN radars to follow the patch trajectories through sunlit regions contaminating the imager field of view. The correspondence between GPS TEC and 630.0 nm all-sky airglow observations of patches was also tested using a correlation analysis. While global maps

of GPS TEC may be used to extend patch observations beyond the imager fields of view, kilometer-scale resolution is necessary to fully capture patch structuring mechanisms such as the gradient drift instability. Lastly, the dawn-dusk width of patches during geomagnetically quiet versus active periods was considered in terms of dayside generation processes and relaxation of the nightside convection pattern. This study clearly demonstrated the advantages of monitoring polar cap patches using a multi-instrument approach with complementary observational capabilities.

In Chapter 4 a superposed epoch analysis was performed to characterize the average response of GPS TEC in the North American sector during more than 100 geomagnetic storms over a 13-year interval. This approach differed from previous regional and global TEC storm studies by fully separating the local time, storm-time, longitudinal, and seasonal effects. Our results for the general storm response were in good agreement with the classical storm scenario, with an initial dayside positive phase followed by a longer-lasting negative storm phase. We also found the strongest and longest lasting positive storm effects to occur during winter while the negative storm response was deepest in summer months. For the first time, we tested the TEC storm response as a function of magnetic declination by separating results into regions of positive or negative declination. Significant asymmetries were identified such that a stronger positive storm response was observed in regions of negative declination (eastern North America). On the nightside, differences in positive and negative storm effects may be due to neutral wind modulation of the midlatitude trough region.

Finally, in Chapter 5 we summarized several co-authored studies which examined various storm-time phenomena utilizing GPS TEC mapping tools developed for this dissertation research. These features included the subauroral polarization stream (SAPS) and density trough, storm enhanced density (SED) plume, tongue of ionization (TOI), and polar cap patches. This chapter concluded with a discussion of phase scintillation on GPS navigation

signals and how its occurrence can be related to these various storm-time electron density perturbations. An emphasis was placed on describing the specific figures in these papers which were produced via the GPS TEC mapping tools developed for this dissertation research.

6.2 Publications and Presentations

Results from this work have been presented at the AGU Fall Meeting [2013, 2014, 2015], AOGS Annual Meeting [2014], CEDAR workshop [2014], GEM workshop [2014, 2015], Ionospheric Effects Symposium [2015], JSPS Multidisciplinary Science Forum [2014], SuperDARN workshop [2013, 2014, 2015], and VSGC Graduate Student Research Symposium [2013, 2014]. One article has been published in Radio Science [*Thomas et al.*, 2015] and one manuscript has been accepted for publication in Journal of Geophysical Research: Space Physics [*Thomas et al.*, 2016]. Eleven co-authored papers [*Clausen et al.*, 2012; *Kunduri et al.*, 2012; *Zhang et al.*, 2013; *Prikryl et al.*, 2013, 2015a,b; *Zou et al.*, 2013, 2014; *Walsh et al.*, 2015; *Liu et al.*, 2015; *Joshi et al.*, 2015] and two refereed book chapters [*Prikryl et al.*, 2015c; *Coster et al.*, 2016] have been published using GPS TEC mapping tools developed for this research.

6.3 Suggestions for Future Work

Throughout the course of this research the limitations of relying solely upon one data set to characterize the ionospheric state have become readily apparent. For example, while the global maps of GPS TEC are quite powerful for imaging large-scale horizontal plasma structure, they provide no information regarding the altitudinal profile or peak electron density. Also, we have not yet been able to include any neutral wind observations to test our

suggestion of a magnetic declination asymmetry in storm-time TEC response. Some specific recommendations for future work thus include the following:

1. Perform a more rigorous statistical comparison between 630.0 nm airglow intensity measurements of polar cap patches with coarser GPS TEC data, similar to Section 3.3.3. This analysis would ideally be performed within the field of view of an incoherent scatter radar, such as RISR or EISCAT, for an accurate determination of the peak airglow emission altitude for mapping purposes.

2. Compare polar cap patch formation during geomagnetically quiet and active conditions, specifically to test whether the dawn-dusk extent is truly different in a statistical sense. Multi-instrument ground-based observations similar to those used in Chapter 3 could be combined with in situ rocket or low-latitude spacecraft observations to test mesoscale formation processes.

3. Repeat the GPS TEC storm analysis performed in Chapter 4 for additional geographic regions with sufficient GPS receiver coverage such as Europe, South America, or East Asia. By comparing with results obtained for the North American sector, one could test the degree to which SED plumes truly occur more frequently in specific longitude sectors due to the offset between geographic and geomagnetic dipoles as well as extend the study of longitudinal/declination effects on storm-time TEC response.

4. Perform case studies of ionospheric storm response specifically targeted towards magnetic declination asymmetries identified in Section 4.3.4. Such a study would require accurate knowledge of storm-time neutral winds from instruments such as incoherent scatter radars or Fabry-Perot interferometers (FPIs) in addition to the widely available GPS TEC measurements.

5. Construct an empirical model using the GPS TEC storm response calculated in Chapter 4. For future predictive purposes, techniques such as dynamic interpolation or empirical orthogonal functions (EOFs) may be necessary to account for the sparse occurence of storms in time/season/magnitude. Such a model would have immediate application as a space weather prediction tool, allowing the user to infer the development of specific storm features in the ionosphere over North America following storm onset.

References

Aarons, J., (1982), Global morphology of ionospheric scintillations, *Proc. IEEE*, **70**(4), 360–378, doi:10.1109/PROC.1982.12314.

Balan, N., and P. B. Rao (1990), Dependence of ionospheric response on the local time of sudden commencement and the intensity of geomagnetic storms, *J. Atmos. Terr. Phys.*, *52*(4), 269–275, doi:10.1016/0021-9169(90)90094-4.

Baker, K. B., and S. Wing (1989), A new magnetic coordinate system for conjugate studies at high latitudes, *J. Geophys. Res.*, *94*(A7), 9139-9143, doi:10.1029/JA094iA07p09139.

Barbier, D., F. E. Roach, and W. R. Steiger (1962), The summer intensity variations of [OI] 6300 Åin the tropics, *J. Res. Nat. Bur. Stand. - D. Radio Propagation*, *66D*(1), 145–152, doi:10.6028/jres.066D.017.

Blanc, M., and A. D. Richmond (1980), The ionospheric disturbance dynamo, *J. Geophys. Res.*, *85*(A4), 1669-1686, doi:10.1029/JA085iA04p01669.

Borries, C., J. Berdermann, N. Jakowski, and V. Wilken (2015), Ionospheric storms - A challenge for empirical forecast of the total electron content, *J. Geophys. Res. Space Physics*, *120*, 3175–3186, doi:10.1002/2015JA020988.

Buchau, J., B. W. Reinisch, E. J. Weber, and J. G. Moore (1983), Structure and dynamics of the winter polar cap *F* region, *Radio Sci.*, *18*(6), 995–1010, doi:10.1029/RS018i006p00995.

Buchau, J., E. J. Weber, D. N. Anderson, H. C. Carlson Jr., J. G. Moore, B. W. Reinisch, and R. C. Livingston (1985), Ionospheric structures in the polar cap: Their origin and relation to 250-MHz scintillation, *Radio Sci.*, *20*(3), 325–338, doi:10.1029/RS020i003p00325.

Buonsanto, M. J. (1995), A case study of the ionospheric storm dusk effect, *J. Geophys. Res.*, *100*(A12), 23857–23869, doi:10.1029/95JA02697.

Buonsanto, M. J. (1999), Ionospheric Storms – A review, *Space Sci. Rev.*, *88*, 563–601, doi:10.1023/A:1005107532631.

Bust, G. S., and G. Crowley (2007), Tracking of polar cap ionospheric patches using data assimilation, *J. Geophys. Res.*, *112*, A05307, doi:10.1029/2005JA011597.

Carlson, H. C., K. Oksavik, J. Moen, and T. Pederson (2004), Ionospheric patch formation: Direct measurements of the origin of a polar cap patch, *Geophys. Res. Lett.*, *31*, L088061, doi:10.1029/2003GL018166.

Carlson, H. C. (2012), Sharpening our thinking about polar cap ionospheric patch morphology, research, and mitigation techniques, *Radio Sci.*, *47*, RS0L21, doi:10.1029/2011RS004946.

Chapman, S. and J. Bartels (1940), The morphology of magnetid disturbance, in *Geomagnetism*, vol. 1, chap. 9, pp. 272–337, Clarendon, Oxford.

Chen, Y., W. Wang, A. G. Burns, S. Liu, J. Gong, X. Yue, G. Jiang, and A. Coster (2015), Ionospheric response to CIR-induced recurrent geomagnetic activity during the declining phase of solar cycle 23, *J. Geophys. Res. Space Physics*, *120*, 1394–1418, doi:10.1002/2014JA020657.

Chen, Z., S.-R. Zhang, A. J. Coster, and G. Fang (2015), EOF analysis and modeling of GPS TEC climatology over North America, *J. Geophys. Res. Space Physics*, *120*, 3118–3129, doi:10.1002/2014JA020837.

Chisham, G., et al. (2007), A decade of the Super Dual Auroral Radar Network (SuperDARN): Scientific achievements, new techniques and future directions, *Surv. Geophys.*, *28*(1), 33–109, doi:10.1007/s10712-007-9017-8.

Chisham, G., T. K. Yeoman, and G. J. Sofko (2008), Mapping ionospheric backscatter measured by the SuperDARN HF radars Part 1: A new empirical virtual height model, *Ann. Geophys.*, **26**, 823–841, doi:10.5194/angeo-26-823-2008.

Clausen, L. B. N., et al. (2012), Large-scale observations of a subauroral polarization stream by midlatitude SuperDARN radars: Instantaneous longitudinal velocity variations, *J. Geophys. Res.*, *117*, A05306, doi:10.1029/2011JA017232.

Coster, A. J., J. C. Foster, P. J. Erickson, and F. J. Rich (2001), Regional GPS mapping of storm enhanced density during the 15-16 July 2000 geomagnetic storm, in *ION GPS 2001 Proceedings*, Salt Lake City, Utah, 2531–2539.

Coster, A. J. (2011), A Student Tutorial: Using GPS to Study Magnetospheric-Ionospheric Coupling, *CEDAR-GEM Joint Workshop, Santa Fe, NM.*

Coster, A. J., P. J. Erickson, J. C. Foster, E. G. Thomas, J. M. Ruohoniemi, and J. B. H. Baker (2016), Solar Cycle 24 Observations of Storm Enhanced Density and the Tongue of Ionization, in *Ionospheric Space Weather: Longitude and Hemispheric Dependencies and Their Solar, Geomagnetic, and Lower Atmosphere Connections* (eds. T. J. Fuller-Rowell, E. Yizengaw, P. H. Doherty, and S. Basu), John Wiley & Sons, Inc, Hoboken, NJ.

Crowley, G. (1996), Critical review of ionospheric patches and blobs, in *Review of Radio Science 1993-1996*, edited by W. R. Stone, pp. 619–648, Oxford Univ. Press, New York.

Dahlgren, H., G. W. Perry, J. L. Semeter, J.-P. St.-Maurice, K. Hosokawa, M. J. Nicolls, M. Greffen, K. Shiokawa, and C. Heinselman (2012), Space-time variability of polar cap patches: Direct evidence for internal plasma structuring, *J. Geophys. Res.*, *117*, A09312, doi:10.1029/2012JA017961.

Davies, J. A., T. K. Yeoman, I. J. Rae, S. E. Milan, M. Lester, M. Lockwood, and A. McWilliams (2002), Ground-based observations of the auroral zone and polar cap ionospheric responses to dayside transient reconnection, *Ann. Geophys.*, **20**, 781–794, doi:10.5194/angeo-20-781-2002.

Davis, T. N., and M. Sugiura (1966), Auroral electrojet activity index AE and its univeral time variations, *J. Geophys. Res.*, *71*(3), 785–801, doi:10.1029/JZ071i003p00785.

Erickson, P. J., F. Beroz, and M. Z. Miskin (2011), Statistical characterization of the American sector subauroral polarization stream using incoherent scatter radar, *J. Geophys. Res.*, *116*, A00J21, doi:10.1029/2010JA015738.

Evans, J. V. (1957), The electron content of the ionosphere, *J. Atmos. Terr. Phys.*, *11*(3), 259–271, doi:10.1016/0021-9169(57)90071-5.

Fejer, B. G., J. T. Emmert, and D. P. Sipler (2002), Climatology and storm time dependence of nighttime thermospheric neutral winds over Millstone Hill, *J. Geophys. Res.*, *107*(A5), doi:10.1029/2001JA000300.

Finlay, C. C., et al. (2010), International Geomagnetic Reference Field: the eleventh generation, *Geophys. J. Int.*, *183*, 1216–1230, doi:10.1111/j.1365-246X.2010.04804.x.

Foster, J. C. (1993), Storm time plasma transport at middle and high latitudes, *J. Geophys. Res.*, *98*(A2), 1675–1689, doi:10.1029/92JA02032.

Foster, J. C., and W. J. Burke (2002), SAPS: A new categorization for sub-auroral electric fields, *EOS Trans. AGU*, *83*(36), 393, doi:10.1029/2002EO000289.

Foster, J. C., and H. B. Vo (2002), Average characteristics and activity dependence of the subauroral polarization stream, *J. Geophys. Res.*, *107*(A12), 1475, doi:10.1029/2002JA009409.

Foster, J. C., et al. (2005), Multiradar observations of the polar tongue of ionization, *J. Geophys. Res.*, *110*(A9), A09S31, doi:10.1029/2004JA010928.

Foster, J. C., W. Rideout, B. Sandel, W. T. Forrester, and F. J. Rich (2007), On the relationship of SAPS to storm-enhanced density, *J. Atmos. Terr. Phys.*, *69*(3), 303–313, doi:10.1016/j.jastp.2006.07.021.

Fuller-Rowell, T. J., M. V. Codrescu, R. J. Moffett, and S. Quegan (1994), Response of the thermosphere and ionosphere to geomagnetic storms, *J. Geophys. Res.*, *99*(A3), 3893-3914, doi:10.1029/93JA02015.

Fuller-Rowell, T. J., M. V. Codrescu, H. Rishbeth, R. J. Moffett, and S. Quegan (1996), On the seasonal response of the thermosphere and ionosphere to geomagnetic storms, *J. Geophys. Res.*, *101*(A2), 2343-2353, doi:10.1029/95JA01614.

Galperin, Y., V. N. Ponomarev, and A. G. Zosimov (1974), Plasma convection in the polar ionosphere, *Ann. Geophys.*, *30*, 1–7.

Getting, I. A. (1993), Perspective/navigation-the global positioning system, *IEEE Spectrum*, *30*(12), 37–38, doi:10.1109/6.272176.

Ghoddousi-Fard, R., and F. Lahaye (2012), Monitoring GPS phase rate variations as a proxy scintillation index, *AGU Fall Meeting, San Francisco, CA*.

Gondarenko, N. A., P. N. Guzdar, J. J. Sojka, and M. David (2003), Structuring of high latitude plasma patches with variable drive, *Geophys. Res. Lett.*, *30*(4), 1165, doi:10.1029/2002GL016437.

Gondarenko, N. A., and P. N. Guzdar (2004), Plasma patch structuring by the nonlinear evolution of the gradient drift instability in the high-latitude ionosphere, *J. Geophys. Res.*, *109*, A09301, doi:10.1029/2004JA010504.

Gonzalez, W. D., A. L. Clúa de Gonzalez, O. Mendes Jr., and B. T. Tsurutani (1992), Difficulties defining storm sudden commencement, *EOS Trans. AGU*, *73*(16), 180-181, doi:10.1029/91EO00148.

Gonzalez, W. D., J. A. Joselyn, Y. Kamide, H. W. Kroehl, G. Rostoker, B. T. Tsurutani, and V. M. Vasyliunas (1994), What is a geomagnetic storm?, *J. Geophys. Res.*, *99*(A4), 5771-5792, doi:10.1029/93JA02867.

Goodwin, L. V., B. Iserhienrhien, D. M. Miles, S. Patra, C. van der Meeren, S. C. Buchert, J. Burchill, L. B. N. Clausen, D. J. Knudsen, K. A. McWilliams, and J. Moen (2015), Swarm in situ observations of F-region polar cap patches created by cusp precipitation, *Geophys. Res. Lett.*, *42*, 996–1003, doi:10.1002/2014GL062610.

Greenwald, R. A., K. B. Baker, R. A. Hutchins, and C. Hanuise (1985), An HF phased-array radar for studying small-scale structure in the high-latitude ionosphere, *Radio Sci.*, *20*(1), 63–79, doi10.1029/RS020i001p00063.

Greenwald, R. A., et al. (1995), DARN/SUPERDARN: A global view of the dynamics of high-latitude convection, *Space Sci. Rev.*, *71*(1), 761–796, doi:10.1007/BF00751350.

Guier, W. H. and G. C. Weiffenbach (1993), A satellite Doppler navigation system, *Proceedings of the IRE*, *48*(4), 507–516, doi:10.1109/JRPROC.1960.287399.

He, M., L. Liu, W. Wan, and B. Zhao (2011), A study on the nighttime midlatitude ionospheric trough, *J. Geophys. Res.*, *116*, A05315, doi:10.1029/2010JA016252.

Hearn, A. L. (1974), Longitudinal effect in the response of total electron content to magnetic storms, *Nature*, *249*, 133-134, doi:10.1038/249133a0.

Heppner, J. P., and N. C. Maynard (1987), Empirical high-latitude electric field models, *J. Geophys. Res.*, *92*(A5), 4467–4489, doi:10.1029/JA092iA05p04467.

Hibberd, F. H., and W. J. Ross (1967), Variations in total electron content and other ionospheric parameters in association with magnetic storms, *J. Geophys. Res.*, *72*(21), 5331-5337, doi:10.1029/JZ072i021p05331.

Hosokawa, K., K. Shiokawa, Y. Otsuka, A. Nakajima, T. Ogawa, and J. D. Kelly (2006), Estimating drift velocity of polar cap patches with all-sky airglow imager at Resolute Bay, Canada, *Geophys. Res. Lett.*, *33*, L15111, doi:10.1029/2006GL026916.

Hosokawa, K., K. Shiokawa, Y. Otsuka, T. Ogawa, J.-P. St-Maurice, G. J. Sofko, and D. A. Andre (2009), Relationship between polar cap patches and field-aligned irregularities as observed with an all-sky airglow imager at Resolute Bay and the PolarDARN radar at Rankin Inlet, *J. Geophys. Res.*, *114*(A3), A03306, doi:10.1029/2008JA013707.

Hosokawa, K., T. Kashimoto, S. Suzuki, K. Shiokawa, Y. Otsuka, and T. Ogawa (2009), Motion of polar cap patches: A statistical study with all-sky airglow imager at Resolute Bay, Canada, *J. Geophys. Res.*, *114*, A04318, doi:10.1029/2008JA014020.

Hosokawa, K., J.-P. St-Maurice, G. J. Sofko, K. Shiokawa, Y. Otsuka, and T. Ogawa and (2010), Reorganization of polar cap patches through shears in the background plasma convection, *J. Geophys. Res.*, *115*, A01303, doi:10.1029/2009JA014599.

Hosokawa, K., S. Taguchi, K. Shiokawa, Y. Otsuka, Y. Ogawa, and M. Nicolls (2014), Global imaging of polar cap patches with dual airglow imagers, *Geophys. Res. Lett.*, *41*, 1–6, doi:10.1002/2013GL058748.

Huang, C.-S., J. C. Foster, L. P. Goncharenko, P. J. Erickson, W. Rideout, and A. J. Coster (2005), A strong positive phase of ionospheric storms observed by the Millstone Hill incoherent scatter radar and global GPS network, *J. Geophys. Res.*, *110*, A06303, doi:10.1029/2004JA010865.

Hutchinson, J. A., D. M. Wright, and S. E. Milan (2011), Geomagnetic storms over the last solar cycle: A superposed epoch analysis, *J. Geophys. Res.*, *116*, A09211, doi:10.1029/2011JA016463.

Immel, T. J., and A. J. Mannucci (2013), Ionospheric redistribution during geomagnetic storms, *J. Geophys. Res. Space Physics*, *118*(12), 7928-7939, doi:10.1002/2013JA018919.

Iyemori, T. (1990), Storm-time magnetospheric currents inferred from mid-latitude geomagnetic field variations, *J. Geomag. Geoelectr.*, *42*, 1249–1265, doi:10.5636/jgg.42.1249.

Iyemori, T., M. Takeda, M. Nose, Y. Odagi, and H. Toh (2010), Mid-latitude Geomagnetic Indices "ASY" and "SYM" for 2009 (Provisional), World Date Center for Geomagnetism, Kyoto, Japan. [Available at http://wdc.kugi.kyoto-u.ac.jp/aeasy/asy.pdf.]

Joshi, P. P., J. B. H. Baker, J. M. Ruohoniemi, J. J. Makela, D. J. Fisher, B. J. Harding, N. A. Frissell, and E. G. Thomas (2015), Observations of storm-time mid-latitude ion-neutral coupling using SuperDARN radars and NATION Fabry-Perot interferometers, *J. Geophys. Res. Space Physics*, *120*, 8989–9003, doi:10.1002/2015JA021475.

Kamei, T., M. Sugiura, and T. Araki (1992), Auroral Electrojet (AE) Indices for January - December 1992 (Provisional), World Date Center for Geomagnetism, Kyoto, Japan. [Available at http://wdc.kugi.kyoto-u.ac.jp/aedir/ae2/onAEindex.html.]

Kamide, Y., et al. (1998), Current understanding of magnetic storms: Storm-substorm relationships, *J. Geophys. Res.*, *103*(A8), 17705–17728, doi:10.1029/98JA01426.

King, J. H., and N. E. Papitashvili (2005), Solar wind spatial scales in and comparisons of hourly Wind and ACE plasma and magnetic field data, *J. Geophys. Res.*, *110*, A02104, doi:10.1029/2004JA010649.

Kintner, P. M. (1999), *Global Positioning System Theory and Design*, Cornell University.

Klobuchar, J. A., M. Mendillo, F. L. Smith III, R. B. Fritz, A. V. da Rosa, M. J. Davis, P. C. Yuen, T. H. Roelofs, K. C. Yeh, and B. J. Flaherty (1971), Ionospheric storm of March 8, 1970, *J. Geophys. Res.*, *76*(25), 6202–6207, doi:10.1029/JA076i025p06202.

Knudsen, W. C. (1974), Magnetospheric convection and the high-latitude F2 ionosphere, *J. Geophys. Res.*, *79*(7), 1046–1055, doi:10.1029/JA079i007p01046.

Kozyra, J. U., V. K. Jordanova, J. E. Borovsky, M. F. Thomsen, D. J. Knipp, D. S. Evans, D. J. McComas, and T. E. Cayton (1998), Effects of a high-density plasma sheet on ring current development during the November 26, 1993, magnetic storm, *J. Geophys. Res.*, *103*(A11), 26285-26305, doi:10.1029/98JA01964.

Kubota, M., H. Fukunishi, and S. Okano (2001), Characteristics of medium- and large-scale TIDs over Japan derived from OI 630-nm nightglow observation, *Earth Planets Space*, **53**, 741–751.

Kunduri, B. S. R., J. B. H. Baker, J. M. Ruohoniemi, L. B. N. Clausen, A. Grocott, E. G. Thomas, M. P. Freeman, and E. R. Talaat (2012), An examination of interhemispheric conjugacy in a subauroral polarization stream, *J. Geophys. Res.*, *117*, A08225, doi:10.1029/2012JA017784.

Lanzerotti, L. J., L. L. Cogger, and M. Mendillo (1975), Latitude dependence of ionosphere total electron content: Observations during sudden commencement storms, *J. Geophys. Res.*, *80*(10), 1287–1306, doi:10.1029/JA080i010p01287.

Liu, J., B. Zhao, and L. Liu (2010), Time delay and duration of ionospheric total electron content responses to geomagnetic storms, *Ann. Geophys.*, *28*, 795–805, doi:10.5194/angeo-28-795-2010.

Liu, J., T. Nakamura, L. Liu, W. Wang, N. Balan, T. Nishiyama, M. R. Hairston, and E. G. Thomas (2015), Formation of polar tongue of ionization during minor geomagnetic disturbed conditions, *J. Geophys. Res. Space Physics*, *120*, 6860–6873, doi:10.1002/2015JA021393.

Lockwood, M., and H. C. Carlson (1992), Production of polar cap electron density patches by transient magnetopause reconnection, *Geophys. Res. Lett.*, *19*, 1731–1734, doi:10.1029/92GL01993.

Lockwood, M., J. A. Davies, J. Moen, A. P. van Eyken, K. Oksavik, I. W. McCrea, and M. Lester (2005), Motion of the dayside polar cap boundary during substorm cycles: II. Generation of poleward-moving events and polar cap patches by pulses in the magnetopause reconnection rate, *Ann. Geophys.*, **23**, 3513–3532, doi:10.5194/angeo-23-3513-2005.

Loewe, C. A., and G. W. Prölss (1997), Classification and mean behavior of magnetic storms, *J. Geophys. Res.*, *102*(A7), 14209-14213, doi:10.1029/96JA04020.

Lorentzen, D. A., J. Moen, K. Oksavik, F. Sigernes, Y. Saito, and M. G. Johnsen (2010), In situ measurement of a newly created polar cap patch, *J. Geophys. Res.*, *115*, A12323, doi:10.1029/2010JA015710.

Lu, G., L. P. Goncharenko, A. D. Richmond, R. G. Noble, and N. Aponte (2008), A dayside ionospheric positive storm phase driven by neutral winds, *J. Geophys. Res.*, *113*, A08304, doi:10.1029/2007JA012895.

Luhmann, J. G. (1995), Ionospheres, in *Introduction to Space Physics*, edited by M. G. Kivelson and C. T. Russell, pp. 183-202, Cambridge University Press, New York, New York.

Matsushita, S. (1959), A study of the morphology of ionospheric storms, *J. Geophys. Res.*, *64*(3), 305–321, doi:10.1029/JZ064i003p00305.

Mendillo, M. (1971), Ionospheric total electron content behaviour during geomagnetic storms, *Nature*, *234*, 23–24, doi:10.1038/physci234023a0.

Mendillo, M. (2006), Storms in the ionosphere: Patterns and processes for total electron content, *Rev. Geophys.*, *44*, RG4001, doi:10.1029/2005RG000193.

Mendillo, M., and J. A. Klobuchar (2006), Total electron content: Synthesis of past storm studies and needed future work, *Radio Sci*, *41*, RS5S02, doi:10.1029/2005RS003394.

Milan, S. E., M. Lester, and T. K. Yeoman (2002), HF radar polar patch formation revisited: summer and winter variations in dayside plasma structuring, *Ann. Geophys.*, **20**, 487–499, doi:10.5194/angeo-20-487-2002.

Moen, J., H. C. Carlson, S. E. Milan, N. Shumilov, B. Lybekk, P. E. Sandholt, and M. Lester (2000), On the collocation between dayside auroral activity and coherent HF radar backscatter, *Ann. Geophys.*, **18**, 1531–1549, doi:10.1007/s00585-001-1531-2.

Moen, J., A. P. van Eyken, and H. C. Carlson (2001), EISCAT Svalbard Radar observations of ionospheric plasma dynamics in relation to dayside auroral transients, *J. Geophys. Res.*, *106*(A10), 21453-21461, doi:10.1029/2000JA000378.

Moen, J., N. Gulbrandsen, D. A. Lorentzen, and H. C. Carlson (2007), On the MLT distribution of *F* region polar cap patches at night, *Geophys. Res. Lett.*, *34*, L14113, doi:10.1029/2007GL029632.

Moffett, R. J., and S. Quegan (1983), The mid-latitude trough in the electron concentration of the ionospheric F-layer: a review of observations and modelling, *J. Atmos. Terr. Phys.*, *45*(5), 315–343, doi:10.1016/S0021-9169(83)80038-5.

Newell, P. T., T. Sotirelis, and S. Wing (2010), Seasonal variations in diffuse, monoenergetic, and broadband aurora, *J. Geophys. Res.*, *115*, A03216, doi:10.1029/2009JA014805.

Ogawa, T., N. Balan, Y. Otsuka, K. Shiokawa, C. Ihara, T. Shimomai, and A. Saito (2002), Observations and modeling of 630 nm airglow and total electron content associated with traveling ionospheric disturbances over Shigaraki, Japan, *Earth Planets Space*, **54**, 45–56.

Oksavik, K., J. M. Ruohoniemi, R. A. Greenwald, J. B. H. Baker, J. Moen, H. C. Carlson, T. K. Yeoman, and M. Lester (2006), Observations of isolated polar cap patches by the European Incoherent Scatter (EISCAT) Svalbard and Super Dual Auroral Radar Network (SuperDARN) Finland radars, *J. Geophys. Res.*, *111*, A05310, doi:10.1029/2005JA011400.

Perry, G. W., J.-P. St.-Maurice, and K. Hosokawa (2013), The interconnection between cross-polar cap convection and the luminosity of polar cap patches, *J. Geophys. Res. Space Physics*, *118*, 7306–7315, doi:10.1002/2013JA019196.

Prikryl, P., R. Ghoddousi-Fard, B. S. R. Kunduri, E. G. Thomas, A. J. Coster, P. T. Jayachandran, E. Spanswick, and D. W. Danskin (2013), GPS phase scintillation and proxy index at high latitudes during a moderate geomagnetic storm, *Ann. Geophys.*, *31*, 805–816, doi:10.5194/angeo-31-805-2013.

Prikryl, P., R. Ghoddousi-Fard, E. G. Thomas, J. M. Ruohoniemi, S. G. Shepherd, P. T. Jayachandran, D. W. Danskin, E. Spanswick, Y. Zhang, Y. Jiao, and Y. T. Morton (2015a), GPS phase scintillation at high latitudes during geomagnetic storms of 717 March 2012 Part 1: The North American sector, *Ann. Geophys.*, *33*, 636-656, doi:10.5194/angeo-33-637-2015.

Prikryl, P., et al. (2015b), GPS phase scintillation at high latitudes during geomagnetic storms of 717 March 2012 Part 2: Interhemispheric comparison, *Ann. Geophys.*, *33*, 657–670, doi:10.5194/angeo-33-657-2015.

Prikryl, P., R. Ghoddousi-Fard, J. M. Ruohoniemi, and E. G. Thomas (2015c), GPS phase scintillation at high latitudes during two geomagnetic storms, in *Aurora Dynamics and Space Weather* (eds Y. Zhang and L. J. Paxton), John Wiley & Sons, Inc, Hoboken, NJ, doi:10.1002/9781118978719.ch15.

Prölss, G. W. (1980), Magnetic storm associated perturbations of the upper atmosphere: Recent results obtained by satellite-borne gas analyzers, *Rev. Geophys.*, *18*(1), 183–202, doi:10.1029/RG018i001p00183.

Prölss, G. W. (1987), Storm-induced changes in the thermospheric composition at middle latitudes, *Planetary Space Sci.*, *35*(6), 807–811, doi:10.1016/0032-0633(87)90041-9.

Prölss, G. W. (1993), On explaining the local time variation of ionospheric storm effects, *Ann. Geophys.*, *11*, 1–9.

Prölss, G. W. (1995), Ionospheric F-region storms, in *Handbook of Atmospheric Electrodynamics*, vol. 2, edited by H. Volland, chap. 8, pp. 195–248, CRC Press, Boca Raton, Fla.

Prölss, G. W. (2008), Ionospheric Storms at Mid-Latitude: A Short Review, in *Midlatitude Ionospheric Dynamics and Disturbances* (eds P. M. Kintner, A. J. Coster, T. Fuller-Rowell, A. J. Mannucci, M. Mendillo, and R. Heelis), American Geophysical Union, Washington, D.C., doi:10.1029/181GM03.

Prölss, G. W., M. Roemer, and J. W. Slowey (1988), Dissipation of solar wind energy in the Earth's upper atmosphere: The geomagnetic activity effect, *Adv. Space Res.*, *8*(5), 215–261, doi:10.1016/0273-1177(88)90043-9.

Rideout, W., and A. Coster (2006), Automated GPS processing for global total electron content data, *GPS Solutions*, *10*(3), 219–228, doi:10.1007/s10291-006-0029-5.

Rishbeth, H., and O. K. Garriott (1969), *Introduction to Ionospheric Physics*, Academic Press, New York.

Rishbeth, H. (1998), How the thermospheric circulation affects the ionospheric F2-layer, *J. Atmos. Terr. Phys.*, *60*(14), 1385–1402, doi:10.1016/S1364-6826(98)00062-5.

Rodger, A. S., R. J. Moffett, and S. Quegan (1992), The role of ion drift in the formation of ionisation troughs in the mid- and high-latitude ionosphere–a review, *J. Atmos. Sol. Terr. Phys.*, *54*(1), 1–30, doi:10.1016/0021-9169(92)90082-V.

Rodger, A. S., S. B. Mende, T. J. Rosenberg, and K. B. Baker (1995), Simultaneous optical and HF radar observations of the ionospheric cusp, *Geophys. Res. Lett.*, *22*(15), 2045–2048, doi:10.1029/95GL01797.

Rodger, A. S. (2008), The Mid-Latitude Trough–Revisited, in *Midlatitude Ionospheric Dynamics and Disturbances* (eds P. M. Kintner, A. J. Coster, T. Fuller-Rowell, A. J. Mannucci, M. Mendillo, and R. Heelis), American Geophysical Union, Washington, D.C., doi:10.1029/181GM04.

Ruohoniemi, J. M., and R. A. Greenwald (1996), Statistical patterns of high-latitude convection obtained from Goose Bay HF radar observations, *J. Geophys. Res.*, *101*(A10), 21743–21763, doi:10.1029/96JA01584.

Ruohoniemi, J. M., and K. B. Baker (1998), Large-scale imaging of high-latitude convection with Super Dual Auroral Radar Network HF radar observations, *J. Geophys. Res.*, *103*(A9), 20, 797–20, doi:10.1029/98JA01288.

Ruohoniemi, J. M., R. J. Barnes, R. A. Greenwald, and S. G. Shepherd (2001), The response of the high-latitude ionosphere to the coronal mass ejection event of April 6, 2000: A practical demonstration of space weather nowcasting with the Super Dual Auroral Radar Network HF radars, *J. Geophys. Res.*, *106*(A12), 30085–30097, doi:10.1029/2000JA000217.

Ruohoniemi, J. M, and R. A. Greenwald (2005), Dependencies of high-latitude plasma convection: Consideration of interplanetary magnetic field, seasonal, and universal time factors in statistical patterns, *J. Geophys. Res.*, *110*, A09204, doi:10.1029/2004JA010815.

Sakai, J., K. Hosokawa, S. Taguchi, and Y. Ogawa (2014), Storm-time enhancements of 630.0-nm airglow associated with polar cap patches, *J. Geophys. Res. Space Physics*, *119*, 2214-2228, doi:10.1002/2013JA019197.

Sato, T., and G. F. Rourke (1964), F-region enhancements in the Antarctic, *J. Geophys. Res.*, *69*(21), 4591–4607, doi:10.1029/JZ069i021p04591.

Shaw, M., K. Sandhoo, and D. Turner (2000), Modernization of the Global Positioning System, *32nd Annual Precise Time and Time Interval (PTTI) Meeting.*

Shepherd, S. G. (2014), Altitude-adjusted corrected geomagnetic coordinates: Definition and functional approximations, *J. Geophys. Res. Space Physics*, *119*, 7501-7521, doi:10.1002/2014JA020264.

Shepherd, S. G., and J. M. Ruohoniemi (2000), Electrostatic potential patterns in the high-latitude ionosphere constrained by SuperDARN measurements, *J. Geophys. Res.*, *105*(A10), 23005–23014, doi:10.1029/2000JA000171.

Shiokawa, K., Y. Katoh, M. Satoh, M. K. Ejiri, T. Ogawa, T. Nakamura, T. Tsuda, and R. H. Wiens (1999), Development of Optical Mesosphere Thermosphere Imagers (OMTI), *Earth Planets Space*, **51**, 887–896, doi:10.1186/BF03353247.

Shiokawa, K., Y. Otsuka, and T. Ogawa (2009), Propagation characteristics of nighttime mesospheric and thermospheric waves observed by optical mesosphere thermosphere imagers at middle and low latitudes, *Earth Planets Space*, **61**, 479–491, doi:10.1186/BF03353165.

Spicher, A., T. Cameron, E. M. Grono, K. M. Yakymenko, S. C. Buchert, L. B. N. Clausen, D. J. Knudsen, K. A. McWilliams, and J. I. Moen (2015), Observation of polar cap patches and calculation of gradient drift instability growth times: A Swarm case study, *Geophys. Res. Lett.*, *42*, doi:10.1002/2014GL062590.

Stankov, S. M., K. Stegen, and R. Warnant (2010), Seasonal variations of storm-time TEC at European middle latitudes, *Adv. Space Res.*, *46*(10), 1318–1325, doi:10.1016/j.asr.2010.07.017.

Taguchi, S., K. Hosokawa, T. Ogawa, T. Aoki, and M. Taguchi (2012), Double bursts inside a poleward-moving auroral form in the cusp, *J. Geophys. Res.*, *117*, A12301, doi:10.1029/2012JA018150.

Taylor, G. N. (1961), The total electron content of the ionosphere during the magnetic disturbance of November 12-13, 1960, *Nature*, *189*, 740–741, doi:10.1038/189740a0.

Tohmatsu, T., and T. Ogawa (1990), *Compendium of Aeronomy*, Terra Sci., Tokyo.

Thomas, E. G. (2012), Dynamics of the geomagnetically disturbed ionosphere as measured by GPS receivers and SuperDARN HF radars, M.S. thesis, Virginia Tech, Blacksburg, VA, USA.

Thomas, E. G., J. B. H. Baker, J. M. Ruohoniemi, L. B. N. Clausen, A. J. Coster, J. C. Foster, and P. J. Erickson (2013), Direct observations of the role of convection electric field in the formation of a polar tongue of ionization from storm enhanced density, *J. Geophys. Res. Space Physics*, *118*, 1180–1189, doi:10.1002/jgra.50116.

Thomas, E. G., K. Hosokawa, J. Sakai, J. B. H. Baker, J. M. Ruohoniemi, S. Taguchi, K. Shiokawa, Y. Otsuka, A. J. Coster, J.-P. St.-Maurice, and K. A. McWilliams (2015), Multi-instrument, high-resolution imaging of polar cap patch transportation, *Radio Sci.*, *50*, 904–915, doi:10.1002/2015RS005672.

Thomas, E. G., J. B. H. Baker, J. M. Ruohoniemi, A. J. Coster, and S.-R. Zhang (2016), The geomagnetic storm-time response of GPS total electron content in the North American sector, *J. Geophys. Res. Space Physics*, *121*, doi:10.1002/2015JA022182.

Thomas, L., and F. H. Venables (1966), The onset of the F-region disturbance at middle latitudes during magnetic storms, *J. Atmos. Terr. Phys.*, *28*(6), 599–605, doi:10.1016/0021-9169(66)90073-0.

Tsurutani, B. T., et al. (2006), Corotating solar wind streams and recurrent geomagnetic activity: A review, *J. Geophys. Res.*, *111*, A07S01, doi:10.1029/2005JA011273.

Voiculescu, M., I. Virtanen, and T. Nygrén (2006), The F-region trough: seasonal morphology and relation to interplanetary magnetic field, *Ann. Geophys.*, *24*, 173–185, doi:10.5194/angeo-24-173-2006.

Volland, H. (1979), Magnetospheric electric fields and currents and their influence on large scale thermospheric circulation and composition, *J. Atmos. Terr. Phys.*, *41*, 853–866, doi:10.1016/0021-9169(79)90128-4.

Walker, I. K., J. Moen, L. Kersley, and D. A. Lorentzen (1999), On the possible role of cusp/cleft precipitation in the formation of polar-cap patches, *Ann. Geophys.*, **17**, 1298–1305, doi:10.1007/s00585-999-1298-4.

Walsh, B. M., E. G. Thomas, K.-J. Hwang, J. B. H. Baker, J. M. Ruohoniemi, and J. W. Bonnell (2015), Dense plasma and Kelvin-Helmholtz waves at Earth's dayside magnetopause, *J. Geophys. Res. Space Physics*, *120*, 5560–5573, doi:10.1002/2015JA021014.

Wanliss, J. A., and K. M. Showalter (2006), High-resolution global storm index: *Dst* versus SYM-H, *J. Geophys. Res.*, *111*, A02202, doi:10.1029/2005JA011034.

Weber, E. J., J. Buchau, J. G. Moore, J. R. Sharber, R. C. Livingston, J. D. Winningham, and B. W. Reinisch (1984), F layer ionization patches in the polar cap, *J. Geophys. Res.*, *89*(A3), 1683–1694, doi:10.1029/JA089iA03p01683.

Weber, E. J., J. A. Klobuchar, J. Buchau, H. C. Carlson Jr., R. C. Livingston, O. de la Beaujardiere, M. McCready, J. G. Moore, and G. J. Bishop (1986), Polar cap F layer patches, *J. Geophys. Res.*, *91*(A11), 12121–12129, doi:10.1029/JA091iA11p12121.

Yeh, H.-C., J. C. Foster, F. J. Rich, and W. Swider (1991), Storm time electric field penetration observed at mid-latitude, *J. Geophys. Res.*, *96*(A4), 5707–5721, doi:10.1029/90JA02751.

Yionoulis, S. M. (1998), The Transit Satellite Geodesy Program, *Johns Hopkins APL Technical Digest*, *19*(1), 37.

Yizengaw, E., M. B. Moldwin, and D. Galvan (2006), Ionospheric signatures of a plasmaspheric plume over Europe, *Geophys. Res. Lett.*, *33*, L17103, doi:10.1029/2006GL026597.

Yizengaw, E., M. B. Moldwin, D. Galvan, B. A. Iijima, A. Komjathy, and A. J. Mannucci (2008a), Global plasmaspheric TEC and its relative contribution to GPS TEC, *J. Atmos. Sol. Terr. Phys.*, *70*, 1541–1548, doi:10.1016/j.jastp.2008.04.022.

Yizengaw, E., J. Dewar, J. MacNeill, M. B. Moldwin, D. Galvan, J. Sanny, D. Berube, and B. Sandel (2008b), The occurrence of ionospheric signatures of plasmaspheric plumes over different longitudinal sectors, *J. Geophys. Res.*, *113*, A08318, doi:10.1029/2007JA012925.

Zhang, Q.-H., et al. (2011), On the importance of interplanetary magnetic field $|B_y|$ on polar cap patch formation, *J. Geophys. Res.*, *116*, A05308, doi:10.1029/2010JA016287.

Zhang, Q.-H., B.-C. Zhang, M. Lockwood, H.-Q. Hu, J. M. Moen, J. M. Ruohoniemi, E. G. Thomas, S.-R. Zhang, H.-G. Yang, R.-Y. Liu, K. A. McWilliams, and J. B. H. Baker (2013), Direct Observations of the Evolution of Polar Cap Ionization Patches, *Science*, **339**(6127), 1597–1600, doi:10.1126/science.1231487.

Zhang, S.-R., J. C. Foster, A. J. Coster, and P. J. Erickson (2011), East-West Coast differences in total electron content over the continental US, *Geophys. Res. Lett.*, *38*, L19101, doi:10.1029/2011GL049116.

Zhang, S.-R., J. C. Foster, J. M. Holt, P. J. Erickson, and A. J. Coster (2012), Magnetic declination and zonal wind effects on longitudinal differences of ionospheric electron density at midlatitudes, *J. Geophys. Res.*, *117*, A08329, doi:10.1029/2012JA017954.

Zhang, S.-R., Z. Chen, A. J. Coster, P. J. Erickson, and J. C. Foster (2013), Ionospheric symmetry caused by geomagnetic declination over North America, *Geophys. Res. Lett.*, *40*, 5350-5354, doi:10.1002/2013GL057933.

Zhao, B., W. Wan, L. Liu, and T. Mao (2007), Morphology in the total electron content under geomagnetic disturbed conditions: Results from global ionosphere maps, *Ann. Geophys.*, *25*, 1555–1568, doi:10.5194/angeo-25-1555-2007.

Zhao, B., M. Wang, Y. Wang, Z. Ren, X. Yue, J. Zhu, W. Wan, B. Ning, J. Liu, and B. Xiong (2013), East-west differences in F-region electron density at midlatitude: Evidence from the Far East region, *J. Geophys. Res. Space Physics*, *118*, 542-553, doi:10.1029/2012JA018235.

Zou, S., A. J. Ridley, M. Moldwin, M. J. Nicolls, A. J. Coster, E. G. Thomas, and J. M. Ruohoniemi (2013), Multi-instrument observations of SED during 24-25 October 2011 storm: Implications for SED formation processes, *J. Geophys. Res. Space Physics*, *118*, 7798–7809, doi:10.1002/2013JA018860.

Zou, S., M. Moldwin, A. J. Ridley, M. J. Nicolls, A. J. Coster, E. G. Thomas, and J. M. Ruohoniemi (2014), On the generation/decay of the storm-enhanced density (SED) plumes: Role of the convection flow and field-aligned ion flow, *J. Geophys. Res. Space Physics*, *119*, 8543-8559, doi:10.1002/2014JA020408.